THE DEVELOPMENT OF NOVEL APPLICATIONS OF RAMAN SPECTROSCOPY

by

ADAM JASON BASS

B.Sc., The University of British Columbia, 2000

A THESIS SUBMITTED IN PARTIAL FULFILMENT OF
THE REQUIREMENTS FOR THE DEGREE OF

MASTER OF SCIENCE

in

THE FACULTY OF GRADUATE STUDIES

CHEMISTRY

THE UNIVERSITY OF BRITISH COLUMBIA

February 2005

Abstract

This thesis explores two different facets of Raman spectroscopy that aim to extend the applications of this technique.

Ultraviolet Resonance Raman Spectroscopy was used to examine the stable tryptophan and tyrosine radicals of the reaction of Cytochrome c Peroxidase (CcP) with Hydrogen Peroxide. Native CcP, reduced CcP and a CcP W191F mutant were analyzed at 248.2 nm in a fibre-optic probe setup and difference spectra were obtained from the data. Signals seen in the difference spectra were attributed to the tryptophan and tyrosine radicals in the protein.

A surface plasmon resonance (SPR) imager was designed and built that interfaced with a Renishaw 1000B microscope with the future aim of analyzing DNA microarrays. The combination of the two techniques aimed to harness the enhancement advantages of Surface Enhanced Raman Spectroscopy (SERS). The device successfully imaged liquid drops on it's surface and was able to distinguish differences of refractive index between the solution of as little as $5x10^{-3}$. The spectrum of evaporated Salmon Sperm DNA spotted on the surface of the SPR imager was collected and a mild enhancement of the spectrum was observed when the SPR imager was operating concurrently during the acquisition of Raman spectra.

Table of Contents

List of Tables

List of Figures

List of Abbreviations

ABTS	2,2'-Azino-bis3-Ethylbenzthiazoline-6-Sulfonic Acid
CcP	Cytochrome c Peroxidase
DNA	Deoxyribonucleic acid
ENDOR	Electron Nuclear Double Resonance
EPR	Electron Paramagnetic Resonance
FISH	Fluorescent In-Situ Hybirdization
IPTG	Isopropyl-D-thiogalactoside
LUMO	Least unoccupied molecular orbital
OPO	Optical Parametric Oscillators
PMSF	Phenylmethylsulfonyl Fluoride
RNA	Ribonucleic acid
SDS-PAGE	Sodium Dodecyl Sulfate Polyacrylamide Gel Electrophoresis
SERS	Surface Enhanced Raman Spectroscopy
SNR	Signal to noise ratio
SPR	Surface Plasmon Resonance
UVRRS	UV Resonance Raman Spectroscopy

Acknowledgements

I would like to take this opportunity to thank all the people who have helped me at the various stages of this endeavor. First and foremost, I would like to thank my parents and my brothers for trying to look as interested as possible when I attempted to explain to them what I was studying at school. Their constant encouragement was instrumental in getting me this far and I will never forget it. My supervisors, Mike Blades and Robin Turner, guided me through this adventure and I would like to thank them for taking the time to help me along the path of becoming a better scientist. I would especially like to thank all my lab-mates, August Specht, Ken Wright, Chris Barbosa, Andrew Jirasek and Marcia Yu, for putting up with my constant questions and nattering. I truly appreciate all the guidance and patience that these talented and very intelligent people gave to me. Dave McLaren deserves a special thank you for showing me what a positive disposition really is. My friends deserve a huge thank you for keeping my mind off of school when I wasn't there. Finally, I'd like to thank my girlfriend, Nathalie Saad, for her unwavering support, her ever positive attitude, and her beautiful smile which helped me get over the last few hurdles of this thesis.

Chapter 1

Introduction to Raman Spectroscopy

1.1 The History and Development of Raman Spectroscopy

In his Nobel acceptance speech about the discovery of the phenomenon which carries his name, C.V. Raman said "It soon became evident, however, that the subject possessed a significance extending far beyond the special purpose for which the work was undertaken, and that it offered unlimited scope for research." Three quarters of a century later, Raman's 1928 paper in which he used a telescope, sunlight and his eyes to observe Raman scattering[1] has almost become scientific legend and it is a testament to Raman's intelligence and foresight that he was able to foretell the impact his discovery would have on the scientific community. The historical development and theoretical treatment of vibrational Raman light scattering are presented here using an appropriate distillation of a few sources of particular relevance to this thesis[2,3].

Early research in Raman Scattering was mainly centered on the development of new components for instrumentation. Raman scattering, which will be described in more detail later, is a spectroscopic phenomenon whereby photons impinge on molecules, excite them into virtual energy states, and then as molecules relax into lower energy states they scatter photons. Ideally a Raman experiment requires a high intensity light excitation source that has a very narrow band width, a method of separating light, and a light detector with a quantum efficiency that is both high and linear across all wavelengths. Since the sun is certainly not the most ideal excitation source, the focus of initial progress in Raman was the engineering of new narrow band excitation sources. Various atomic emission lamps were developed but mercury lamps proved to be the first

lamp that had sufficient intensity to be effective. Various configurations of the Mercury lamp were examined and other types of excitation sources were developed but significant advancement in light technology did not occur until the realization of coherent light sources. In time, both the Argon Ion Laser and the Nd:YAG Laser have proven to be important laser sources for Raman Spectroscopy due to their narrow, high intensity laser lines. The advent of the dye laser for pulsed applications allowed access to wavelength tunability that extends from the UV to the Infrared. More recently, dye lasers have been replaced by Optical Parametric Oscillators (OPO) which give superior wavelength tunability and steady power output across wavelengths while at the same time negating the need for a multitude of toxic dyes. Tunable pseudo-continuous wavelength lasers, like the Titanium Sapphire laser, have also represented a great stride in laser technology.

The use of unaided human eyes as detectors were quickly abandoned in early days of the development of Raman spectroscopy and photographic plates soon followed as the detector of choice. The inherent inconvenience and bulky nature of photographic plates eventually led to their replacement by photomultiplier tubes in the 1940's. More recently, Charge-Coupled Devices and Intensified Charge-Coupled Devices have come into use, however, photomultipliers are also still in use. Both the liquid nitrogen cooled detectors and Peltier cooled detectors available offer high quantum yields while at the same time having favorable noise characteristics.

Light wavelength separation in Raman was originally performed by prism monochromators, but present instrumentation has moved towards reflective gratings. Reflective gratings are superior because they are inexpensive to produce, disperse radiation linearly, and perform better for the same size dispersing element. Holographic

gratings have become the gratings of choice due to the high number of lines per millimeter that one can achieve which offers better dispersion.

Modern applications of Raman have grown dramatically and a multitude of technological advances have broadened the applications of this technique. In recent years some advances in Raman technology, including fibre-optic probes and Raman microscopes, have allowed Raman to be used in systems that were previously impossible to analyze via this technique.

One of the main goals of this thesis is to continue the trend of technological development in Raman technology. It is also hoped that this work might extend the breadth of applications currently available in Raman Spectroscopy.

1.2 Raman Scattering

There are many different ways in which light can interact with molecules. The Raman effect is the inelastic scattering of light by molecules. In non-resonance Raman spectroscopy, light impinges on a molecule and excites it to any one of an infinite number of virtual vibrational states, which exist between two electronic energy levels and which exactly corresponds to the energy of the incoming photon. Once a molecule is elevated to a virtual state it has a very short lifetime of approximately $1x10^{-14}$ s. The molecule can either decay to it's original vibrational level (ν_o) or it can fall to a different vibrational energy level (ν_n) that is either above or below it's original vibrational level. This results in the molecule emitting a photon of energy corresponding to that transition. If the molecule decays to the state from which it originated, the frequency of the emitted light (ν) will have the same frequency as the incoming light (ν_o) and is called Rayleigh Scattering ($\nu = \nu_o$). However, if the molecule falls to a vibrational level of higher energy

than the originating vibrational level of the molecule, then the emitted light will have a lower frequency ($\nu = \nu_o - \nu_n$) than the incoming light and this is known as Stokes Scattering. On the other hand, if the molecule falls to a vibrational level of lower energy than the original vibrational level, the emitted light will have a frequency that is higher than the incident light frequency ($\nu = \nu_o + \nu_n$) which is deemed Anti-Stokes Scattering.

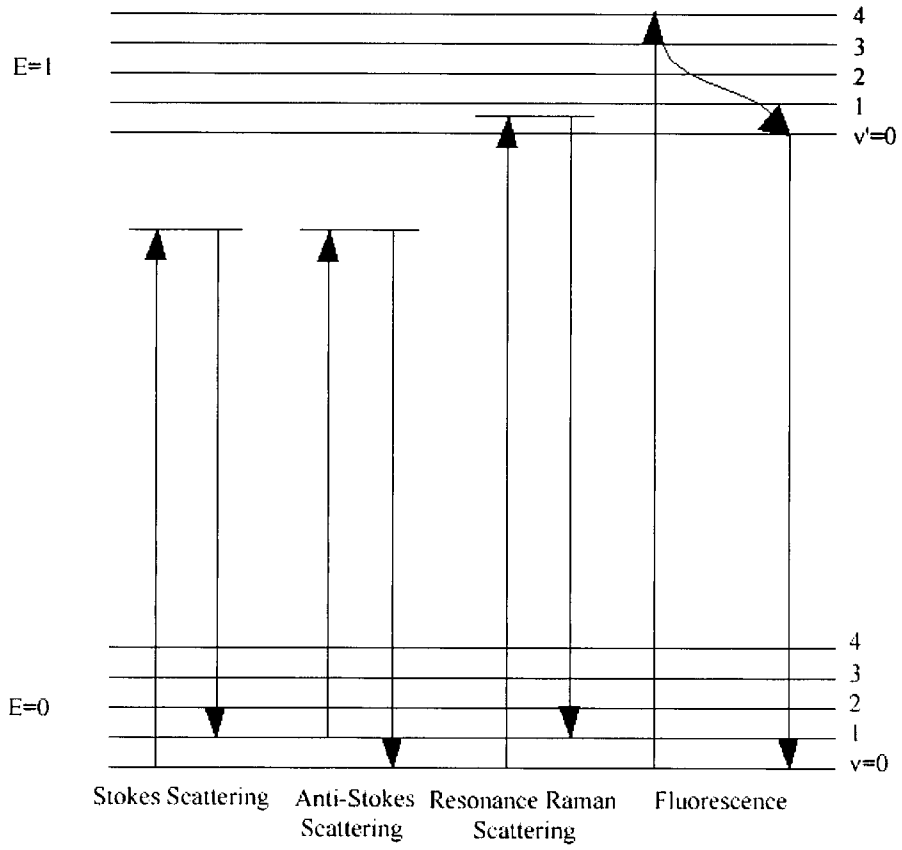

Figure 1.1: Energy level transitions corresponding to various optical phenomena are depicted. Vibration energy levels are depicted by v = 0 to v = 5 and v' = 0 to v' = 5 and electronic energy levels are depicted by E = 0 and E = 1. The arrows depict electronic energy level transitions.

In general, Raman scattering is a very weak phenomenon and only about 1 in 1×10^9 photons are inelastically scattered. Fluorescence signals, on the other hand, are extremely intense in comparison. Since both fluorescence and Raman scattering can occur

simultaneously in a molecule and the two wavelengths of light observed from these two effects may overlap, light from fluorescence may completely obscure a Raman signal. Although in conventional (i.e., non-resonance) Raman any wavelength of light may be used, fluorescence is generally avoided by exciting the analyte with photons with energies that are not high enough to promote electrons across the electronic transitions required for fluorescence to occur. Fluorescence is also avoided in Resonance Raman and in Surfaced Enhanced Raman Spectroscopy but these cases are unique and will be discussed separately.

1.2.1 Classical Scattering Theory

If we consider the electric field component of light, we see that it fluctuates over time (t) as shown in equation (1.1):

$$E = E_o \cos 2\pi \nu_o t \qquad (1.1)$$

where E is the electric field strength, E_o is the vibrational amplitude, ν_o is the frequency of the light. If we then consider this light interacting with a molecule, an electric dipole moment is induced:

$$P = \alpha E = \alpha E_o \cos 2\pi \nu_o t \qquad (1.2)$$

where P is the electric dipole moment, and the α is the polarizability of a molecule. As can be seen in the first half of equation 1.2, polarizability is a proportionality constant that determines the magnitude of the dipole moment induced for a given electric field. In

reality the dipole moment of any real molecule is three-dimensional and, as such, α is represented in three-dimensions by equation (1.3):

$$\begin{bmatrix} P_x \\ P_y \\ P_z \end{bmatrix} = \begin{bmatrix} \alpha_{xx} & \alpha_{xy} & \alpha_{xz} \\ \alpha_{yx} & \alpha_{yy} & \alpha_{yz} \\ \alpha_{zx} & \alpha_{zy} & \alpha_{zz} \end{bmatrix} \begin{bmatrix} E_x \\ E_y \\ E_z \end{bmatrix} \tag{1.3}$$

From here we can assume that the molecule is vibrating:

$$q = q_o \cos 2\pi \nu_m t \tag{1.4}$$

where q is the nuclear displacement, ν_m is the vibrating frequency, and q_o is the vibrational amplitude. At small vibrational amplitudes α is proportional to q and so we can write:

$$\alpha = \alpha_o + \left(\frac{\partial \alpha}{\partial q}\right)_o q_o + \ldots \tag{1.5}$$

where α_o is the polarizability at the equilibrium position and $(\partial\alpha/\partial q)_o$ is the change in α with respect to changes in q from the equilibrium position. By combining equations (1.1), (1.2) and (1.4) we arrive at:

$$\begin{aligned} P &= \alpha_o E_o \cos 2\pi \nu_o t \\ &+ \frac{1}{2}\left(\frac{\partial \alpha}{\partial q}\right)_o q_o E_o \left[\cos\{2\pi(\nu_o + \nu_m)t\} + \cos\{2\pi(\nu_o - \nu_m)t\}\right] \end{aligned} \tag{1.6}$$

Equation (1.6) has 2 terms that are very important for the classical explanation of Raman scattering. The first term of the equation dictates that the oscillating dipole will scatter light at frequency v_o which is known as Rayleigh scattering. The second term of equation (1.6) is comprised of 2 distinct parts. The first part of the equation shows that the dipole will scatter light at a frequency $(v_o + v_m)$, which is known as Stokes scattering, while the second half dictates that the dipole will also scatter light at a frequency $(v_o - v_m)$ which corresponds to Anti-Stokes scattering. Another important point is that the second term of equation (1.6) is preceeded by $(\partial\alpha/\partial q)_o$ which illustrates that Raman scattering will only occur if this term- is non-zero. For this to occur, the molecule must undergo a change in polarizability.

It is important at this point to understand why Stokes scattering is inherently more intense than Anti-Stokes scattering. The classical description of Raman scattering does not give any insight into the reason for the difference in intensities between Stokes and Anti-Stokes scattering, however, some insight into this difference can be elucidated from statistical mechanics. The Boltzman distribution dictates that a molecule has the highest probability of existing in the lowest energy level available to it and the probability of existing in higher states is much lower. Since Anti-Stokes Raman scattering originates from molecules being excited when they are in higher vibrational energy levels then it follows that the Anti-Stokes bands should be less intense than Stokes bands.

1.2.2 Resonance Raman Spectroscopy

Resonance Raman Scattering occurs when you excite a molecule with a wavelength of light that is close to that which corresponds to an electronic transition of

the molecule. In this situation the amount of scattered light from molecules is typically 10^3 to 10^5 times more than that of non-resonance Raman[2]. The equation that describes the intensity of a Raman band (accounting for quantum effects) is[2]:

$$I_{mn} = \text{constant} \cdot I_o \cdot (\nu_o - \nu_{mn})^4 \sum_{\rho\sigma} \left| (\alpha_{\rho\sigma})_{mn} \right|^2 \qquad (1.7)$$

Where m is the initial vibrational state of the electronic ground state, n is the final vibrational state of the electronic ground state, I_o is the laser intensity with frequency ν_o and $(\alpha_{\rho\sigma})_{mn}$ is the component of the polarizability tensor corresponding to the m→ n vibrational transition (where $\rho\sigma$ are the column and row indices of the polarizability tensor). If we look more closely at the $(\alpha_{\rho\sigma})_{mn}$ term and rewrite it in the following manner[2]:

$$(\alpha_{\rho\sigma})_{mn} = \frac{1}{h} \sum_e \left(\frac{M_{me} M_{en}}{\nu_{em} - \nu_o + i\Gamma_e} + \frac{M_{me} M_{en}}{\nu_{en} + \nu_o + i\Gamma_e} \right) \qquad (1.8)$$

where M_{me} and M_{en} are the electric transition dipole moments, h is Planck's constant, e is an electronic excited state, Γ_e is the band width of the *e*th state, and $i\Gamma_e$ is referred to as the damping constant. The transitional dipole moment can be described as:

$$M_{ab} = \int \Psi_a^* \mu_\sigma \Psi_b d\tau \qquad (1.9)$$

where Ψ is the wave function, Ψ^* is the complex conjugate of the wave function and μ is the magnitude of the induced dipole moment. As ν_{em} approaches ν_o the first term of equation (1.8) becomes extremely large and thus the Raman band intensity shown in equation (1.7) becomes extremely large. This explains why Resonance Raman signals are much more intense then the non-resonance case. The intensity of different bands within a particular chromophore can be explained using the concept of the Franck-Condon principle and Franck-Condon overlap integrals. The Franck-Condon principle states that since electronic transitions occur almost instantaneously compared to vibrational changes of the nucleus of molecules, electronic transitions are said to be vertical with respect to the vibrational states. The relative intensities of the bands of a spectrum are proportional to the amount of overlap between the areas of the probability density.

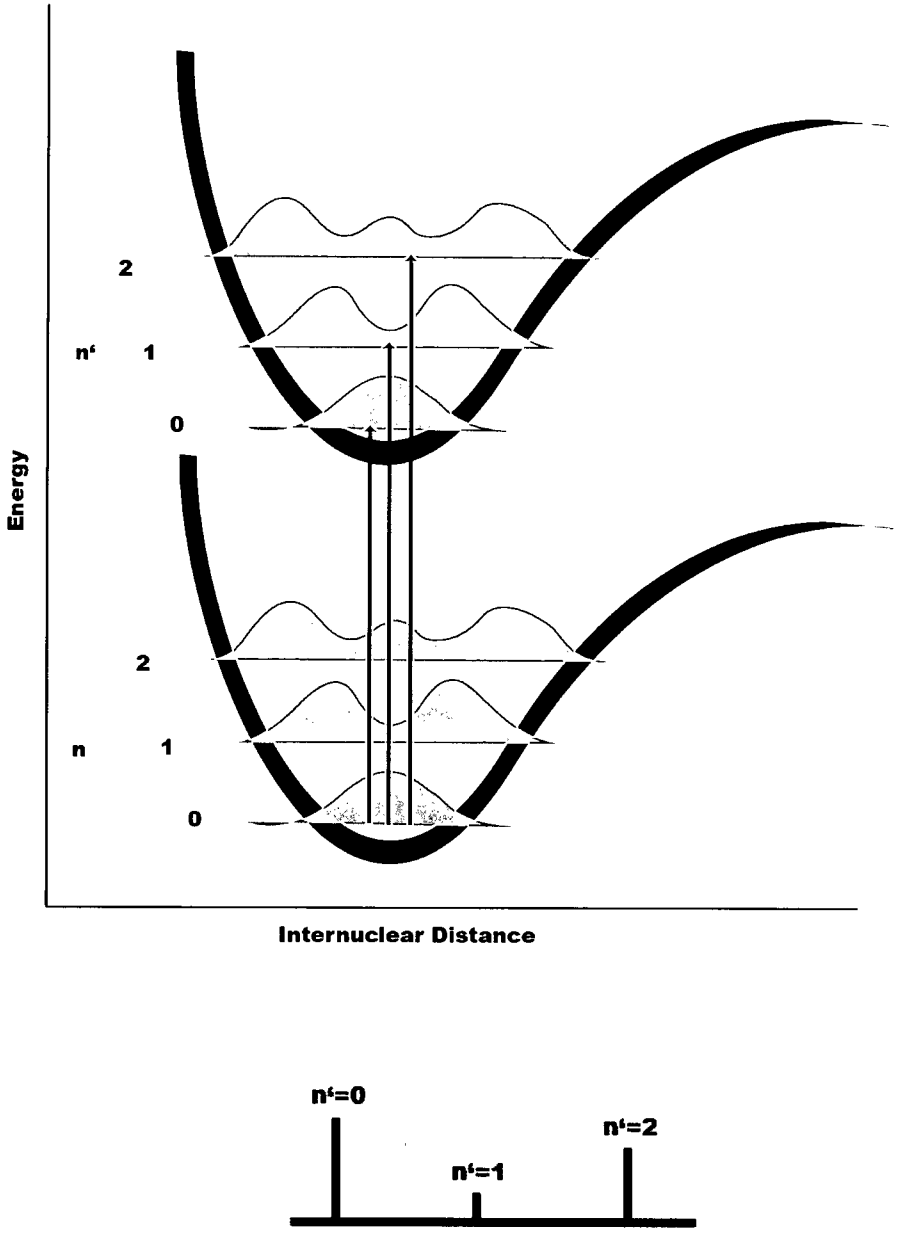

Figure 1.2 (Top) A graphical illustration of Franck-Condon Overlap. The two curves represent the internuclear distance between two nuclei of a molecule at two different energy levels. The vibrational energy levels are depicted within each electronic energy level and the shaded areas represent the harmonic-oscillator probability densities for each vibrational state. The arrows represent both electronic and vibrational transitions. (Bottom) The predicted intensity of transitions from the n = 0 to n' = 0,1,2 levels.

Since the resonance enhancement is associated with an electronic absorption band, by using Resonance Raman it is possible to selectively enhance regions within a molecule that have different electronic absorptions. Heme based proteins, like Cytochrome c Peroxidase for example, have an iron porphyrin ring which is integral and required for correct protein function and the understanding of the function of the heme group is very important to protein characterisation. If non-resonance Raman spectroscopy was employed to investigate the heme group within these proteins, the analysis would be much more complex since the bands specific to the heme group would appear amongst a myriad of other protein bands of similar amplitudes. Fortunately, Heme has a characteristic absorption in the green region of the visible spectrum known as the Soret band. By exciting these proteins in the Soret region it is possible to selectively enhance the heme group within the protein[4-10] and drastically reduce the contribution of other interferring vibrations.

1.2.2.1 UV Resonance Raman Characteristics and Applications

While UV Resonance Raman Spectroscopy (UVRRS) shares all the characteristics of Resonance Raman Spectroscopy it has advantages that are unique and are worth mentioning separately. One of the main disadvantages of non-resonance Raman is the emission of unwanted fluorescence which can mask the Raman signal. In non-resonance Raman this is usually avoided by exciting in the infrared or near infrared region where the energy of photons is low enough to avoid reaching an electronic state and thus cause fluorescence. However, at such low frequencies the Raman signal is much

weaker and higher laser powers, longer integration times or Fourier Transform methods must be used either separately or in combination to achieve a reasonable signal to noise ratio (SNR). Perhaps the greatest advantage of working in the ultraviolet region of the electromagnetic spectrum is that when a molecule is excited below ~260 nm, molecular fluorescence is significantly red-shifted compared to the Raman scattered light. Since the two signals do not overlap, the interference and noise of the unwanted fluorescence is avoided completely while still maintaining the large scattering cross sections that are advantageous in Resonance Raman scattering. A further SNR advantage is realized due to the $(\nu_o-\nu_{mn})^4$ term of equation 1.7. Many biochemical analytes of interest also exhibit resonance enhancement in the UV.

The characteristics of UVRRS make it a very useful tool for investigating biological molecules, like proteins and deoxyribonucleic acid (DNA)[11-24]. In proteins, the aromatic amino acids Tryptophan, Tyrosine and Phenylalanine are often important in protein function due to their ability to accept or donate electrons. Conveniently, electronic absorptions for these side chains occur in different regions of the ultraviolet spectrum allowing some degree of selective excitation. Interference from the protein backbone can be avoided since it is excited in the deep ultraviolet region, close to 200 nm. In the case of DNA, the four bases adenine, guanine, cytosine and thymine absorb in the ultraviolet region as well as it's phosphate backbone. In each of these cases, it is possible to selectively enhance the species of interest and reject most of the competing signals. Fluorescence avoidance is also very important since large macro-molecules often exhibit a high fluorescence quantum efficiency.

1.3 Surface Enhanced Raman Spectroscopy

Surface Enhanced Raman Spectroscopy (SERS) was first discovered in 1977. Two different research groups simultaneously concluded that the abnormally high scattering signal from pyridine bound to a silver electrode that had undergone one oxidation reduction cycle was due to a new enhancement mechanism[25,26]. Since the discovery of SERS, the field has expanded dramatically and many molecules have been shown to exhibit this effect on a variety of SERS active metals. The noble metals have been the most widely used SERS substrates and Silver has been found to give the highest levels of enhancement while Gold and Copper substrates also provide a good level of enhancement. SERS enhancements on the order of 10^{14} have now been observed for some molecules thus allowing single molecule Raman Spectroscopy[27].

The explanation of SERS in terms of the underlying physical-chemical mechanisms remains a subject of active research, and the mathematical foundations of SERS are inherently complex. It is beyond the scope of this thesis to give a rigorous description of SERS details of them, however a qualitative description will be presented that is based on a variety of sources.[27-39]

From the outset of the discovery of SERS, this phenomenon has been attributed to two contributing enhancement mechanisms: a first layer chemical enhancement and an electromagnetic enhancement. The chemical enhancement is by far the weaker of the two enhancement mechanisms and it has been estimated that it only provides 10 to 100 times the total signal enhancement observed in SERS. The nature of the chemical enhancement is attributed to two possible mechanisms. The first involves a new metal to analyte charge-transfer electronic transition that is characterized as a Resonance Raman effect, while the second mechanism is a dynamic charge transfer occurring between the metal

and the molecule. It is postulated that this second effect involves an excited electron transferring from the metal into the least unoccupied molecular orbital (LUMO) of an adsorbed analyte molecule and then relaxing to produce a photon Stokes-shifted from the excitation frequency. It is thought that the sharp features on the surface of the metal aid in these chemical enhancements. The electromagnetic enhancement in SERS is responsible for the far majority of the enhancement that is attributed to SERS. The electromagnetic enhancement derives from enhanced local optical fields that occur on the metal surface that interact with the molecule that is being excited. These enhanced fields are due to evanescent electromagnetic fields associated with surface plasmon resonances. The concept and physics of surface plasmon resonance will be further explored in the next chapter of this thesis. Surface plasmon fields have been theoretically modelled for single colloid silver and gold spheroids and such analyses have predicted strong enhancement on sharp features. This prediction correlates well with the observation of apparent "hot spots" that occur near sharp features on fractal surfaces where large electromagnetic fields exist. As will be explained later, surface plasmon resonances change with wavelength and as a result the hot spots in fractal surfaces have been observed to change location with wavelength.

In the past, the best SERS signals were found to occur on fractal silver surfaces. However, because silver surfaces tended to be unstable due to oxidation, it was nearly impossible to create two silver SERS substrates that had the same enhancement characteristics. While this is not a serious issue for qualitative analysis of molecules, it certainly is a serious issue if meaningful analytical results are to be done with this technology. As a result of this, a large portion of research in the field has been involved in the development of SERS-active substrates that offer strong and reproducible

enhancement[40-46]. Significant advances in this area could have a major impact on existing and developing applications of SERS, particularly in trace detection and analysis of chemicals and analysis of biological molecules in low concentrations[30,47-52].

Chapter 2

Introduction to Surface Plasmon Resonance

2.1 Historical Development of Surface Plasmon Resonance

Surface Plasmon Resonance (SPR) was first observed on a diffraction grating in the beginning of the twentieth century by Wood[53]. It was not until the 1960s that both Otto[54] and Krestchmann[55] separately discovered methods of exciting surface plasmon resonances using attenuated total reflection geometries. Later, in the early eighties, SPR began being used as a sensor to detect gases[56] and also found its first use as a biosensor[57]. The first commercial instrument was released in 1990 by Biacore AB[58] and now there are at least half a dozen companies that offer competing instruments. SPR measurements have become very commonplace in biophysical laboratories and thousands of studies have now been done using information taken from SPR devices. Like any technology, early developments of SPR technology concentrated on improving the technique of surface plasmon resonance. More recently, however, the focus has become quite directed on the development of new applications for this technology[59]. Two major areas of research in SPR technology are the development of SPR platforms capable of detecting biological analytes and the analysis of the biophysical properties of biological substances[59].

Note that although grating based SPR devices do exist and theory for them has been developed, they will not be discussed here since the present work revolves around attenuated total reflection geometries.

2.2 Theoretical Basis of Surface Plasmon Resonance

The theory behind SPR has been described previously[60-62] and the following section will attempt to summarize these sources and highlight the salient points of SPR theory most relevant to the discussion of work presented in this thesis.

Consider the interface between two different materials, 1 and 2, with complex frequency dependent dielectric constants $\varepsilon_1(\omega)$ and $\varepsilon_2(\omega)$. Surface plasmons can only be excited at this interface if the electric field of the exciting radiation has a component that is normal to the interface. As such, p-polarized light is capable of exciting surface plasmons because it has $E = (E_x,0,E_z)$, where z is normal to the surface, while s-polarized light is unable to excite surface plasmon modes because it has $E = (0,E_y,0)$. The electromagnetic surface wave should be described by:

$$\vec{E}_1 = \vec{E}_{10} e^{i(\vec{k}_{x1}\vec{x}+\vec{k}_{z1}\vec{z}-\omega t)} \text{ in medium 1, } z < 0 \qquad (2.1)$$

$$\vec{E}_2 = \vec{E}_{20} e^{i(\vec{k}_{x2}\vec{x}+\vec{k}_{z2}\vec{z}-\omega t)} \text{ in medium 2, } z > 0 \qquad (2.2)$$

where $\vec{E}$ stands for the electric field component, $\vec{k}_{x1}$ and $\vec{k}_{x2}$ are the wavevectors is the x-direction, $\vec{k}_{z1}$ and $\vec{k}_{z2}$ are the wavevectors in the z-direction and ω is the angular frequency. It can also be shown that:

$$\frac{k_{z1}}{k_{z2}} = -\frac{\varepsilon_1}{\varepsilon_2} \qquad (2.3)$$

which demonstrates that for any electromagnetic mode to occur, the dielectric constants of the two materials at the interface must be of opposing signs. In this case the two

materials at the interface are a metal and a dielectric material. The dispersion relationship, or the energy-momentum relationship, of the surface plasmon can be shown to be:

$$k_x = \frac{\omega}{c}\sqrt{\frac{\varepsilon_m \cdot \varepsilon_d}{(\varepsilon_m + \varepsilon_d)}} \tag{2.4}$$

Where is ε_m is the dielectric constant of the metal and ε_d is the dielectric constant of the dielectric. From these equations it can also be shown that:

$$\sqrt{\frac{\varepsilon_m \cdot \varepsilon_d}{(\varepsilon_m + \varepsilon_d)}} \geq \sqrt{\varepsilon_d} \tag{2.5}$$

Looking back at these formulas we can now elucidate some important properties of the surface plasmons. A surface plasmon wave is a bound, nonradiative (i.e.,evanescent) wave which has a maximum at the interface between the metal and dielectric and decays exponentially into both materials which is schematically illustrated in figure 2.1

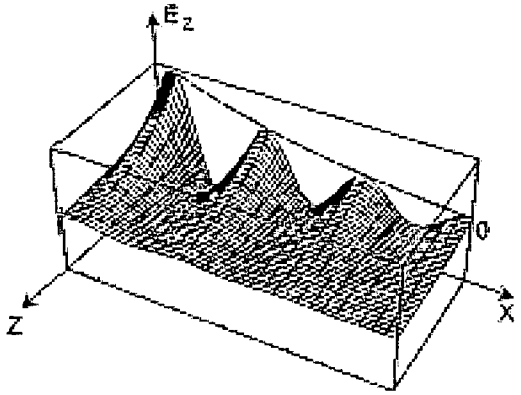

Figure 2.1: Schematic representation of the evanescent decay of a surface plasmon wave at the surface of a metal. The surface represents the intensity of the wave in the x and z directions on a metal [61]

Up to this point the discussion has missed a very important concept concerning surface plasmon resonances. Figure 2.1 is the theoretical representation of what the resonance might resemble if a photon impinging directly on a metal surface was able to excite a resonance. In reality, however, it is impossible to excite a surface plasmon resonance by direct illumination onto the surface of a metal, as described here, and an alternative method must be used in order to generate them.

With this in mind, an important point arises when examining the equation of the momentum of a photon k_{ph} in a dielectric medium. This is:

$$k_{ph} = \frac{\omega}{c} \cdot \sqrt{\varepsilon_d} \qquad (2.6)$$

and the component that is available to excite the surface plasmon mode is:

$$k_{ph}^{x} = k_{ph} \cdot \sin\theta \qquad (2.7)$$

Where θ is the angle between the incident photon and the surface. This means that the momentum of the photon propagating at the interface between the metal and the dielectric will always be smaller than the momentum of the surface plasmon mode, and hence we will be unable to excite a resonance. Even if we adjust the angle at which the light impinges on the surface so that it arrives at a grazing angle, and use the entire wavevector it still is not possible to excite a surface plasmon resonance. In order to circumvent this problem and create a surface plasmon resonance between the metal and the dielectric we use a high index prism, where $\varepsilon_{prism} > \varepsilon_{dielectric}$, to couple the light into the metal by using the evanescent wave of the photon impinging at the surface of the prism that is closest to the metal surface. This is possible, as can be seen from equation (2.6), because, exploiting the high index of refraction of the prism, we can have photons with a momentum that is of sufficient magnitude to excite the surface plasmon resonance in the metal. This is achieved by using either the Otto configuration or the Kretschmann configuration, as shown in figure 2.2. At this point, we can now understand what sort of readout we should expect from a conventional SPR device and how it works as an analytical device. Since the component of momentum vector that is coupled into the evenescent wave changes with the angle the light impinges on the prism/metal interface, we would expect that, at angles where the momentum vector of the electromagnetic wave matches the surface plasmon mode, we should get a reduction in the reflected intensity since the light is being coupled into the metal. Figure 2.3 shows the reflected intensity versus angle of a typical surface plasmon resonance device and it obeys this prediction.

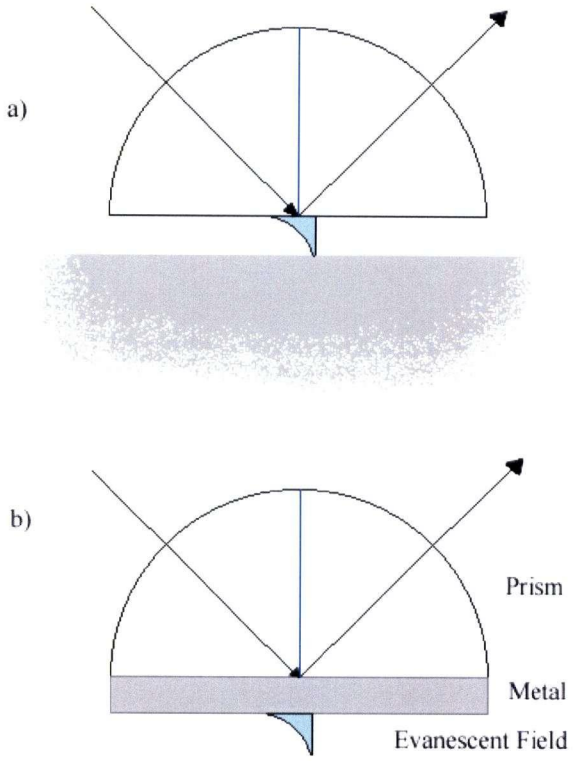

Figure 2.2: a) The Otto Configuration of Surface Plasmon Resonance induction. A prism is separated from a metal surface by a distance smaller than the wavelength of the light. b) The Kretschmann Configuration. A prism is plated with a layer of metal on the order of 50~100nm in thickness. The arrows represent the incoming photon beam being used to excite the surface plasmon resonance.

Insight into the utility of SPR as an analytical technique comes by examining equation (2.4) where we can see that the momentum required to excite a surface plasmon mode changes if the dielectric constant of the dielectric material changes and thus the angle at which the surface plasmon resonance occurs should also change. This is extremely important because if we are able to adjust the local dielectric constant of the medium near the metal we will be able to observe a change in the resonance angle. This behavior is the

basis of how SPR sensors detect small refractive index changes due to the presence of an analyte at the surface of the metal

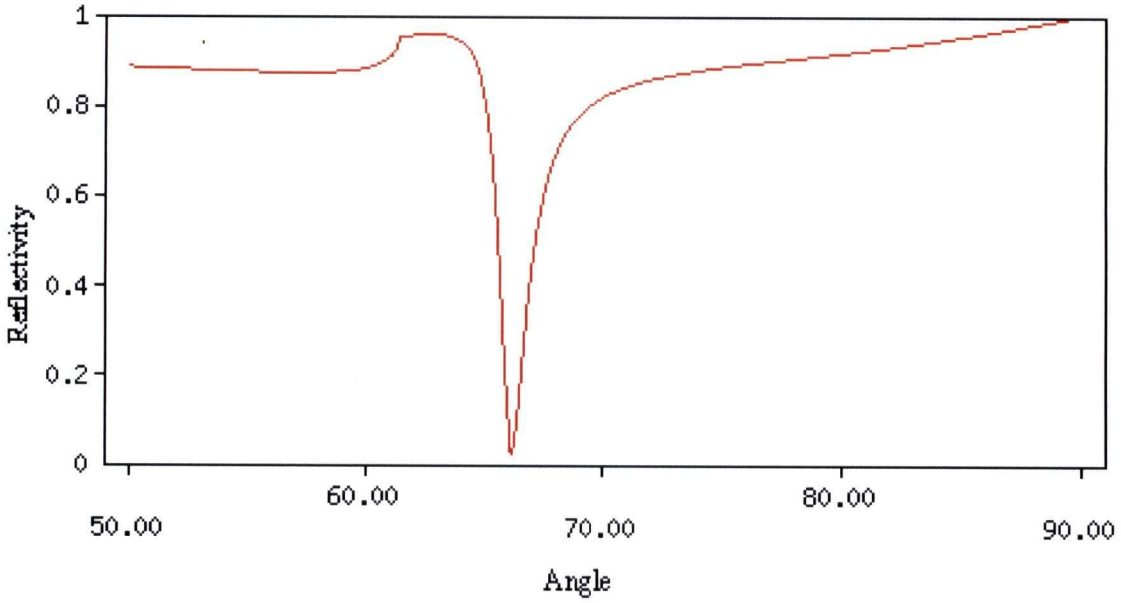

Figure 2.3: Typical SPR readout of reflectivity versus angle as calculated by a web based program[132]. Where the angle is determined between the incident beam and the normal to the metal surface. The curve represents the proportion of the incoming beam being reflected at different angles.

2.3 Typical SPR Devices and Current Uses

Most SPR systems are schematically similar to the one shown in figure 2.4[63]. This configuration, known as the Kretschmann configuration, is the preferred geometry of SPR devices. In figure 2.4, *p*-polarized light is focussed on the surface such that the incident rays subtend a subset of angles and the reflected beam shows a marked decrease in intensity at those angles which couple radiant energy into the surface plasmon modes.

Alternatively, a collimated beam of light can be impinged on the surface and the angle of incidence of light can be changed while

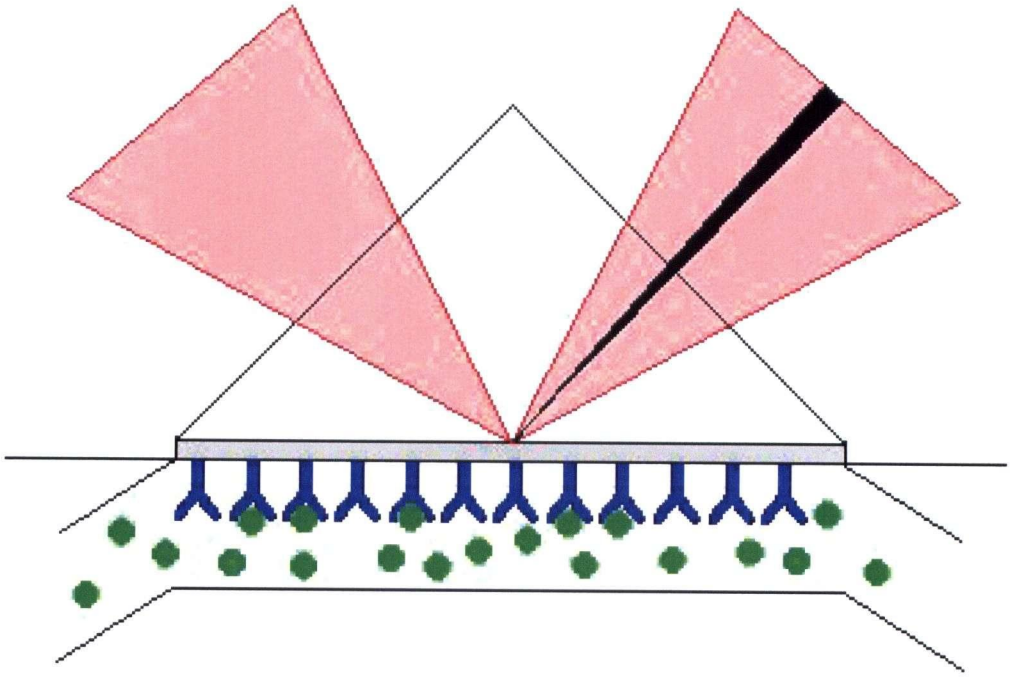

Figure 2.4: A schematic representation of a typical SPR device. The blue antibodies represent the immobilized surface species and the green dots represent the intended target molecule. Only the intended analyte will bind to the surface. Light impinges on the surface over a range of angles and only light that is at the appropriate angle to excite a surface plasmon resonance will be coupled into the surface. As the number of analyte molecules bound to the surface changes so does the local dielectric constant and consequently the angle at which light may be coupled into the surface also changes.

monitoring the reflected intensity. In general, a typical kinetic SPR experiment involves binding a ligand to the metal surface of the SPR device (pictured as an antibody in figure 2.4), a binding partner is passed through a flow cell over the surface of the metal and the reflectivity is monitored versus time[63]. This is repeated several times with varying concentrations. A popular readout method involves holding the angle of incident light constant and monitoring the intensity of reflected light over time. A plot of the reflected

light intensity (typically normalized the incident light intensity) versus time is called a sensorgram. Information about the rate constants, binding constants and a variety of other information can be extracted from these sensorgrams.

One of the important characteristics to recognize when using SPR is that the technique is unable to discern between specific and non-specific adsorption of substances onto the measurement surface. Since the surface plasmon resonance angle will change if a species is in close enough proximity to the surface to alter the local index of refraction of the surface, between 100 nm and 500 nm depending on the wavelength[59], this will result in changing the angle at which a specific wavelength of light may be coupled into the surface. In this case, a change of angle may be observed even if a species is not selectively binding to its appropriate ligand but is merely touching the surface of the metal. Because of this fact, a lot of bioanalytical method development has been undertaken in order to address errors relating to the non-specific nature of SPR measurements.

A variety of applications have been designed for surface plasmon resonance. By far, the bulk of the applications of SPR have focussed on examining biomolecular interactions. Kinetic and binding studies of proteins, anti-bodies and DNA have yielded very insightful information into the binding properties of these systems [57-58,60,63-67].

2.3.1 Surface Plasmon Resonance Imaging

Of particular interest to the current work is the recent development of Surface Plasmon Resonance Imaging[68-74]. SPR imaging involves impinging *p*-polarized light over a surface and then imaging the reflected light onto a CCD device instead of a one-channel

detector. The read out is a 2-dimensional image of the area illuminated by the impinging light, as shown in figure 2.5

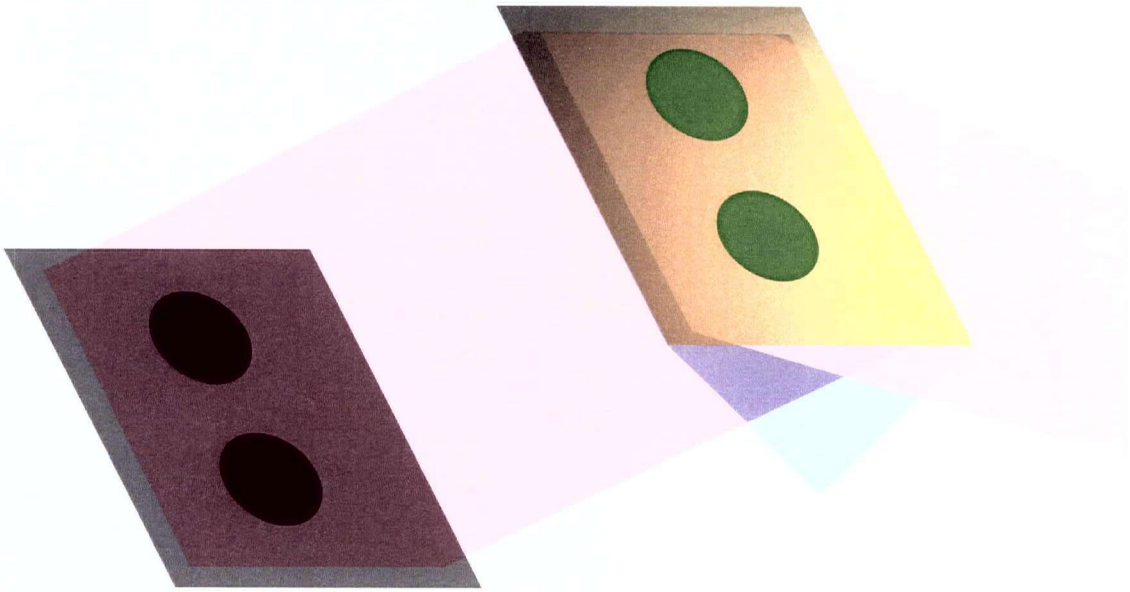

Figure 2.5: A schematic representation of SPR imaging. A beam of light impinges on the gold surface and regions where substrate contacts the metal reflect at a reduced intensity.

The interest in developing SPR imaging technology is due to trends in emerging bioassays, like DNA microarrays. Current microarrays use florescent probes to readout bound analyte molecules. This is problematic since fluorescent groups bleach, don't necessarily bind stoichiometrically and can conceivably alter the binding characteristics of the intended analyte. Although these assays are still very useful it is not possible to get accurate analytical data from them. The advantage SPR imaging brings to such

applications is that it can offer label-free detection while still being very sensitive. Further discussion of DNA microarrays will be presented in subsequent sections of this thesis.

Chapter 3

Introduction to DNA Microarrays

3.1 Historical Development of DNA Microarrays

Simply put, DNA microarrays are 2 dimensional arrays of single stranded oligonucleotides, cDNA or cDNA fragments bound to a planar glass, silicon, polymer or metal surface, as shown in figure 3.1.

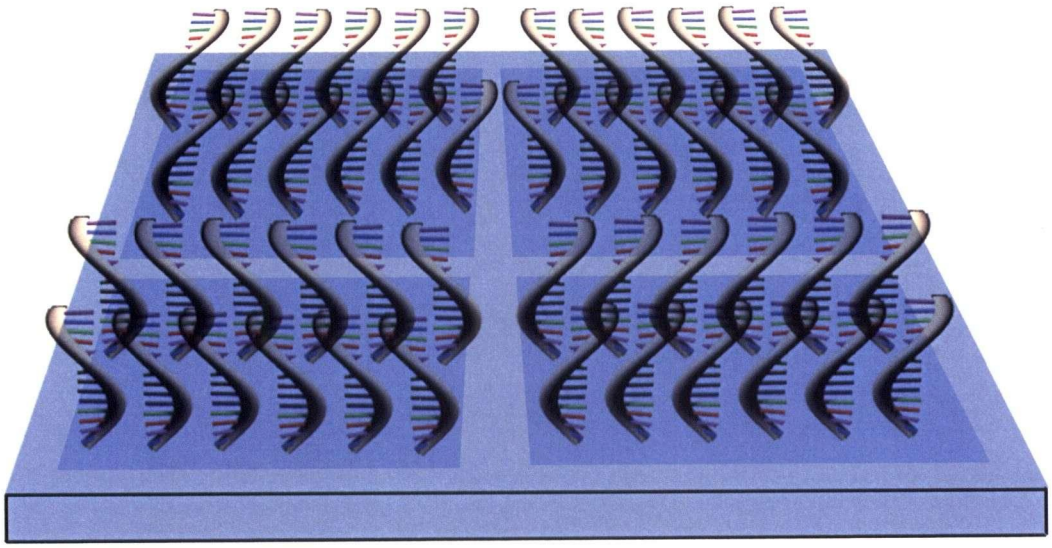

Figure 3.1 A schematic representation of single stranded pieces of DNA bound to a glass substrate. In a conventional microarray, all of the individual probes attached to each cell (or register) of the array would be a known and different sequence of DNA.

To analyze a sample of cellular DNA, mRNA or cDNA for the presence of a specific genetic sequence using a DNA microarray, the analyte sample is usually reacted with a

fluorescent tag and then it is exposed to the surface of the array under conditions that allow hybridization of complementary sequences[74]. Any genetic sequences in the sample that are complimentary to those found on the array should bind and should then be immobilized on the array surface. After rinsing the array they are usually read by an imaging fluorimeter. The readout of a typical microarray is shown in figure 3.2.

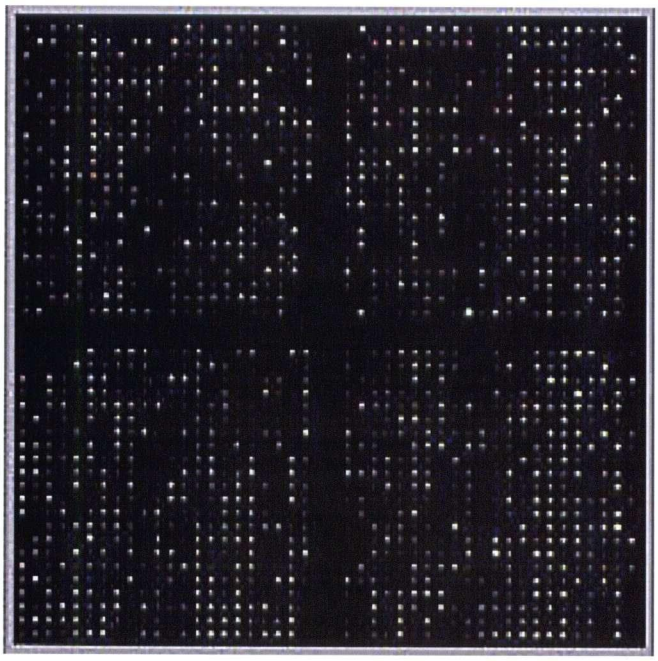

Figure 3.2 The fluorescent readout of a DNA microarray. Each spot indicates that a complimentary portion of fluorescently tagged DNA has been bound. The varying intensity of each dots indicates the amount of complimentary DNA in the sample[75].

The intensity of each spot is measured and can be used to acquire semi-quantitative and qualitative information from the array.

DNA microarrays have emerged in the last decade as an important tool for genetic analysis. The history presented here follows Chapter 1 of Methods in Molecular Biology, vol. 170: DNA Arrays: Methods and Protocols[76]. Like the development of many other

technologies, DNA microarrays have resulted from the maturation of multiple techniques that coalesced to form a powerful new tool.

The infancy of DNA microarrays began soon after the structure of DNA by Watson and Crick. The idea of sequence complimentarity offered the possibility of the analysis of DNA and this idea was studied extensively. A major step in the development of arrays came in the 1960s when Fluorescent In-Situ Hybirdization (FISH) was demonstrated. FISH involves labeling fluorescently labeled probes that identify specific sequences of DNA on chromosomes. Another major discovery came in the mid 1970s when Grunstein and Hogness[77] discovered a way to lyse and fix DNA from bacterial colonies to a membrane.

The idea of large scale analysis of multiple DNA sequences came in the 1980s and followed from the production of bacteria and yeast cell clones. Clones were initially organized onto microtitre plates and subsequent analysis was performed to find critical information about the genetic sequence of the clones. It was Hoheisel et al.[78] who advocated putting multiple libraries on filters at high density in order to cross-correlate sequences. Kafatos et al.[79] were the first to analyze multiple hybridization targets in parallel by putting them on a filter in a defined pattern, now known as a dot blot. This technique was not only able to hybridize in parallel but also to analyze in parallel which represents a huge step in the development of arrays. Automization followed this development and the density and reproducibility of these dot blots was drastically increased.

Dot blots involve attaching sequences of unknown DNA to membranes and then using known DNA probes to analyze the sequence. Reverse dot blots approached more modern array methods by attaching the known DNA probes to the surface of the

membrane and labeling and hybridizing the unknown sequences. The major difference between these reverse dot blots and modern arrays is that modern arrays have the known probe DNA sequence bound to solid supports. Solid supports offer many advantages over membranes. Besides the inherent advantages of being significantly more robust in the face of physical contact and solvent exposure, there are other important differences that exist. Methods of producing microarrays on solid surfaces are capable of ensuring that the amount of DNA placed on a chip is consistent from one region to another. Membranes are much more fragile then solid supports and can deform when subjected to solvents and drying.

The development of solid state organic chemistry techniques was also a tremendous aid in the development of microarrays. The ability to produce complex nucleic acids on solid supports has been integral in the development of certain kinds of arrays. It was Letsinger et al.[80] and Beaucage and Caruthers[81] that lead the development of techniques for producing nucleic acids using the solid-phase method. Modern techniques for synthesis of DNA on solid supports can create long strands and sequences as long as 200 nucleic acids have been achieved, however, anything longer than 30 will likely contain too many errors to be very accurate for detection.

3.2 Manufacturing of DNA microarrays

There are a few competing methods for the manufacturing of DNA microarrays. The first commercially available high-density microarrays involved using photolithographic techniques coupled with solid-phase *in situ* synthetic chemistries to create probe sequences on the surface of the DNA microarray, also called a chip [74-75,83]. Photolithography, a commonly used technique in electronics manufacturing, is a solid-

phase multi-step process which uses a combination of masks, light and chemicals to pattern a silicon surface has been adapted for use in microarray[83]. Initially, the surface of glass is derivatized with a light reactive material. Photolithographic masks are created which expose certain regions of the chip to ultraviolet light. Once exposed to light, the selected surface becomes "activated" and will react with selected reagents that are washed over the surface. Steps are taken to react one particular nucleic acid to all the "activated" sites on the surface of the chip. Once the nucleic acid has been "attached" to the surface it is protected with another light reactive material. The process is then repeated with differing masks until the desired sequence of nucleotides is achieved over the entire chip. This process is visualized in figure 3.3.

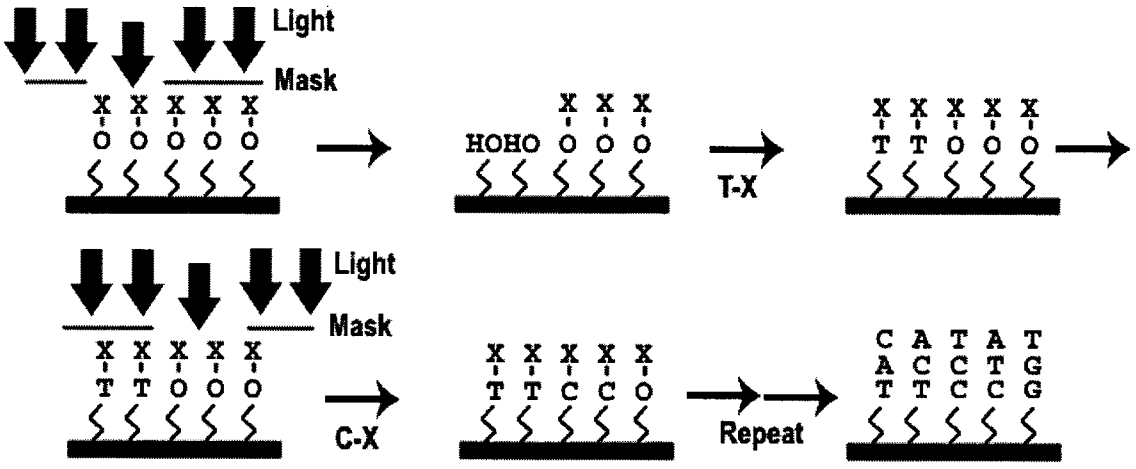

Figure 3.3 The schematic representation of the lithographic method of DNA microarray manufacturing. A,C,T,G represent the bases, X is a photolabile chemical bound to the surface of the slide or to the bases. Light impinges on the derivitized surface and de-protects uncovered regions. The surface is then reacted with a derivitized bases that bind to the unprotected regions. The process is repeated until the desired surface is reached.[83]

One method of producing DNA microarrays is by using microprinting technology. Microprinting of DNA microarrays stems directly from technology developed by the printing industry. Printing heads developed for high-quality document production have been adapted for use in microarray manufacturing. Printing is achieved either by spraying the solution out of a miniature nozzle, like an inkjet printer, under high pressure, or by spotting the DNA onto the surface by using a needle "quill" tip[74,75]. The later involves using needle tips that are essentially tiny pen nibs. The design of the needle alters the spot size and spot volume although typical spotting volumes are less than 1 nL. Since the spot size can be affected by DNA concentration, in order to achieve desired DNA density at each probe site while maintaining an appropriate spot size, each location is spotted multiple times until the desired density is reached. The DNA sequences are chemically bound to the surface of the glass using various chemical approaches[74,75]. Although printing technology can be used for any DNA sequence it is often used to create arrays made of cDNA.

There are a few advantages of using photolithographic methods over microprinting technologies. The first being that they are capable of accommodating very high probe densities with very precisely defined (albeit short, <20 nucleotides) sequences. This allows the investigator to explore thousands of probes simultaneously. Short oligonucleotides also make it possible to detect variations between DNA sequences of as little as one base pair[84]. In spite these advantages, there are drawbacks to photolithographic techniques. Photolithography is expensive and may not be feasible in an academic setting. Other disadvantages of oligonucleotide arrays result from the inherent method of fabrication[84]. Since the oligonucleotide sequences are chosen prospectively, there is the very real possibility of not detecting desired but unknown

sequences. High probe density, an advantage of these chips, can also be a hindrance since the sequences are short and highly variable which means that the thermodynamics of hybridization are highly variable within the probe population of the array[85]. This limits the ability to compare binding globally throughout the array.

Microprinting methods offer a completely unique set of characteristics. Since printing technology is so readily available, microarrays produced by this method are much less expensive than photolithographic methods and as a result are much more feasible for laboratories with financial constraints[84]. A clear advantage of these arrays is that they can spot fragments of DNA of any length, including full length cDNA, Another advantage of this is that scientists can spot any sequence, known or unknown, to the surface and monitor hybridization. This adds a high degree of flexibility to experiments. Despite all the advantages of DNA microprinting there are definite pitfalls of this technology. Although spotting larger DNA sequences offers flexibility it also introduces the possibility of probe-target mismatches. This means that the analyte being examined may bind to one or more DNA sequences on the chip which may introduce error if the experiment is not designed correctly[84]. The printing process is also a variable that can affect experimental outcome. The amount of DNA printed on the surface can affect the intensity of the output signal. Care must be take to ensure that DNA concentrations are optimized and consistent across slides in an experiment since this may greatly affect experimental outcomes. Another hurdle facing slide manufacturing is that evaporation of solvent while printing may lead to significant variability of the DNA on the slide which can be a significant source of error[84].

3.3 Experimentation and Readout of DNA Microarrays

Experimentation using DNA microarrays depends highly on the system to be studied. Typically, the gene sequences to be studied are selected and an array is manufactured to include the genes of interest. To aid in analysis, each probe is spotted at multiple locations throughout the array in an attempt to account for variability encountered in the hybridization.

Once the chip has been manufactured, the samples to be analyzed must be prepared for detection. Microarrays depend on tagging DNA samples with fluorescent dyes for detection. Typical fluorescent dyes used to tag DNA samples include the green fluorophore Cyanine 3 (Cy3) and the red fluorophore Cyanine 5 (Cy5)[88]. One of the major drawbacks to fluorescent tagging is that the number of dye molecules that bind to a particular DNA sequence can vary. This issue manifests itself in analysis since this variation adds inaccuracy to the quatitation of bound DNA. After tagging, the samples are incubated with the arrays under controlled conditions that favor only Watson-Crick duplex formation and given time to hybridize, then the chips are rinsed with buffer to clear unhybridized sample DNA.

As previously explained, readout consists of placing the probes into an instrument that illuminates the probes with the appropriate wavelengths and images of the surface of the array are taken at each excitation wavelength. Once the image is acquired the data on the chip must be analyzed in order to acquire useful information from the chip. Data analysis and interpretation has proven to be one of the major hurdles that researchers in this area face. In order to get useful information from arrays the raw images must first be processed and then interpretation of the data must commence to make biological sense of the information aquired. Due to the high volume of information on microarrays raw data

processing is done by computer. Image processing involves a few steps which include locating the individual spots, determining the boundary of the spots, measuring the fluorescent intensity of each spot, subtracting background intensity and normalization of signal intensity[84]. Each one of these steps has unique problems associated with it and since there is no universally accepted standard that all scientists use it can make comparing array data from different laboratories very difficult. Normalization, in particular, has been one of the most systematic sources of error within experiments due to variability with fluorophores[86]. In some experiments, one analyte is labeled with two separate fluorophores while in other experiments two analytes are labeled with different fluorophores and hybridized on the same chip. Each fluorophore is read out separately with a separate wavelength of light and in order to compare the information garnered by the separate readouts of the two fluorophores the signal intensities of the two fluorescent tags must be normalized between themselves. This is difficult since not only does each fluorophore have unique emission characteristics but fluorescent intensity may vary from feature to feature. Complicated mathematical algorithms are being developed in an attempt to battle this issue[86,87] but the reality remains that most information garnered by microarrays is qualitative and not quantitative.

3.4 Surface Plasmon Resonance Microarray Systems

As previously mentioned, one of the disadvantages of using current DNA microarray technology is the use of bound fluorescent probes for chip readout[89-91]. As illustrated in the previous section there are groups that are attempting to combat the pitfalls of fluorescent probes but the heart of the issue results from inherent pitfalls of using fluorescent tags[88,84] . One approach to this problem has come from the Surface

Plasmon Resonance community. As mentioned, SPR detection depends on a local change of index of refraction at the surface of a metal and this technology is ideal for creating microarrays that do not require fluorescent tag attachment. As demonstrated in the previous chapter, SPR has already proven itself to be very sensitive and by incorporating this technology into microarrays and eliminating the problems associated by fluorescent tag attachment, the acquisition of quantitative information from microarrays is very feasible as long as care is taken to avoid non-specific adsorption and surface contamination at the surface of the chip. A number of groups have taken the lead in the development of these chips[92-96]. Although these SPR arrays are currently only capable of detecting approximately 100 sequences simultaneously, with further development it will certainly be possible to begin to achieve densities that rival currently used microarray technologies.

3.5 Applications of DNA microarrays

The use of DNA microarrays has grown dramatically since their invention. It is understandable that any tool that is able to analyze a large amount of genetic material has a tremendous amount of applications. A few of these diverse applications includes the global analysis of gene expression of organisms, the genetic screening for cancer and other diseases, the identification of pathogens, and for drug design and drug discovery[97-104]. The work presented herein attempts to build on the already tremendous applications of microarrays and to further the usefulness of SPR microarrays. By combining Raman Spectroscopy and SPR microarrays, the aim of this thesis is to provide researchers with the added information from Raman spectroscopy to help analyze microarray information.

Chapter 4

Materials and Methods

4.1 Introduction

The materials and methods used in the experiments performed in this work will be presented here. Both the ultraviolet resonance Raman fiber-optic spectrometer used in our lab and the Renishaw Model 1000B Raman Microscope will be described. The design and construction of an SPR imaging device will be undertaken in a subsequent chapter. Finally, the expression and purification of Cytochrome c Peroxidase and the mutant Cytochrome c Peroxidase W191F will be presented in this chapter .

4.2 Ultraviolet Resonance Raman Fiber Optic Spectrometer

4.2.1 Ultraviolet Laser Source

The laser source employed in this experiment was a frequency-doubled Argon ion laser (Coherent I-90 FreD, Santa Clara, CA)which utilizes an intracavity BBO crystal. By using various BBO crystals, the laser is discretely tunable at UV229.0, 238.2, 244.0, 248.2, 250.8, 257.2 and 264.3 nm.

4.2.2 Detectors

A thermoelectrically cooled CCD camera (SpectraVideo, Pixelvision of Oregon, Inc., Beaverton, OR) and a liquid nitrogen cooled CCD camera (Spec-10:400UVB, Roper Scientific, Trenton, NJ) were used in the present work. The later was on loan from Roper

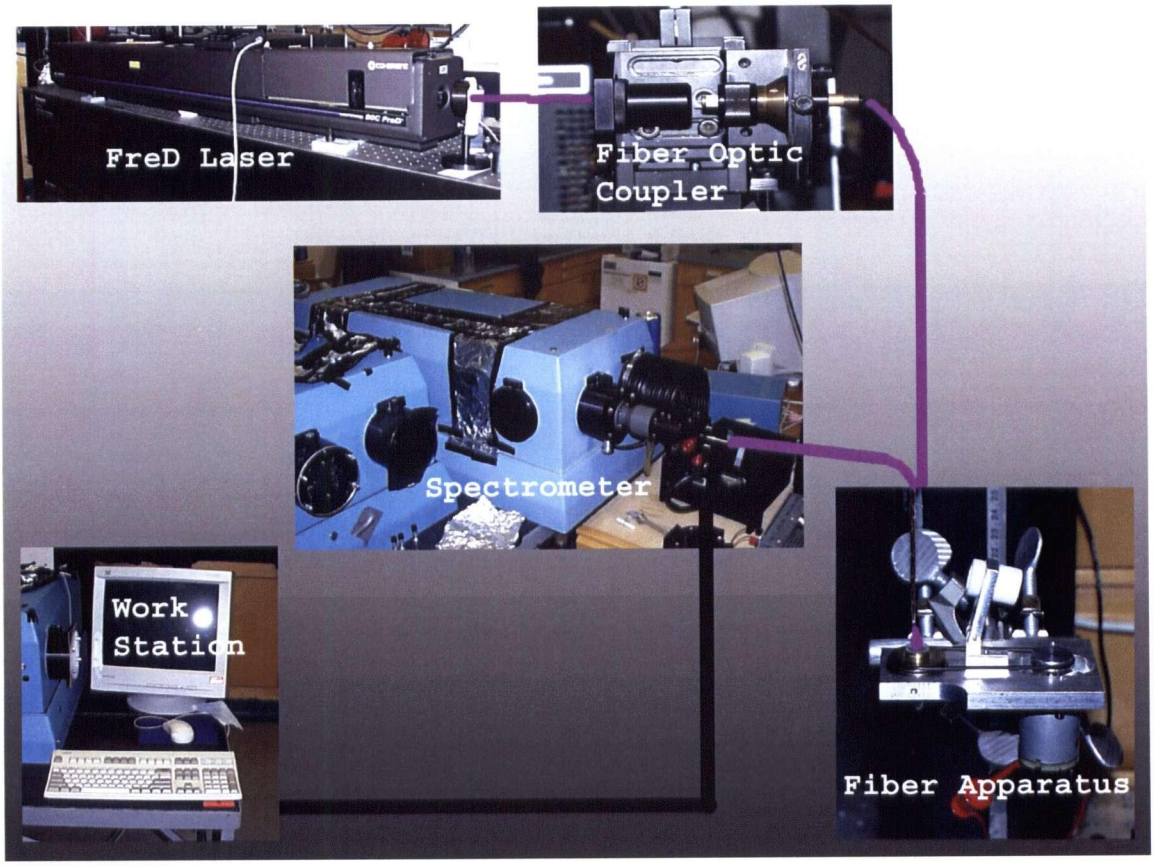

Figure 4.1: Photographs of various components of the setup of the UV/Vis fiber optic Raman spectrometer used to perform the experiments. The laser originates in the FreD laser is coupled into a fibre optic probe using a fibre-optic coupling assembly. The beam is transmitted into the sample. Light is collected by the fibre optic collection fibres and it directed into a spectrometer. The data is collected and analyzed at the computer work station.

Scientific for evaluation and despite it's favorable performance characteristics was only available for a limited period.

4.2.2.1 Thermoelectrically Cooled CCD Camera

The SpectraVideo camera uses a thinned back-illuminated CCD array which is coated with a UV anti-reflection coating. The array is 1100x330 pixels and each pixel measures 24 μm^2. The camera is equipped with an externally mounted water-cooled Peltier effect device that was installed after delivery and a nitrogen purge which was added to the camera to avoid the condensation and ice formation. The camera is normally cooled to $-51^{\circ}C$ during data acquisition. When last tested in April of 2003, the dark current at $-23^{\circ}C$ was measured to be 6.42 electrons/pixel/second and the readout noise was 19.9 electrons per readout at 50kHz.

4.2.2.2 Liquid Nitrogen Cooled CCD Camera

The Spec-10:400UVB Camera is a back-illuminated CCD array with a UV enhancement coating. The array consists of 1340x400 pixels and each pixel is $20\mu m^2$. The quantum efficiency of the camera between 200 nm and 300 nm is approximately 45%. The camera is cooled by liquid nitrogen and was operated at $-116^{\circ}C$. The dark current of the camera is reported to be 0.3 electrons/pixel/hour and the read noise at 50 kHz is 2.8 electrons per readout.

4.2.3 Wavelength Separation

Wavelength separation was achieved through the use of a 1.0 meter Czerny-Turner design single monochromator (McPherson Model 2061, Chelmsord, MA). The

grating employed was a 3600 grooves/mm holographic grating. Fiber-optic collection fibers were coupled to the monochromator through the use of a fibre-optic adapter (FPH-DJ, Newport Corporation, Irvine, CA) and with a chuck built to hold six collection fibres in a vertical column. The adapter was employed to match the f-number of the fibers to that of the monochromator and was modified by changing the lenses and adding a spacer. The slit width was chosen to be 200μm since this allowed a good signal throughput while maintaining adequate spectral resolution.

4.2.4 Fibre-Optic Multi-Fibre Ultraviolet Resonance Raman Probes

Fiber optic probes were first created and used in our lab by Greek[105] and have evolved into a multi-fiber geometry. The ends of six UVMI fiber-optics (Polymicro Technologies, Phoenix, AZ) of 400μm are beveled to 45° using a fiber-optic grinder and polisher (Ultrapol, Ultratec Manufacturing Inc., Santa Ana, CA) using various grades of polishing paper while the other end is polished flat. The beveled end is dipped in photoresist and the angled portion of the fiber is exposed using methanol. Aluminum is vapour deposited onto the end of the fibers in a vacuum chamber (CHA Industries model SE-600-RAP, Menlo Park, CA). Once the aluminum has been deposited, the photoresist is removed and the fibers are positioned around a 600μm diameter excitation fiber using silastic tubing cut into small collars. The mirrored faces were rotated to face the excitation fiber and then were glued into position using medical grade silicone (Medical Adhesive Type A, Dow Corning, Midland, Michigan). The arrangement is presented in Figure 4.2.

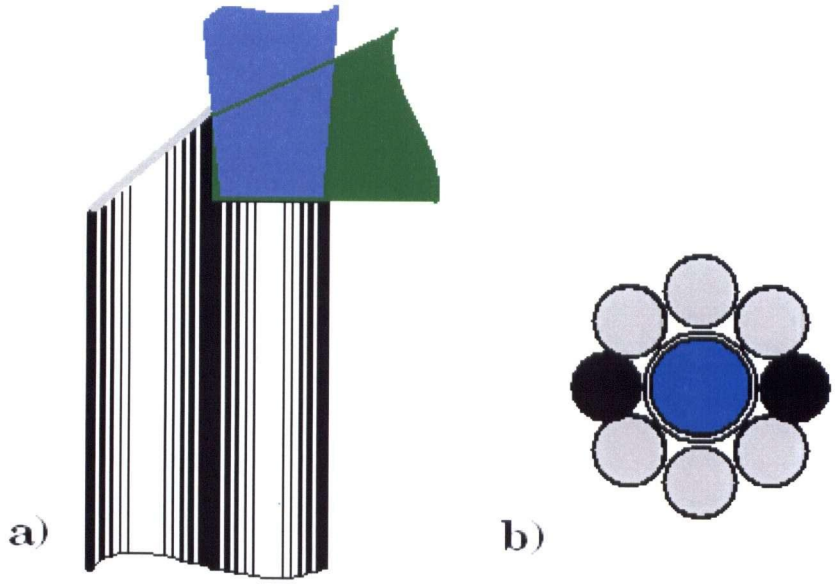

Figure 4.2: a) The side view of the alignment of a single collection and a single excitation fibre. The excitation volume is depicted in blue and the collection volume is indicated by green. b) The top view of a bundle of six collection fibres surrounding the excitation fibre. The gray circles are collection fibres that have been angled and aluminized while the black circles are short spacers which are designed to allow flow over the face of the excitation fibre.

4.2.5 Data Collection and Signal Processing

4.2.5.1 Computer Hardware and Software

The computer used to control both CCD cameras was an Intel 233 MMX based personal computer. The software used to control the SpectraVideo Camera was PixelView (PixelVision, Beaverton, OR) and the software used to control the Spec-10:400UVB was WinSpec32 (Roper Scientific, Trenton, NJ). All files collected with either program were converted to the .SPC format and all data processing was done with Grams32 v5.1 (ThermoGalactic, Salem, NH).

4.2.5.2 Wavenumber Calibration

Although reasonably constant, changes in the local environment, like temperature, humidity, can introduce variability in the position of observed peaks during data acquisition. For this reason, wavenumber calibration must be performed for each individual experiment. This is achieved by measuring the spectrum of neat ethanol as prescribed by Ferraro and Nakamoto[2]. The pixel positions of the ethanol peaks were plotted versus the known wavenumber peak positions and were fitted to a quadratic. The quadratic relationship was then applied to each spectrum using Grams32.

4.2.5.3 Background Removal

Since the excitatory beam passes through a silica optical fiber before exciting the sample, Raman scattered light from the excitation fibre may be collected under certain experimental conditions and contribute to noise in the data. Although, typically, not intense, the removal of silica signal is important when analyzing data. This was accomplished by fitting a spectrum of silica, collected from the fibres exciting a reflective surface, and using the subtraction to remove the silica signal. The fitted silica signal is shown in Figure 4.3. The background signal of the camera was not subtracted since it did not prove to present any major interference, although it was monitored during each experiment to be certain.

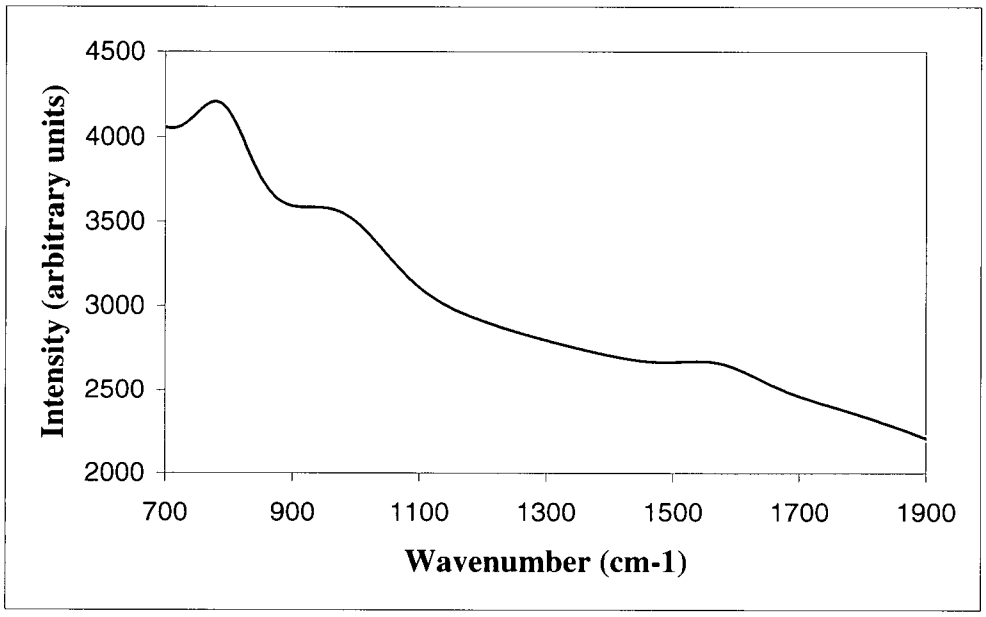

Figure 4.3: The Raman spectrum of silica scatter collected at 248.2 nm.

4.2.5.4 Internal Standard

Sodium Sulfate was used as an internal standard in this experiment spectral subtraction. The sodium sulfate spectrum does not overlap with any of the transitions of interest, [106]. and does not interfere with the enzymatic properties of CcP or CcP W191F.

4.3 Renishaw Model 1000B Raman Microscope and Laser Source

4.3.1 Laser Excitation Source

The laser excitation source was a Titanium:Sapphire($TiAl_2O_3$) multi-component laser system from Coherent Inc. (Santa Clara, CA). The laser is pumped by a solid-state diode-pumped frequency doubled Neodynium Vanadate (Nd:YVO_4) laser (Verdi V-10, Coherent Inc., Santa Clara, CA). The emission from this laser is 532 nm and has a maximum power of 10W which is directed into the Titanium:Sapphire cavity (Mira

Model 900, Coherent Inc., Santa Clara, CA). The Mira offers continuously tunable emission from 700 nm to 1000 nm and the emission of the laser and can be operated in a continuous wave mode or modelocked to operate with either picosecond or femtosecond pulses. For this study the laser was tuned to 785 nm and was in continuous wave mode. The power at the sample was held at 34 mW.

4.3.2 Renishaw Model 1000B Raman Microscope

4.3.2.1 Renishaw Model 1000B Raman Microscope Hardware

The Renishaw 1000B Raman Microscope (Renishaw, Hoffman Estates, IL) is, simply put, a microscope with a built-in spectrometer and thus allows the acquisition of Raman spectra from samples placed under the microscope objective. Light enters the spectrometer portion of the instrument and is directed through the main case, beam expanded with 2 microscope objectives and finally impinges on the first of a set of holographic notch filters. Although notch filters are designed to reject light, in this Raman microscope they are initially used to direct light into the microscope without rejecting the incoming beam. The excitation light is reflected by the first notch filter and is directed into the microscope section of the instrument. The light passes through a Leica DMLB microscope with 5x, 20x and 50x objectives and the sample is mounted on an automated translational stage. The stage inset can be removed and replaced with custom insets, which was an SPR imager in this case. White light images can be taken of the sample using a mounted colour CCD camera. The Raman scattered light travels back through the microscope and arrives back at the notch filter setup. The holographic notch filters serve a dual purpose, coupling the light into the microscope objectives and rejecting the Rayleigh light from the sample, a large source of stray light. Since the notch

filters may give an undulating transmission profile, the combination of 2 matched filters offers a high degree of Rayleigh rejection while at the same time providing a smooth transmission profile. The notch filters in our particular instrument are designed to reject 785 nm, which was convenient for this study due to the fact that this wavelength is able to excite a surface plasmon resonance in gold, but the filters can be changed to accommodate a variety of different excitation wavelengths. Once the light has passed through the notch filters it is imaged onto the spectrometer slit and onto a 1200 lines/mm holographic grating. The dispersed light finally impinges on a thermoelectrically cooled CCD which has been cooled to –70°C. The light path is pictured in Figure 4.4. Although the instrument can be run in confocal mode to increase z-dimension resolution, this mode was not used in this study.

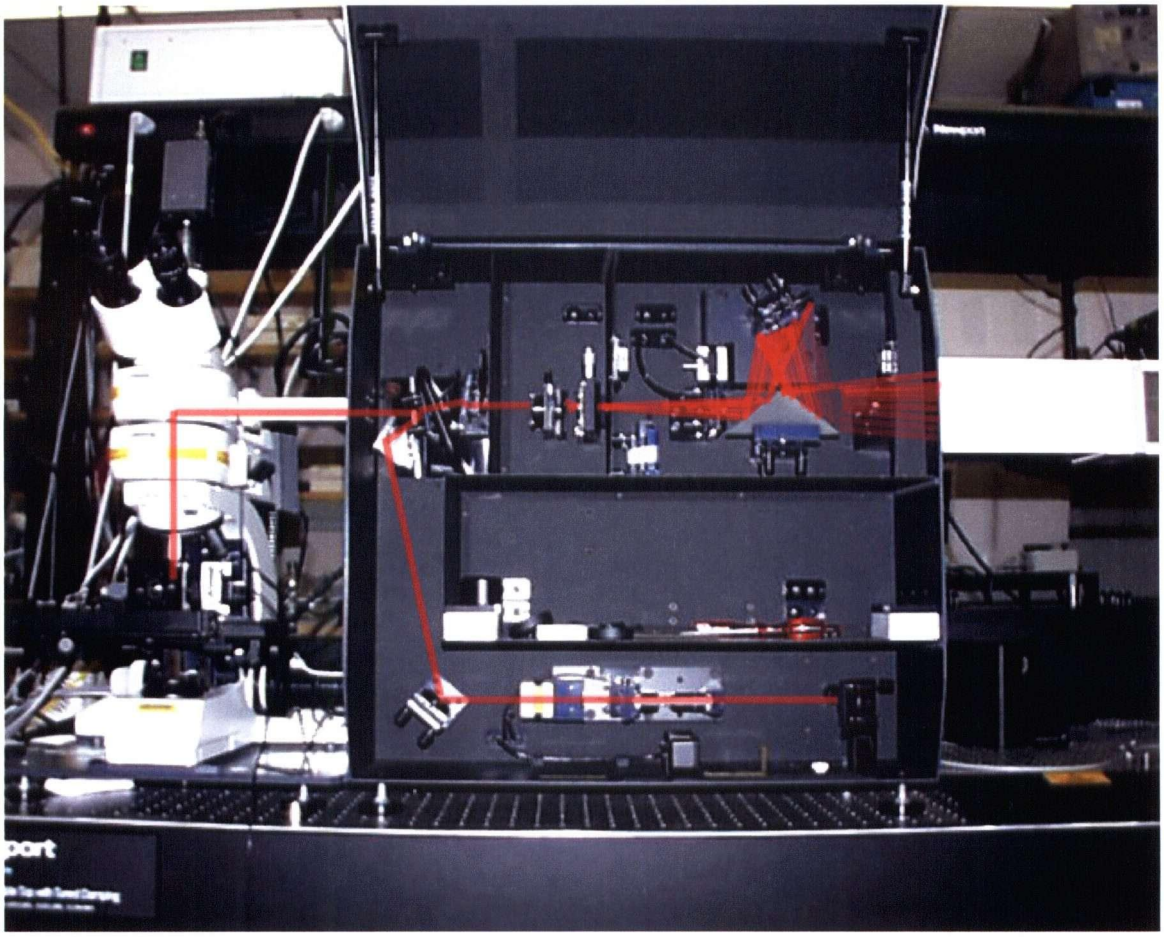

Figure 4.4: The beam path of the beam path (illustrated by the red line) of the Renishaw 100B Raman Spectrometer.

4.3.2.2 Renishaw Model 1000B Raman Microscope Software

The instrument is run on a 1 GHz Pentium III personal computer. The software used to run the microscope (Renishaw WiRE, Renishaw, Hoffman Estates, IL) runs with Grams32 (ThermoGalactic, Salem, NH). The instruments software is calibrated using a neon lamp source and a silica wafer.

Chapter 5

Investigation of Radicals in Cytochrome c Peroxidase

5.1 Introduction

Cytochrome c Peroxidase (CcP) was first discovered by Altschul et al in 1940. It is localized in the inter-membrane space of mitochondria and its main function is thought to involve the removal of toxic hydrogen peroxide. CcP is notoriously easy to crystallize and as a result in 1978 it became the first protein to have a three dimensional crystal structure taken. Another significant contribution to the scientific community came with the investigation of CcP by site-directed mutagenesis. This groundbreaking work was cited for the 1993 Nobel prize in chemistry awarded to Michael Smith. Having been the focus of such important scientific discoveries it is not surprising that this protein has been extensively studied. The following discussion of CcP will be a distillation of a variety of sources[107-110].

5.1.1 CcP Stucture and Function

The molecular weight of CcP is 35,350 g/mol and after post-translational modification is a single polypeptide chain with 294 residues. It is important for this study to note that 7 of the residues are tryptophans and 14 are tyrosines. A heme moiety is crucial for protein function and the unreacted enzyme, known as the resting enzyme, exists in the iron (III) state. The structure of CcP and it's active site are shown in Figure 5.1.

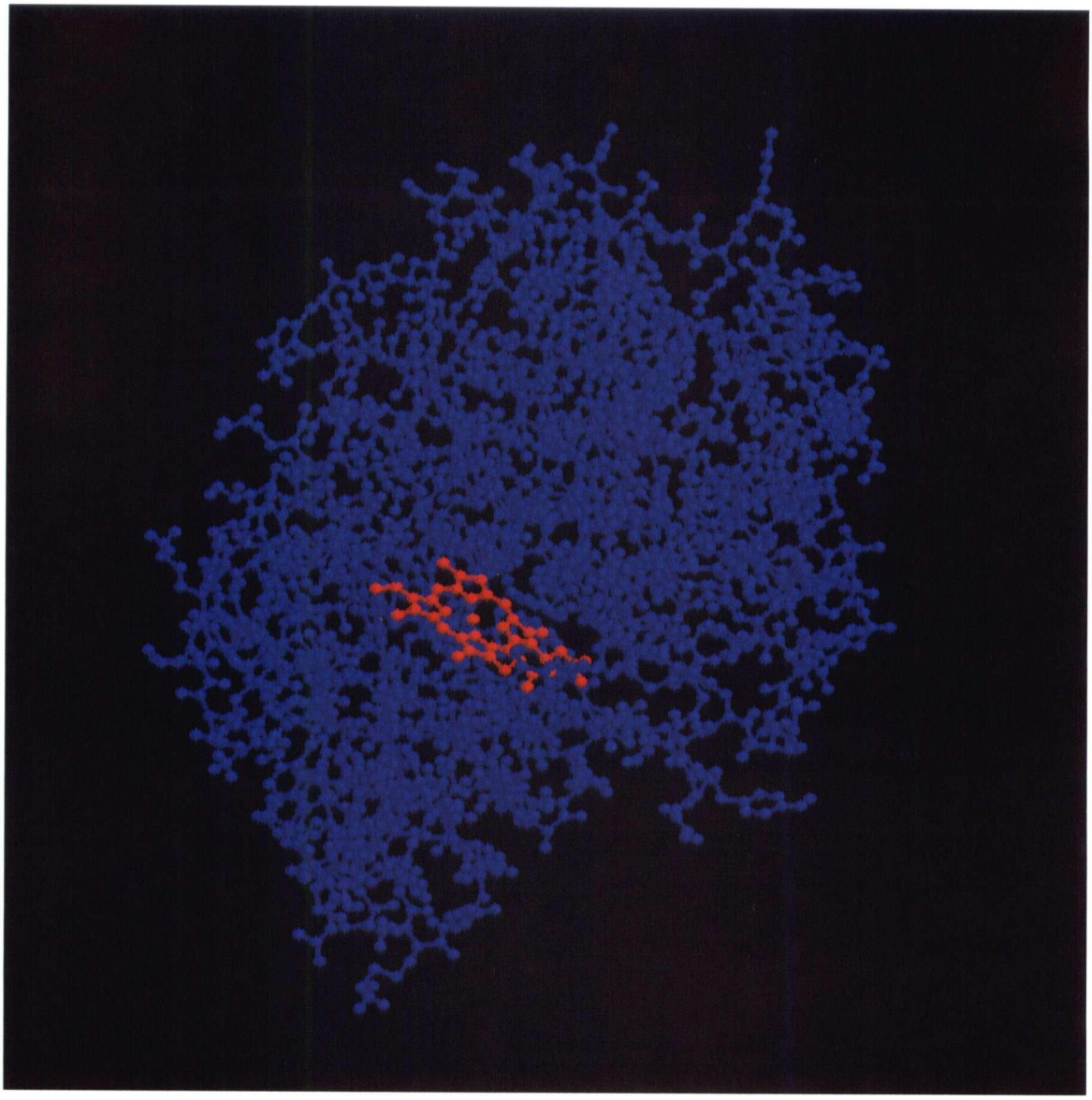

Figure 5.1: Cytochrome C Peroxidase. The red represents the Heme group in the center of the protein and is the source of the reaction.

Cytochrome c and CcP combine to form a catalytic cycle

$$CcP + H_2O_2 \rightarrow CcP\text{-}I + H_2O \quad (5.1)$$

$$CcP\text{-}I + C^{2+} + H^+ \rightarrow CcP\text{-}II + C^{3+} \quad (5.2)$$

$$CcP\text{-}II + C^{2+} + H^+ \rightarrow CcP + C^{3+} + H_2O \quad (5.3)$$

Where CcP-I is called compound I, CcP-II is called compound II, and C^{2+} and C^{3+} are different oxidation states of iron in the Cytochrome c. The formation of compound I has been the source of intense scientific research due to the formation of a radical in the protein. Many studies have been focused on elucidating the location of the radical, which was the source of an anomalous Electron Paramagnetic Resonance (EPR) signal. The source of the radical was conclusively identified in 1989 using Electron Nuclear Double Resonance (ENDOR) and was found to be a tryptophan cationic radical. Radicals are prevalent in many protein reaction mechanisms but what makes CcP interesting is that tryptophan radicals are uncommon and the radical formed in CcP is unusually stable at room temperature, lasting for approximately 2 hours and beyond. In the past 2 years it has been discovered that along with a stable tryptophan radical in CcP there are also stable tyrosine radicals in the protein. It was previously thought that the stoichiometric addition of hydrogen peroxide to the protein would only yield the tryptophan radical but this has been found not to be the case. These tyrosine radicals, located at the 39 and 153 positions, were discovered using high resolution EPR spectroscopy, and have also be found to be stable at room temperature with a lifetime of approximately 1hr. It is still unclear as to what mechanism is involved in the formation of these radicals and what role they play in enzyme activity.

Site-directed mutagenesis of CcP has yielded a variety of variants over the last 2 decades. Of interest, in this study, is the CcP W191F mutant whereby the tryptophan in the 191 position has been replaced by a phenylalanine. The mutation results in a protein with increased activity in which the radical at position 191 has been replaced by a π-bond porphyrin based radical.

5.1.2 Raman studies of CcP

As can be expected by the high profile nature of this enzyme, CcP has been extensively studied using Raman Spectroscopy and Resonance Raman Spectroscopy[110-118]. The main focus of these studies has been on the heme group in the protein. Resonance Raman in particular is uniquely useful for CcP since it can be used to selectively enhance the heme group using wavelengths that fall within the Soret band. While the crystal structure of CcP has been collected, the state of the active site is different in the crystal then in solution and a crystal structure only gives a static view of a protein. Raman has been useful in helping to elucidate the function of the heme in protein function[111,113-116,118]. Many vibrations in the low wavenumber region of Raman spectra, below 800 cm^{-1}, give important information about the heme group, like coordination number and spin state. The interaction of CcP with Cytochrome c has also been examined using Raman[110].

5.1.3 Raman of CcP Radicals

Despite having been identified and studied, the Raman spectrum of the tryptophan radical in CcP has not yet appeared in the literature. Bunte et al.[119] have calculated the theoretical Raman spectrum of the cationic radical of 3–methylindole, a tryptophan

analog. In addition to the recent discovery of the newly found tyrosine radicals, a unique opportunity exists to attempt to collect the Raman spectra of both the tryptophan radical and the tyrosine radical of CcP simultaneously. This could prove to be useful for the spectroscopic identification of similar species in other proteins or in further investigation of CcP. UVRRS is uniquely suited to observing the spectrum of the radicals in CcP because it offers the opportunity to selectively excite these species while at the same time reaping the intensity benefits and fluorescence avoidance characteristics of resonance enhancement.

5.2 Experimental

5.2.1 Expression and Purification of CcP and CcP W191F

The expression and isolation of CcP and CcP W191F performed in this thesis was based on an unpublished protocol used in the laboratory of Dr. Grant Mauk. A general overview of the procedure will be presented here and the entire procedure is listed for reference in Appendix A.

CcP and CcP W191F plasmids were obtained from the laboratory of Dr. Grant Mauk (University of British Columbia, Biochemistry Department). BL21(DE3) cells were transformed with the desired protein plasmid. For each protein, 20 liters of superbroth media innoculated with the transformed cells and the culture was grown at 37°C until the desired optical density of cells was reached. At this point isopropyl-D-thiogalactoside (IPTG) was added to induce protein expression at which time the cells were given 2-3 hours to express protein. Subsequently, the cells were harvested by centrifugation and were lysed using lysozyme and flash freezing in liquid nitrogen. Phenylmethylsulfonyl Fluoride (PMSF) was added to inhibit protease activity. DNAase

and RNAase were added to degrade the DNA and the ribonucleic acid (RNA) in the mixture. Once the cells were lysed all subsequent work was done in a 4°C cold room or on ice in order to limit protein degradation. After centrifugation, the supernatant was loaded on a DEAE sepharose CL-6B column, an ion-exchange column, and eluted into a fraction collector using a linear phosphate buffer gradient. Once eluted, a Sodium Dodecyl Sulfate Polyacrylamide Gel Electrophoresis (SDS-PAGE) was run on the collected fractions and only those fractions with a high content of protein were kept. The desired fractions were concentrated and then run through a G-75 fine size exclusion column. Another SDS-PAGE was run on the samples and only fractions that contained no visible contaminants were kept. Following this, a hemin solution was mixed with the protein solution and the heme is naturally incorporated into the protein. As a final step to the purification, the protein was re-crystallized three times by dialyzing it with deionized water, suspended in deionized water and then flash frozen in liquid nitrogen for storage. All protein samples were kept at –80°C until use.

5.2.2 Sample Preparation

5.2.2.1 Preparation of CcP and CcP W191F for UVRRS

Protein samples were thawed on ice, pelleted by centrifugation and re-suspended in 100 mM pH 7 phosphate buffer with 150 mM Na_2S0_4 (BDH Inc., Toronto, ON). This was made by titrating 100 mM KH_2PO_4 (EM Scientific, Darmstadt, Germany) with 100 mM K_2HPO_4 (EM Scientific, Darmstadt, Germany). This protein solution was centrifuged again to remove any excess heme that might still be present. The concentration of the protein was determined using a Cary 6000 (Varian, Palo Alto, CA). CcP has an extinction coefficient of 119 $mM^{-1}cm^{-1}$ at 408 nm. Protein concentrations

were adjusted in pH 7 phosphate buffer to 0.4 mM. A solution of 0.4 mM hydrogen peroxide (Fisher Scientific, Fair Lawn, NJ) was made up using the same buffer from a 30% Stock and checked using a extinction coefficient of $39.4M^{-1}cm^{-1}$. Immediately before each Raman experiment, 100 µL of protein was added to either 100 µL of buffer or 100 µL of 0.4 mM hydrogen peroxide solution. As a result, every solution was 0.2 mM protein, and 150 mM Na_2S0_4. Where applicable, the hydrogen peroxide concentration was 0.2 mM. The protein concentration needed for the Raman experiments was determined by using simulation software developed by Shane Greek[120] which determines the optimum concentration of samples based on photon scattering and sample self absorption. Hydrogen peroxide concentrations were chosen to be in the same stoichiometric amount at the enzyme hopefully limiting the formation of undesired non-radical species.

5.2.2.2 Preparation of Reduced CcP for UVRRS

Reduced CcP was prepared in a nitrogen filled glove box. 100 mM pH 7 phosphate buffer with 150 mM Na_2S0_4 was bubbled with argon to remove all traces of oxygen and an argon flow was placed overtop of the protein solution to remove oxygen before introduction into the glove box. A large excess of Sodium Dithionite (Sigma, St. louis, MO) was used to reduce the protein as prescribed by Wittenberg et al[121]. The sample was then washed in a concentrator with successive washes of buffer until Sodium Dithionite was not present in the UV/Vis data. The protein and the buffer were kept in sealed anoxic containers. Identical concentrations and solution preparation were used for reduced CcP as were previously described for CcP and CcP W191F. All spectra were taken under anaerobic conditions by using oxygen free buffer and a gas tight syringe to

load samples and by continuously flowing argon over samples during sample analysis. Hydrogen peroxide was added to form CcP with the iron in the +4 oxidation state but with no concomitant radical[122].

5.2.3 UVRRS of Protein Samples

All data was recorded with the liquid nitrogen cooled CCD array except the data taken from the reduced Cytochrome c Peroxidase, which was taken using the thermoelectrically cooled CCD camera. The maximum laser power that was available from the laser at 248.2 nm was approximately 65 mW but the laser power at the sample was kept constant at 20 mW for all investigations of the protein samples. The samples were mixed using a custom design spinning apparatus powered by a small motor which was able to achieve a sufficient degree of stirring. Spectra were taken at 10s intervals and no sample was exposed to a total of more then 60s of laser power.

5.2.4 Activity Assays

Activity assays of Cytochrome c Peroxidase were performed as prescribed by Sigma-Aldridge[123]. 2,2'-Azino-bis(3-Ethylbenzthiazoline-6-Sulfonic Acid) (ABTS) (Sigma, St. louis, MO), Hydrogen Peroxide (Fisher Scientific, Fair Lawn, NJ) and Cytochrome c Peroxidase were prepared to 10 mM ABTS, 3.0×10^{-4} mM CcP and 0.3% H_2O_2 all dissolved in 100 mM $K_iH_iPO_4$ pH 7.0 and standardized using the Cary 6000 (Varian, Palo Alto, CA). Protein samples were irradiated at 20mW at 248.2nm with stirring at 10s intervals. Kinetic data was also taken using kinetic software accompanied with the Cary 6000 (Varian, Palo Alto, CA).

5.2.5 Ultraviolet Visible Measurements

Ultraviolet/Visible Spectra used to aid resonance Raman measurements were recorded using a Cary 6000 (Varian Inc., Palo Alto, CA).

5.3 Results and Discussion

5.3.1 Selection of FO-UVRRS Excitation Wavelength

The UV/Vis spectrum of tryptophan radicals has been observed previously[124] but the spectral region amenable to FO-UVRRS was absent. For this reason, the UV/Vis spectrum of CcP and Compound I were taken in the region from 200nm to 300nm. The difference spectrum of Compound I and CcP was taken. The difference spectrum shows two distinct differences in this region with local maxima occuring at roughly 240nm and 205nm. With the assumption that these signals were due to radical species the excitation wavelength was selected with this in mind. No laser lines were available to excite the 205 nm absorption. 248.2 nm is a good choice for excitation wavelength because both tryptophan and tyrosine have reasonable excitation cross-sections at this wavelength[125] thus allowing simultaneous detection.

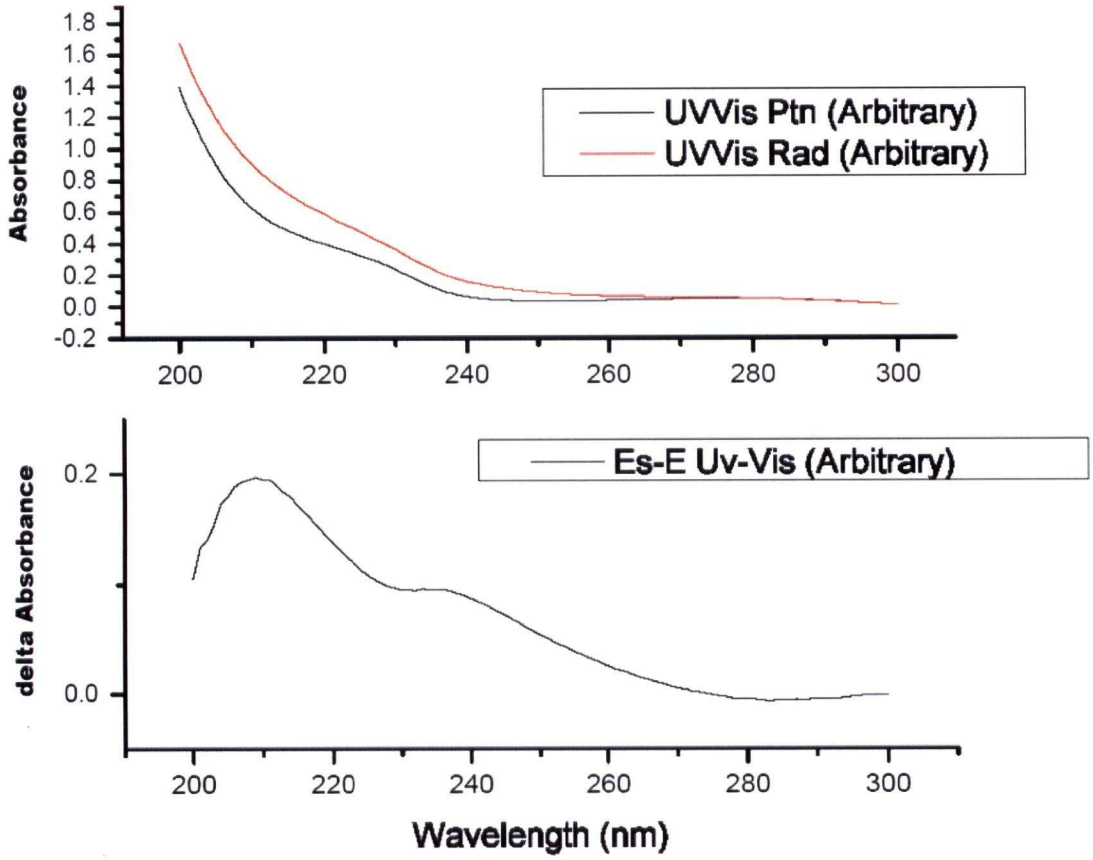

Figure 5.2: The upper plot is the UV/Vis spectrum of CcP and Compound I while the lower graph is the subtraction of the spectrum of CcP from that of Compound I.

5.3.2 UV/Vis of Proteins

The UV/Vis spectrum of CcP is generally regarded as a good indicator of enzyme quality since the Soret band is very sensitive to it's environment. The Soret band is also a good indicator of the oxidation state of the iron. The UV/Vis spectrum of prepared CcP, CcP W191F and reduced CcP were all taken and indicated that all the proteins conformed to previously acquired UV/Vis data.

5.3.3 Activity of CcP after UV Irradiation

Ultraviolet radiation can severely damage biological samples, if care is not taken, resulting in a partial or complete loss of protein function. As a result, activity assays were performed on CcP to ensure that data was only being acquired under conditions that allowed the protein to still be active. Figure 5.4 shows the evolution of ABTS radical versus time after the addition of hydrogen peroxide. From initial visual inspection it appears that there is no loss of enzyme activity. The slope of the linear portion of each curve was calculated and the activity of samples relative to the activity before irradiation was determined. The result is plotted in figure 5.4. By comparing the slopes of each irradiated sample of CcP one can compare the relative activities of each irradiated sample of CcP. Upon initial inspection of the slopes of these samples it seems that there is no significant activity loss. By plotting the relative activity of each sample versus time it is apparent that there is no significant loss of activity during the course of data collection due to ultraviolet light. As a result it can be inferred that the protein undergoes relatively little damage during irradiation of up to 50s of 248.2nm wavelength light at 20 mW.

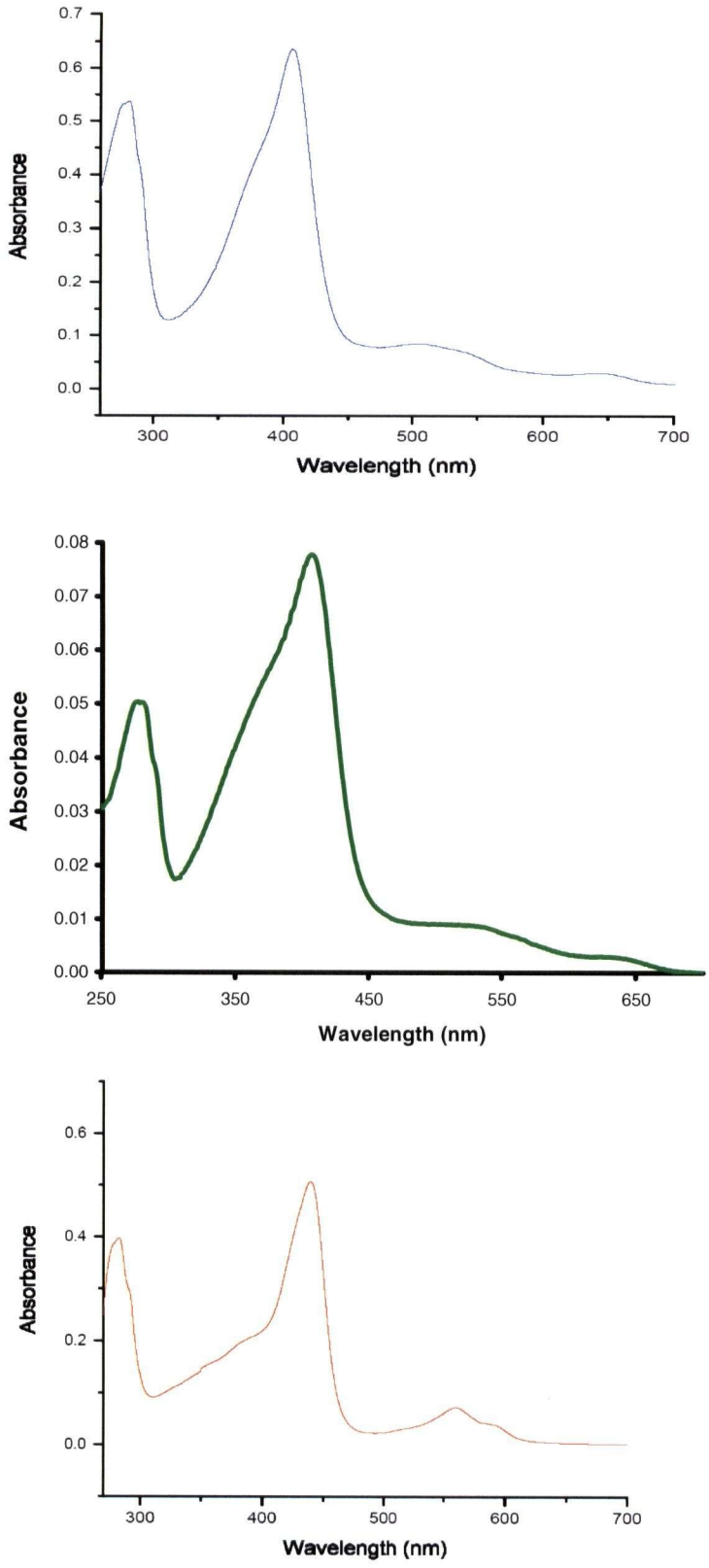

Figure 5.3: (Top) UV/Vis of CcP in 100mM KiPO4 buffer (Center) UV/Vis of CcP Trp191Phe in 100mM KiPO4 buffer (Bottom) UV/Vis of Reduced CcP.

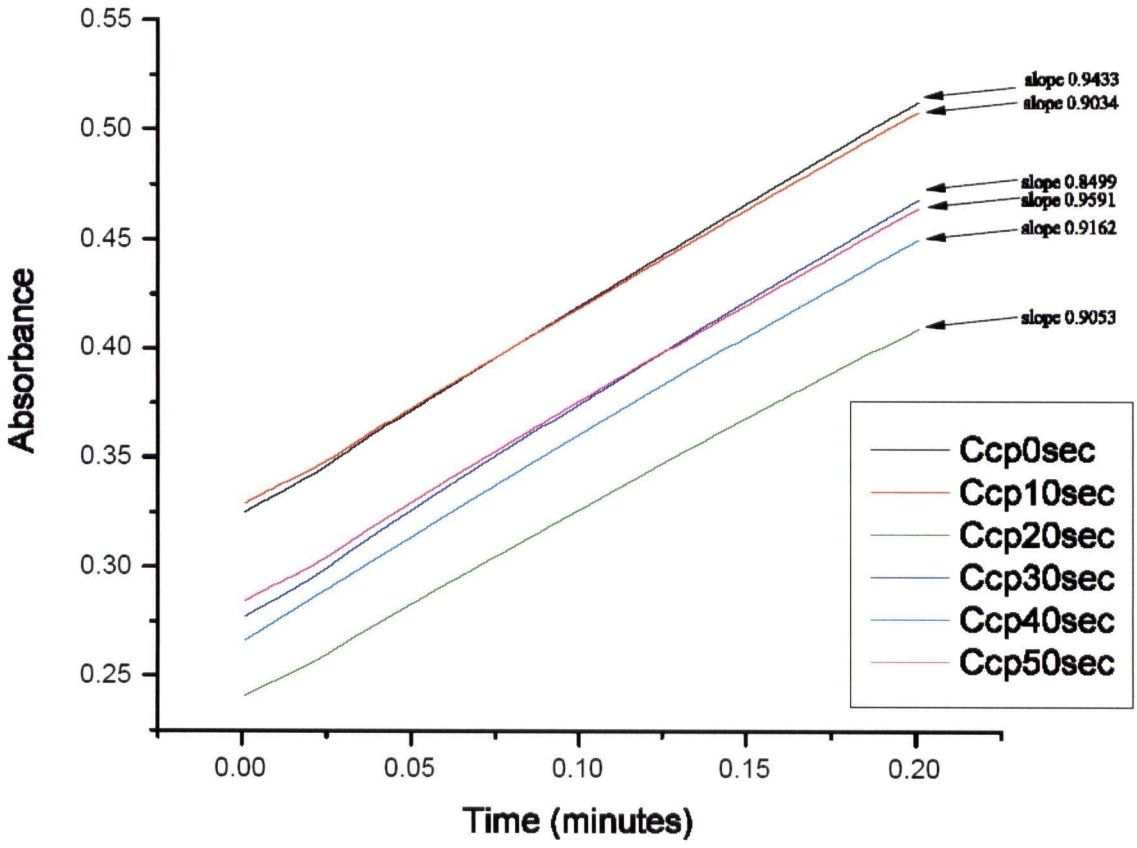

Figure 5.4: Each plot represents the reduction of ABTS versus time. Each assay was performed with CcP that had been exposed to UV light at 248.2 nm at 20 mW for 0 sec to 50 sec. All assays were performed with 10mM ABTS, $3.0x10^{-4}$ mM CcP and 0.3%H_2O_2 dissolved in 100 mM $K_iH_iPO_4$ pH 7.0.

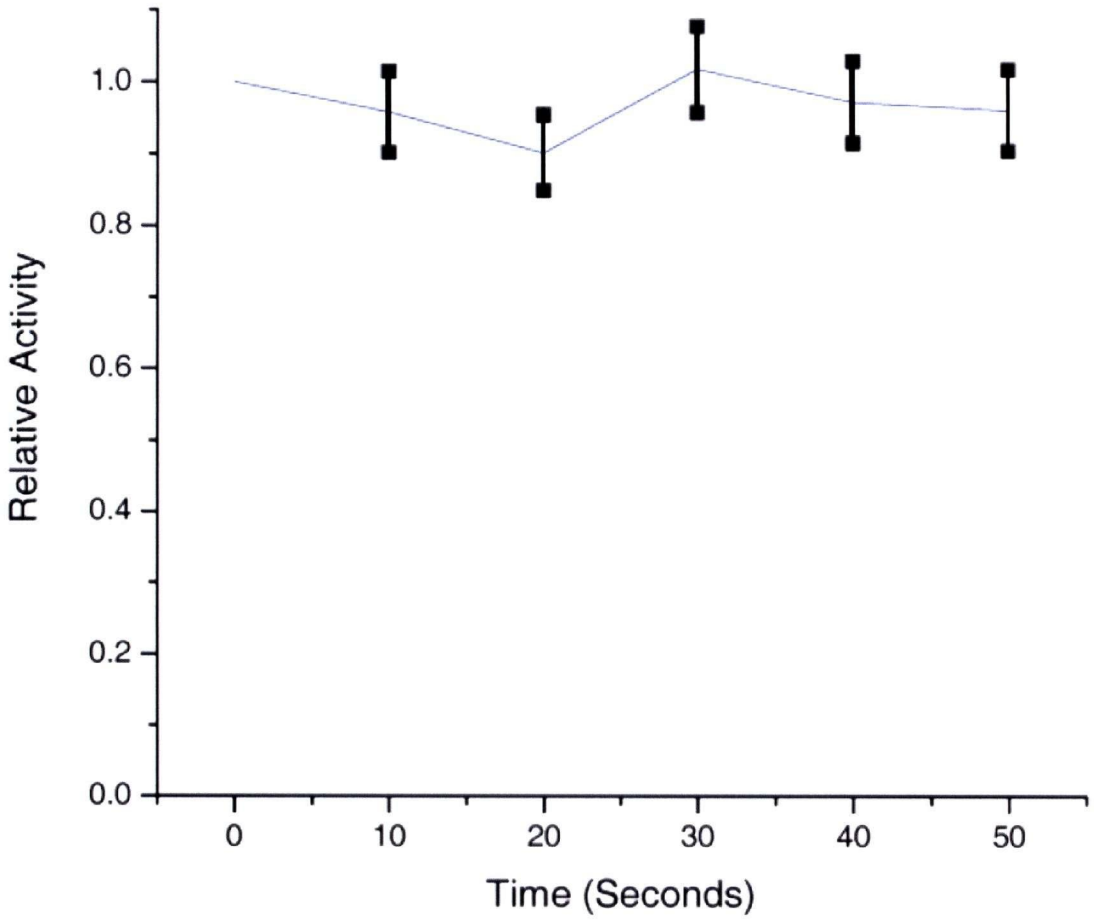

Figure 5.5: A plot of the activity of CcP irradiated at 248.2 nm relative to CcP that had not been irradiated.

5.3.4 FO-UVRR Spectra of CcP Proteins

The UVRR spectra of CcP, it's associated compound I, and the subtraction of CcP from compound I are shown in Figure 5.6 and the corresponding vibrational assignments of CcP are listed in Table 5.1. Sodium sulfate, 982 cm^{-1}, was used as a reference in order to perform the subtraction.

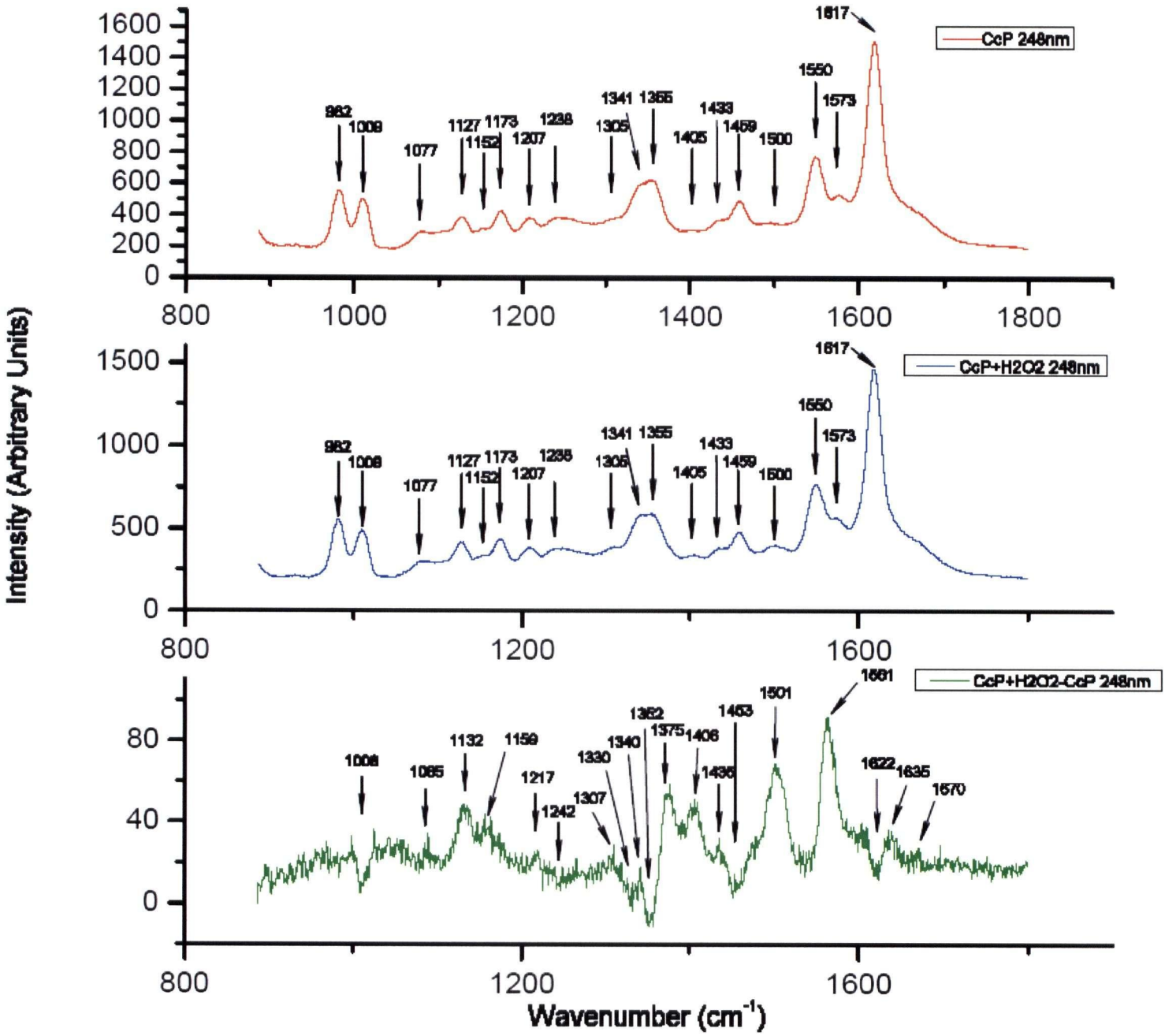

Figure 5.6: (Top) UVRRS spectrum of 0.2 mM CcP in 0.1 M $KHPO_4$ pH 7.0 buffer with 0.150 M Na_2S0_4 as an internal standard. Excitation wavelength of 248.2 nm at 20 mW and each sample irradiated for no longer than 50s but 240s averaging in total. (Middle) UVRRS of 0.2 mM CcP with 0.2 mM of H_2O_2 in 0.1 M KHPO4 pH 7.0 buffer with 0.150 M Na_2S0_4 as an internal standard. Excitation wavelength of 248.2 nm at 20 mW and each sample irradiated for no longer than 50s but 200s averaging in total. (Bottom) Difference spectrum of Top from Middle based on the Na_2SO_4 internal standard.

Trytophan Vibrational Mode	Experimentally Observed Values	Assignment
W1	1622	Φ8a;N1-C8v
W2	1573	Φ8b
W3	1550	C2-C3v
W4	1500	Φ19b
W5	1459	Φ19a
W6	1433	N1-C2-C3v;N1Hδ
W7	1355/1341	Fermi Resonance
W8	1305	C3-C9v;N1Hδ
W10	1238	C3-C10v;CHv
W13	1127	Φ9b
W16	1008	ΦC-Cv(Φ18b)

Table 5.1: The labeled vibrational modes of Tryptophan, the experimentally observed values and the appropriate vibrational assignment.

The difference spectrum of the radical contains a variety of prominent positive and negative peaks. This is expected with the presumption that we are creating radical species from the addition of H_2O_2 while at the same time removing the signal from the lost tryptophan or tyrosine. When investigating unknown systems using Raman spectroscopy, many studies use a model compound to compare with the Raman spectra. In this case, the identity of the radical species involved have been identified and verified previously *via* multiple other techniques and thus we can consider CcP to be a model compound of the radicals negating the need for such a protocol. With this in mind, we must consider that the observed spectrum is likely due to a mix of both a tryptophan and tyrosine radicals. In order to differentiate between a tryptophan radical signal and other changes in the protein the CcP W191F mutant was employed. As explained previously, the CcP W191F mutant retains all activity except that it's tryptophan radical is avoided and the radical is based on the heme instead. Although no studies have been conducted

with this mutant to investigate tyrosine radicals, it is likely that the protein still forms tyrosine radicals upon addition of hydrogen peroxide. Logically, any signals that are observed to significantly decrease in intensity should be due to the tryptophan cationic radical and any remaining signals should be due to either the heme or a tyrosine radical. The resulting spectra of CcP W191F, it's associated compound I and CcP W191F subtracted from compound I are shown in Figure 5.7. Sodium sulfate was used as reference for the subtraction.

Although the signals of the tryptophan radical can be isolated it would also be useful to determine if the source of the remaining signal originated from either tyrosine or heme. Since the most useful spectroscopic absorptions of heme occur in the visible region, no UVRRS studies of heme could be found in the literature. As a consequence, it is difficult to assess what contribution heme would have in the UVRR spectrum. Conveniently, it has been shown that CcP can be reduced to the iron (II) state and oxidized to the iron (IV) state without the formation of the cationic radical[122]. This means that any changes in the spectra due to changes in the heme can be monitored separately. The resulting spectra of CcP (II), CcP (IV) and CcP (II) subtracted from CcP (IV) are shown in Figure 5.8.

Upon inspection of the three difference spectra obtained in this study it is immediately obvious that they are all unique. Examination of the difference spectrum of CcP in the iron (II) state and CcP in the iron (IV) state reveals that a relatively small difference exists between the UVRR spectra of the two iron oxidation states. This indicates that none of the peaks observed in the difference between native CcP and it's associated compound I are likely to be due to changes in the heme or heme environment.

This also means that many of the signals observed in the native protein are either from the tryptophan radical or tyrosine radicals.

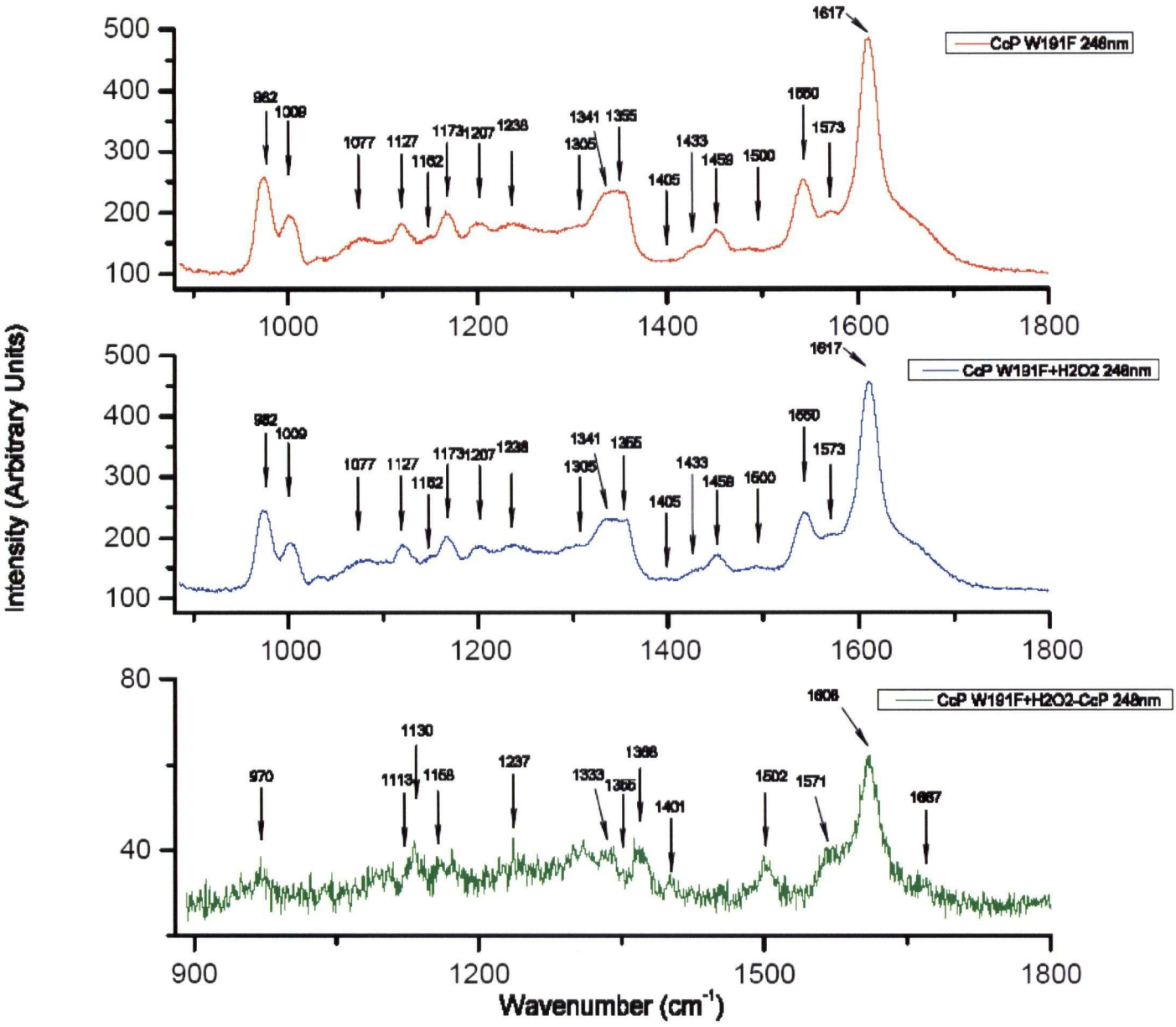

Figure 5.7: (Top) UVRRS spectrum of 0.2 mM CcP W191F in 0.1 M $KHPO_4$ pH 7.0 buffer with 0.150 M Na_2S0_4 as an internal standard. Excitation wavelength of 248.2 nm at 20 mW and each sample irradiated for no longer than 50s but 270s averaging in total. (Middle) UVRRS of 0.2 mM CcP W191F with 0.2 mM of H_2O_2 in 0.1 M KHPO4 pH 7.0 buffer with 0.150 M Na_2S0_4 as an internal standard. Excitation wavelength of 248.2 nm at 20 mW and each sample irradiated for no longer than 50s but 330s averaging in total. (Bottom) Difference spectrum of Top from Middle based on the Na_2SO_4 internal standard.

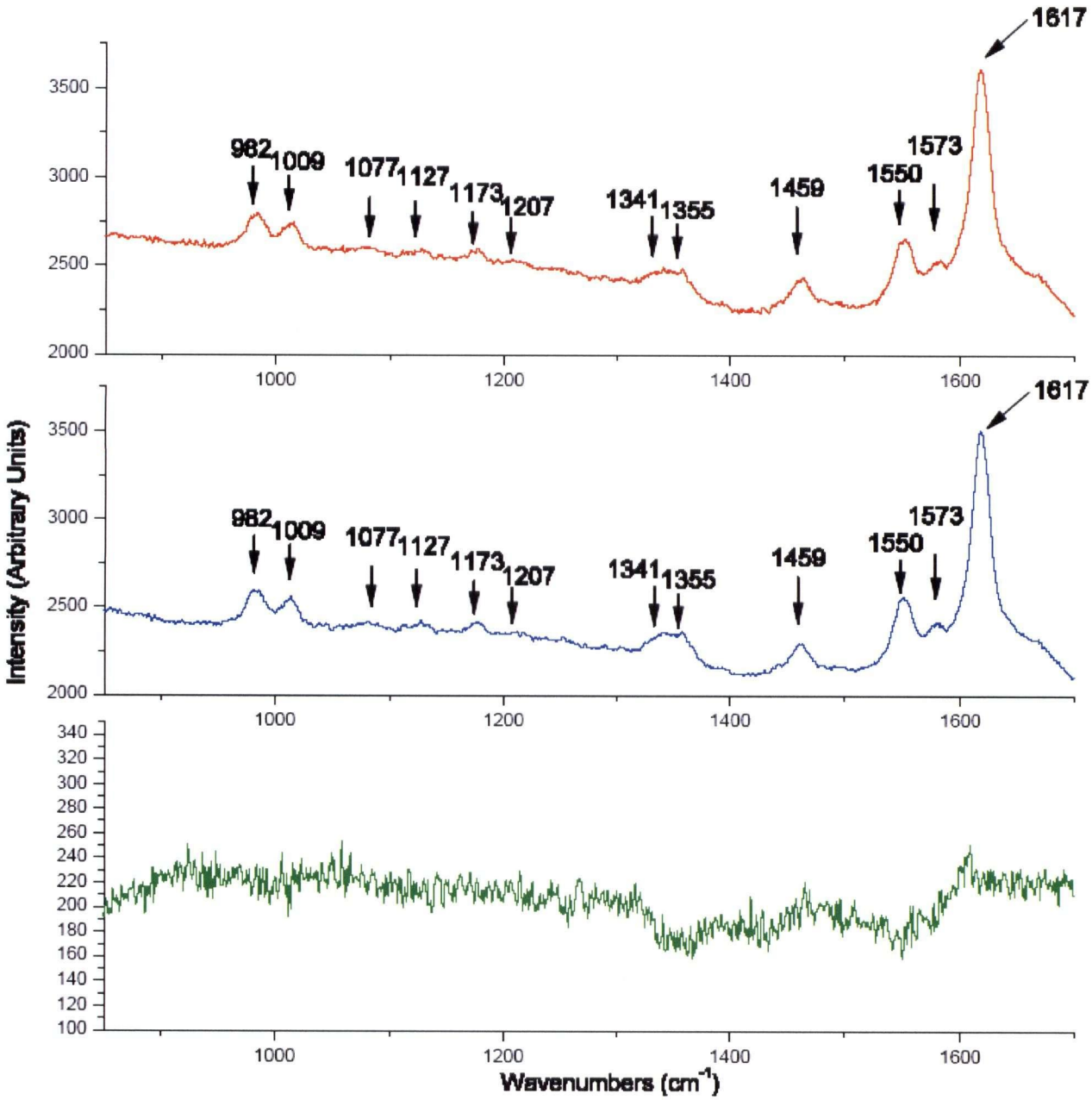

Figure 5.8: (Top) UVRRS spectrum of 0.2 mM Reduced CcP in 0.1 M $KHPO_4$ pH 7.0 buffer with 0.150 M Na_2S0_4 as an internal standard. Excitation wavelength of 248.2 nm at 20 mW and each sample irradiated for no longer than 50s but 240s averaging in total. (Middle) UVRRS of 0.2 mM Reduced CcP with 0.2 mM of H_2O_2 in 0.1 M KHPO4 pH 7.0 buffer with 0.150 M Na_2S0_4 as an internal standard. Excitation wavelength of 248.2 nm at 20 mW and each sample irradiated for no longer than 50s but 180s averaging in total. (Bottom) Difference spectrum of Top from Middle based on the Na_2SO_4 internal standard.

Having eliminated heme from the discussion, it is now pertinent to examine the remaining two difference spectra to attempt to differentiate the tryptophan signal from the tyrosine signal. On initial comparison, it is quite apparent that all of the peaks observed in the native protein spectrum have either disappeared or significantly reduced in intensity when going from the native protein subtraction to the mutant subtraction. An exception occurs at 1608 cm^{-1}, where a negative signal observed in the native difference spectrum is replaced by a positive peak in the mutant difference spectrum. The obvious question arises that if the signal observed in the native protein difference spectrum is a combination of two signals then why is a new peak observed? As it turns out, the negative signals observed in the native difference spectrum at 1008 cm^{-1}, 1352 cm^{-1} and 1622 cm^{-1} can be correlated with known tryptophan vibrations[119,126-130]. These negative signals are expected in the native difference spectrum since tryptophan 191 is being changed into a cationic radical and hence we would expect negative signals at know tryptophan vibrations and new positive signals from the radical. It is likely that the negative signal observed from the loss of a tryptophan at 1622 cm^{-1} is dominant over the new tyrosine radical signal seen at 1608 cm^{-1} and combine arithmetically leaving a negative signal. Once this negative signal is removed in the mutant difference spectrum, the signal at 1608cm^{-1} is observed. This signal is quite intense and so it is also possible that once Trp 191 is eliminated, a higher portion of the H_2O_2 that was previously used to form Tryptophan radicals is now used to form Tyrosine radicals.

Upon further examination of this data we also expect to see negative signals from any lost tyrosines but strong negative signals are not observed in the difference spectrum of CcP W191F and it's associated compound I while the signal at 1608 cm^{-1} is relatively intense. This observation can be explained by the combination a few contributing factors.

First of all, it must be pointed out that although tyrosine can be observed at 248.2nm, this wavelength is not ideal for tyrosine examination and the enhancement cross sections for tyrosine are relatively weak compared with other wavelengths[126,128,130]. As seen in the native protein spectra, tyrosine signals are not nearly as intense as tryptophan signals since they not as resonant at this frequency. Since there happen to be 14 tyrosines in CcP and the tyrosine signal is weak to begin with, the $1/14^{th}$ reduction in signal due to a missing tyrosine may be lost in the noise. If this is the case, then why is a relatively large positive signal observed in the mutant difference spectra? It is likely that the tyrosine radical has a larger excitation cross-section than tyrosine itself.

Calculations of the vibrational frequencies of both tryptophan and tyrosine radicals have been published in the literature[119,131] and it is useful to compare our values to these studies. Bunte *et al.*[119] calculated the Raman spectra of 3-methylindole and it's associated neutral and cationic forms. When comparing 3-methylindole calculations to experimentally observed values of tryptophan, it is immediately obvious that reasonably large discrepancies exist between the two sets of data. In order to aid in the comparison of collected data with calculated values, the calculated shift of each peak of 3-methylindole upon transformation to the cationic radical species was determined and these calculated shifts were applied to the experimentally observed tryptophan peaks. These new values should correspond more closely with the experimental values. With these values in hand, each peak on the CcP difference spectrum was matched with the closest matching peak of the calculated values.

Experimentally Observed Peaks (cm^{-1})	3-Methylindole Calculated Peaks (cm^{-1})	Cation Radical Calculated Peaks (cm^{-1})	Cation Calc. Minus 3-Methylindole Calc. (Negative is a downshift) (cm^{-1})	Change Applied to Experimental peaks (cm^{-1})	Resorted Descending (cm^{-1})	Possible Matching Peaks in Radical Subtraction (cm^{-1})
1622	1616	1636	20	1642	1642	1670
1573	1658	1595	-63	1510	1533	1561
1550	1594	1256	-338	1212	1510	1501
1500	1485	1518	33	1533	1434	1435
1459	1526	1501	-25	1434	1433	1435 or 1406
1433	1446	1446	0	1433	1366	1375
1355	1366	1377	11	1366	1317	1340
1341	1322	No Doublet		----	----	----
1305	1372	1374	2	1307	1307	1307
1238	1245	1324	79	1317	1212	1217
1127	1150	1124	-26	1101	1101	1085
1009	1034	1031	-3	1006	1006	neg peak at 1008

Table 5.2: Summary of calculated values used in determining the peaks correlated with the calculated 3-Methylindole Peaks.

The observed peak position was plotted versus the calculated peak position and the result is shown in Figure 5.9. The relationship between the two data sets is linear with a correlation coefficient of 0.99 indicating that there is very good correlation between the two data sets. This supports the previously made assumption that the observed signal is due to a tryptophan radical.

If the CcP W191F difference spectrum is compared with the CcP difference spectrum, it can be seen that the peaks at 970cm^{-1} and 1608cm^{-1} are probably new features and the peak at 1571cm^{-1} could also be new. Qin et al.[131] calculated the theoretical peaks for tyrosine radicals and these peaks are compared with the peaks found in this study in Table 5.3. The previous study investigating Tyrosine radicals involved irradiating samples with successively higher photon fluxes until a measurable difference signal was observed. Although signal was observed, there was never any attempt made to characterize these transient species by any other means. For this reason, it seems reasonable to conclude that the reason that the experimental signals observed in this study are different than those previously reported could be because different methods were used to create radicals and consequently it is possible

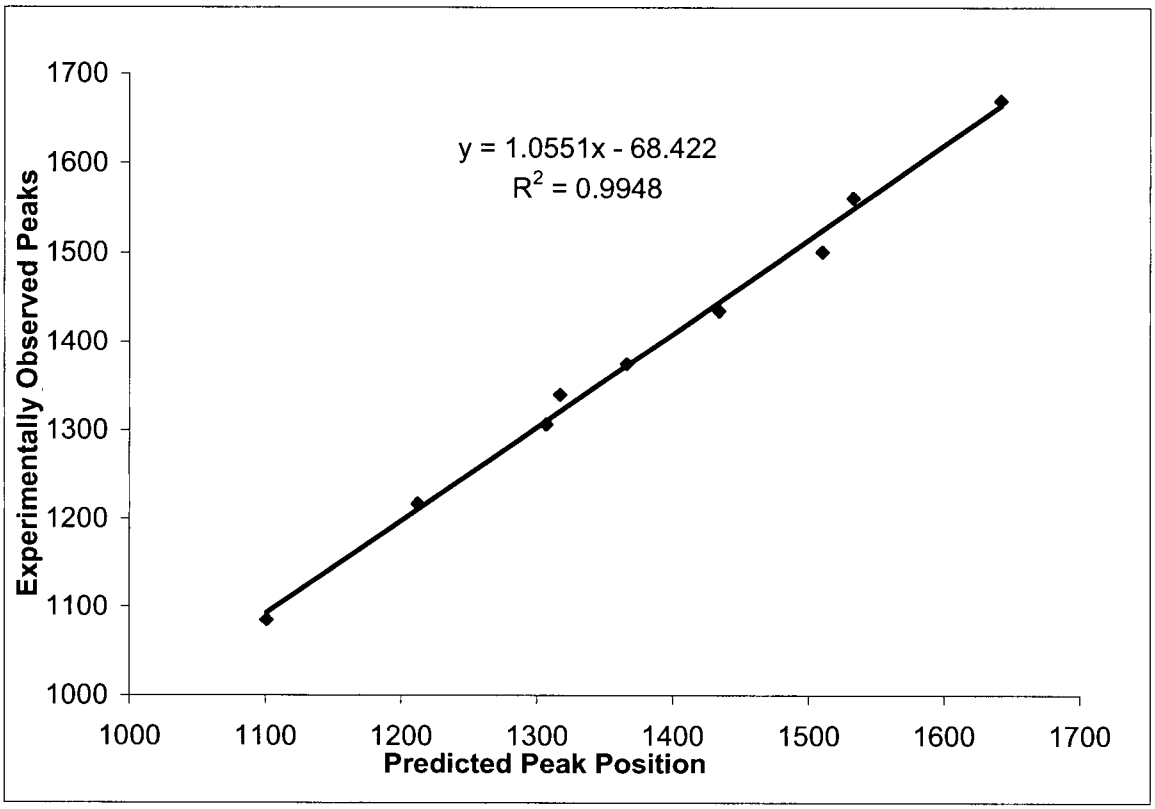

Figure 5.9: The predicted peak position of Tryptophan radical peaks was plotted versus the experimentally observed peaks and a linear regression was performed on the data.

Predicted (cm^{-1})	Experimentally Observed (cm^{-1})	Previously Observed Peaks (cm^{-1})
1620	1608	1565
1564	1571	1510
1418	-----	1402
1139	-----	1160
970	970	975

Table 5.3: Predicted, experimentally observed and previously observed peaks of Tyrosine radical species.

that the data represents two different species. With this in mind, if we compare the experimentally observed values in this study to those calculated there seems to be a reasonable amount of agreement between the values. The obvious question that arises is why two of the calculated peaks do not correlate to any other peaks in this experiment? It is possible that the missing peaks are masked by noise in this experiment. Achieving a higher signal to noise ratio that would have verified this assertion but would have required integrating for a much longer period. The amount of protein needed and the prohibitive amount of time required to ameliorate the signal negated this approach.

5.4 Conclusions and Future Directions

From the data collected in these experiments it seems quite apparent that the cationic tryptophan radical created in CcP with the addition of H_2O_2 was observed using UVRRS. Additional evidence also points to the observation of the tyrosine radicals that are formed concomitantly with the tryptophan radical and it has been shown that precludes any of the signal being due to the oxidation state of the Heme group in the molecule.

This study could be important for further investigations of other protein species since it is known that tryptophan and tyrosine are known sites of transient radical formation in the mechanism of action of a variety of proteins. Future development of our probes for use in a pulse-probe or stop-flow geometry could be very useful in the elucidation of the mechanism of action of differing protein systems.

Chapter 6

Development of a Raman Microscope Coupled Surface Plasmon Resonance Imaging Apparatus for Use in DNA Microarrays

6.1 Motivation

The development of DNA microarrays has been very important in the field of genomics. As previously explained in Section 3.3, one of the issues of "conventional" microarrays is that due to the use of fluorescent probes the quantitative information provided by these arrays is not as accurate as scientists would like in order for unambiguous conclusions to be made. The development of SPR imaging of DNA microarrays may be able to overcome these issues[68-74]. One drawback to both approaches is that they do not provide structural information about the bound molecules, information that could be useful for DNA researchers. Raman spectroscopy would be the perfect tool for such a structural analysis information acquired using Raman spectroscopy could provide valuable information about the interactions between the DNA probes and the molecules on the surface of microarrays. Since Gold is used in SPR microarrays and SERS can use gold as a substrate, the potential for signal amplification using SERS for DNA analysis is a possibility. The phenomenon of SERS, as described previously, offers the potential for ultrasensitive detection, analysis and identification of molecules. Although the mechanism of SERS enhancement is not completely understood, it is accepted that a large majority of the enhancement is due to localized surface plasmon resonances on fractal surfaces of noble metals. The difficulty with combining SERS and SPR lies in the fact that the fractal surfaces used in SERS are not compatible with current SPR technology. However, the use of flat surfaces for SERS have been theorized and

investigated which could allow a fusion of SPR and SERS technologies[132-134]. In fact, a weak enhancement of Raman scattered light on the order of 1 order of magnitude has been observed by using a flat SERS substrate. The combination of SPR and Raman for the use of DNA microarrays has not been previously studied and it was for this reason that research into this idea was conducted. .

6.2 Materials and Methods

6.2.1 Instrument Design

SPR microarray imaging devices have been described previously[135-141]. The essential components of these devices are a collimated light source, a prism for coupling the light to the gold surface, an interchangeable gold surface, a method for changing the incident light angle on the surface of the metal, and an imaging detector. Although the design of our apparatus was intended to conform quite closely with previously published designs, there were a few unique constraints to consider. First and foremost, the device had to be able to interface with the Renishaw 1000B Raman Microscope. Second, many SPR devices employ expensive step motors for angle adjustment of the incident beam on the gold surface but due to the inherent expense, these devices they were unavailable and alternative mechanisms for the operation and functioning of the apparatus had to be conceived

The instrument used in this study was designed to be relatively simple to construct and operate. Polarized laser light at a wavelength of 785 nm from a laser diode (Sanyo DL4140-001, Thorlabs, NJ) emitted in a wedge shape, was aligned so that the light was p-polarized relative to the gold surface. The diode laser was powered by a laser diode driver (Model 501 Laser Diode Driver, Newport Corporation, Irvine, CA). The

light passed through a bi-convex lens (Melles Griot) and was collimated. The lens position was adjusted back and forth to achieve optimal collimation. The collimated light passed into a right angle prism followed by a layer of index matching fluid (Norland Inc., NJ) and finally, through a BK-7 slide (Technical Glass Products, OH) and impinged onto the surface of the slide which had been coated with 3nm of Chromium and 50nm

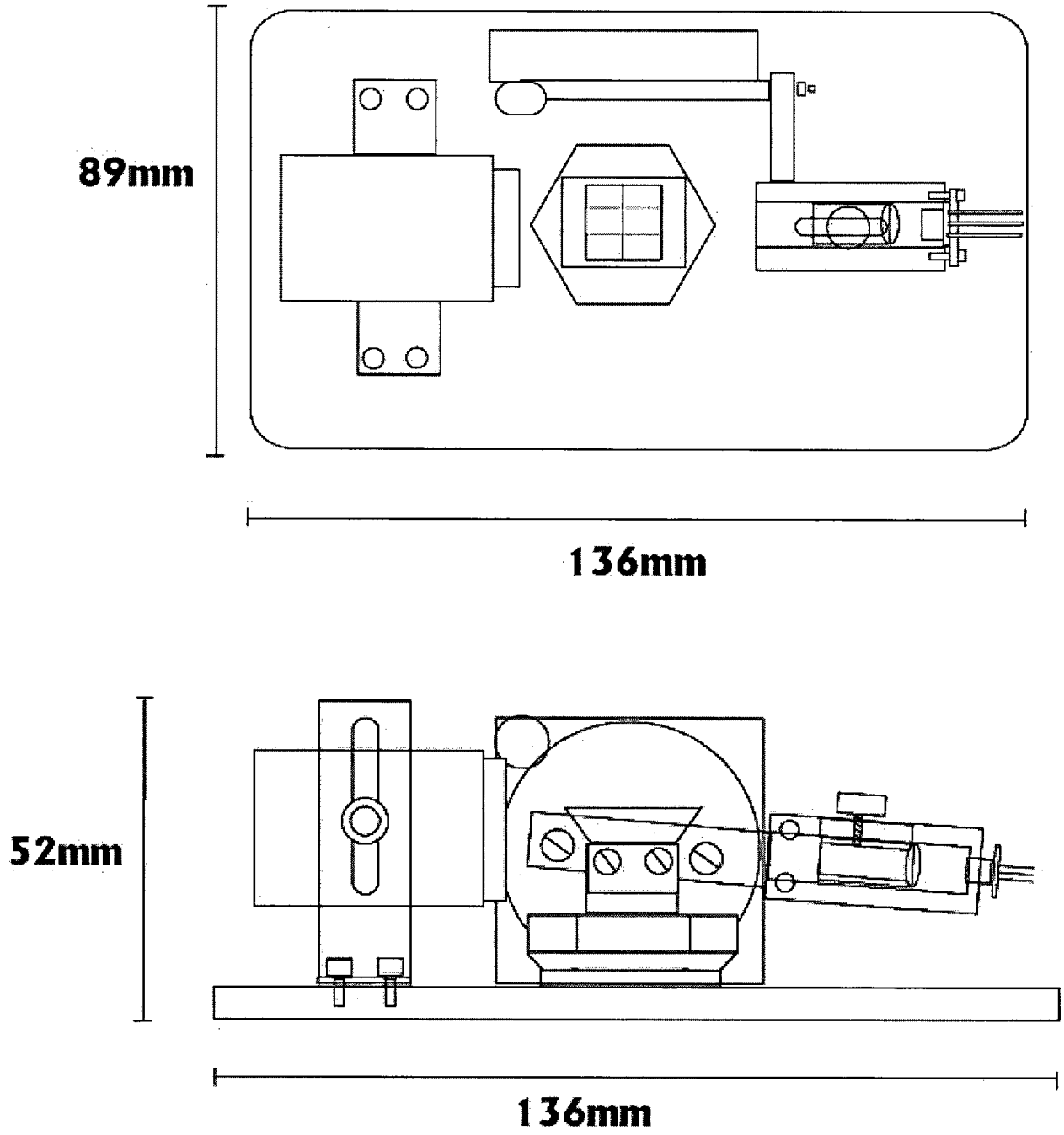

Figure 6.1: (Top) Top view of the SPR imaging device. (Bottom) Side view of SPR imaging device.

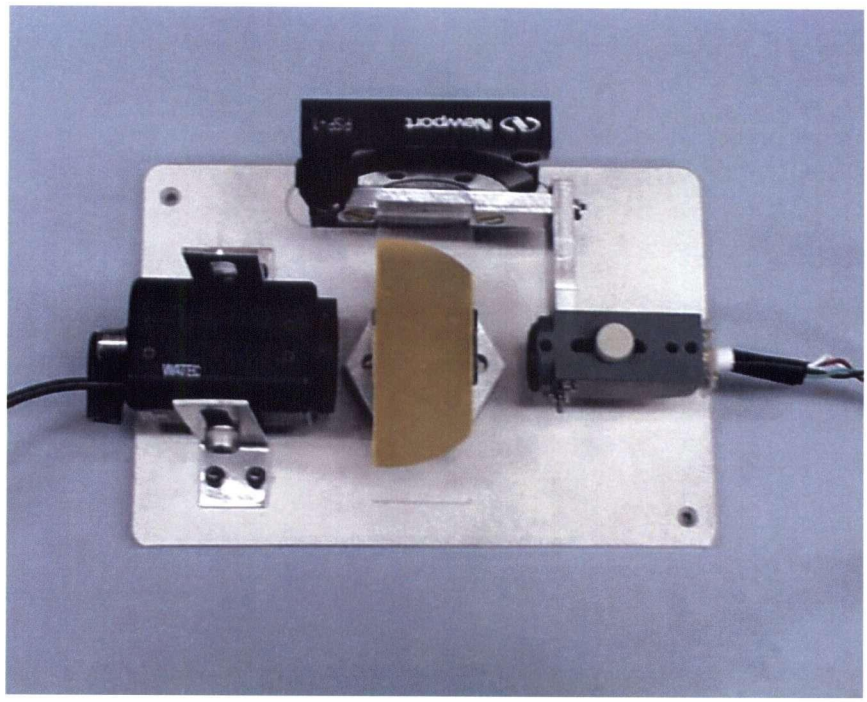

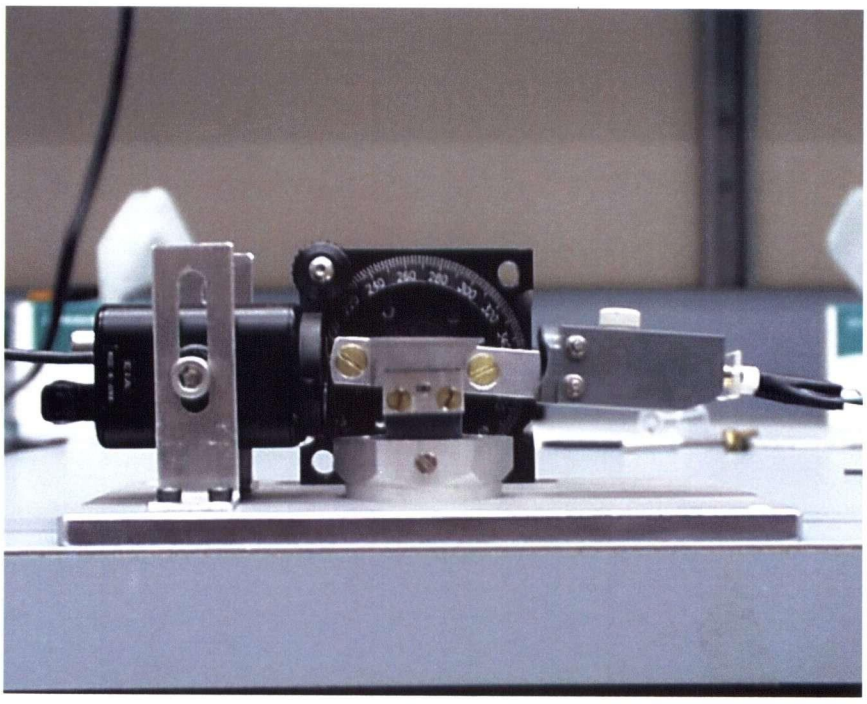

Figure 6.2: (Top) Top view photograph of completed SPR imager. (Bottom) Side view photograph of the completed SPR imager

of Gold. The gold and chromium were vapor deposited using a vacuum deposition chamber. The sample to be examined was placed on the gold surface in the region of laser illumination. The reflected light from the surface passed back through the slide, the index matching fluid, the prism and finally impinged on a low cost CCD camera (WAT-902, Watec, Japan). Angle adjustment of the incident light was achieved using a rotating mount (RSP-1, Newport Corporation, Irvine, CA) which gave accuracy of up to 0.5° and the prism height was also crudely adjustable. The base of the device was designed to fit into the slot of a removable inset of the Renishaw 1000B instrument. Any other components of the instrument were constructed by the UBC Chemistry Machine Shop. When the SPR imaging device was operated with the Raman microscope it was inserted into the removable inset of the translational stage and the two devices were operated independently.

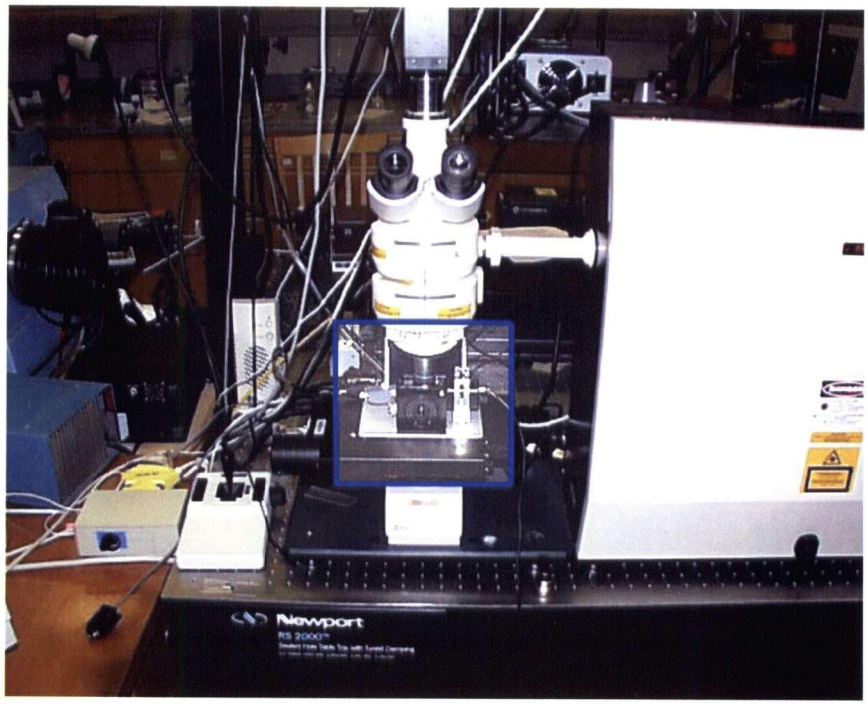

Figure 6.3: Highlighted view of the SPR device mounted in the Renishaw 1000B Raman microscope.

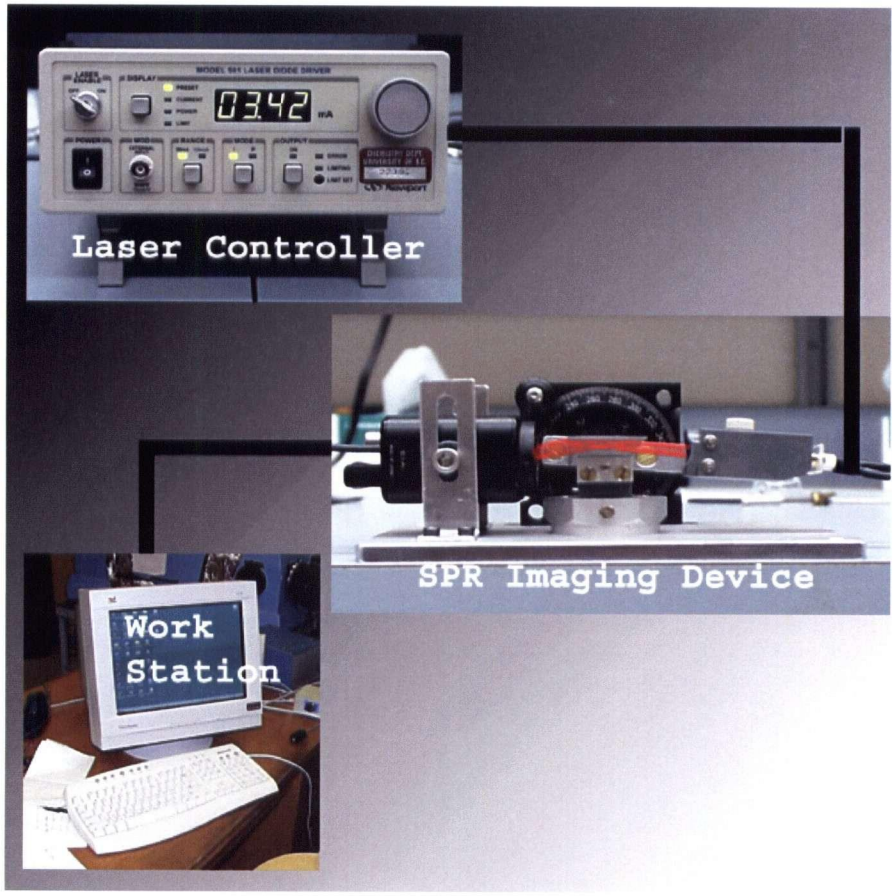

Figure 6.4: Flow diagram of SPR device control, beam path, and data collection.

6.2.2 Light Source Considerations

There were a few considerations when deciding which light source should be used for the SPR imaging system. Although Surface Plasmon Resonance occurs in the visible to infrared region of the electromagnetic spectrum, at higher frequencies the resonance subtends a broad range of angles while at lower frequencies the resonance becomes considerably sharper[141]. Figure 6.5 shows the theoretical resonance profile for water at 632.8 nm and at 785 nm to illustrate this point.

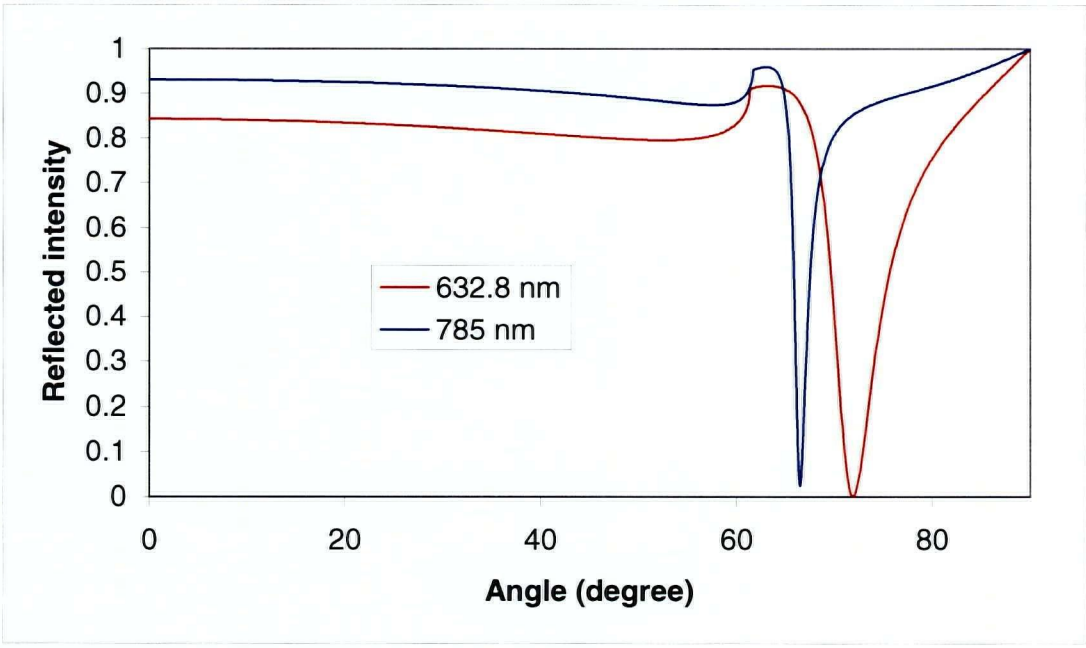

Figure 6.5: The theoretical resonance profile of water on a 50 nm gold surface bound to a BK-7 glass surface at 632.8 nm and 785 nm. The resonance of the 632.8 nm excitation subtends a much larger range of angles than the 785 nm resonance.

The advantage of having a sharp resonance angle is that it provides better resolution between different indices of refraction at the surface of the gold. In the end, two laser diodes were purchased. The first laser diode, which emitted light at 632.8 nm, was chosen because of the broad resonance characteristic of this wavelength since it would be helpful in the early instrument development stages. This property was useful because it permitted easy location of the resonance angle and thus facilitated instrument alignment. The second diode, at 785 nm, was chosen because the sharp resonance would improve the resolution of the instrument. This wavelength was also chosen to match the Ti:Sapphire laser frequency so that surface enhancement from SPR could be possible. This second light source was used for the day-to-day operation of the instrument. The power source used for the laser diodes was a laser diode driver (Model 501 Laser Diode Driver, Newport Corporation, Irvine, CA) which offered stable electrical currents ranging from 0 to 100 mA. It was important to employ a stable power source since laser diodes are susceptible to mode hopping. Since the absolute intensity of the reflected laser light is being monitored, if an unstable light source was used, mode hopping would seriously hamper the operation of the instrument.

6.2.3 Operating Software

The instrument was run on a 1 GHz Pentium III computer. Images were 'grabbed' from the CCD camera using GrabIt (AIMS Lab Inc).

6.2.4 Analysis Software

Two different tools were used for analysis of the data collected from the SPR imaging device. Fresnel calculations were performed to determine the theoretical angular profile of the surface plasmon resonance using a web based program offered by Dr. R. Corn[142]. Further analysis was performed using NIH Image v. 1.6.3 (Freeware). This software allowed cross-sectional intensities, three dimensional mapping, as well as background subtraction to be performed on collected images. All data collection and analysis of Raman spectra is the same as previously described.

6.3 Evaluation of SPR Imaging Device Operation

Although the SPR device was based on previously proven designs the operation of the home built instrument had to be evaluated to ensure correct operation. The initial testing of the instrument was performed with deionized water and 0.4 M and 1 M solutions of NaCl (Sigma). A background image of the blank slide was taken and then 2mm drops of these solutions were placed on the surface of the gold-coated slide. The device was tuned to the minimum reflectance of the water solutions and the resulting background subtracted image is shown in Figure 6.6. The images appear as ellipses since the collimated beam is incident on the surface of the gold at an angle but impinges normal to the surface of the camera. This enabled a greater surface area to be imaged, but if desired, the images can be corrected to account for this effect. Interference patterns are observed and this is due to the coherence of the laser light impinging on an uneven surface. Using an Abbe refractometer the refractive index of water was measured and found to be 1.33, and the refractive indices of the 0.4 M and 1.0 M salt solutions were

measured and found to be 1.3375 and 1.3422 respectively. With this information it was possible to calculate the reflected intensity *vs.* angle of each solution using Fresnel calculations.

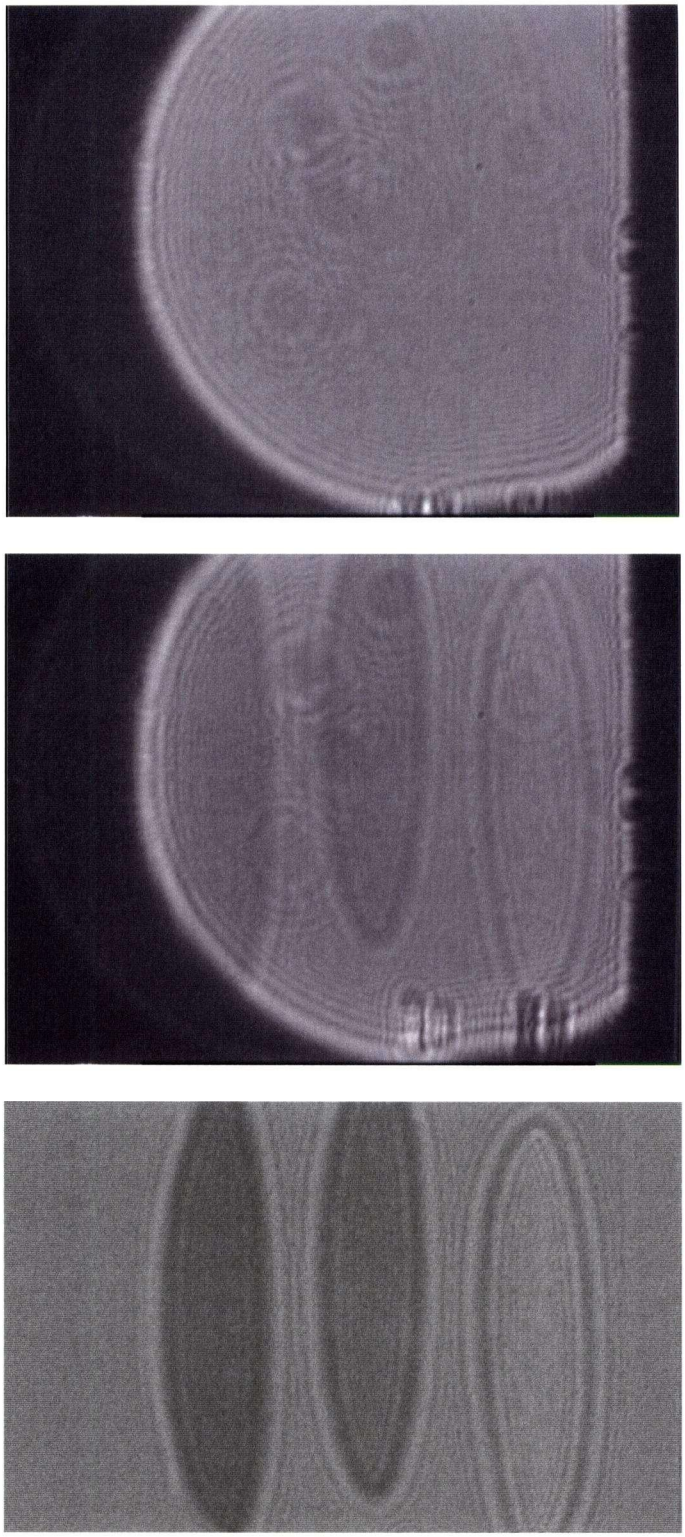

Figure 6.6: (Top) Background image of the reflected beam. (Middle) Raw image of drops on the gold surface of the custom built SPR imaging surface. The drops from left to right are deionized water, 0.4M NaCl and 1.0M NaCl. (Bottom) The background subtracted image of the drops.

The minimum reflectance of water was calculated to occur at 66.5° from the normal of the surface and this was also observed experimentally. These calculations also highlight that the instrument should be able to distinguish between the 3 solutions since the minimum reflectance of the curves do not overlap which is shown below.

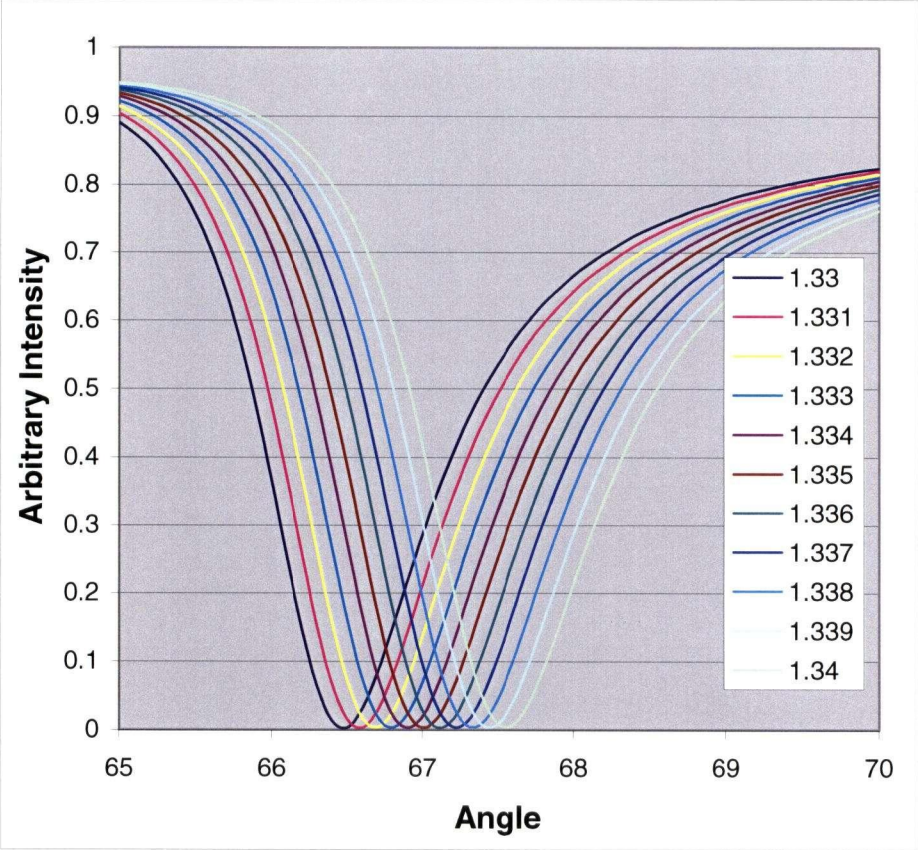

Figure 6.7: Calculated reflected intensity *vs.* angle of solutions of different refractive indices varying from 1.33 to 1.34.

NIH Image was used to plot the 3 dimensional intensity of the image as well the cross section through the image. It is immediately obvious that the reflected intensities of the 3 drops are different. From the image it is discernable that the water is in full resonance while the drop of 1 M NaCl is barely in resonance. From this data, we can say, with

confidence, that the instrument is capable of measuring differences of index of refraction on the order of $5x10^{-3}$. There are a few explanations as to the inferior signal to noise characteristics of the instrument. First of all, the CCD being employed for the imaging in this device is not intended to be used as an analytical instrument and as a result it's noise characteristics are not ideal for analytical instrumentation. An analytical CCD was available for use but extensive modification of the existing setup and modifications to the microscope would have been necessary. Secondly, the interference patterns add noise. Although care was taken with the optical setup there could still be room for improvement in future designs which might help eliminate this problem.

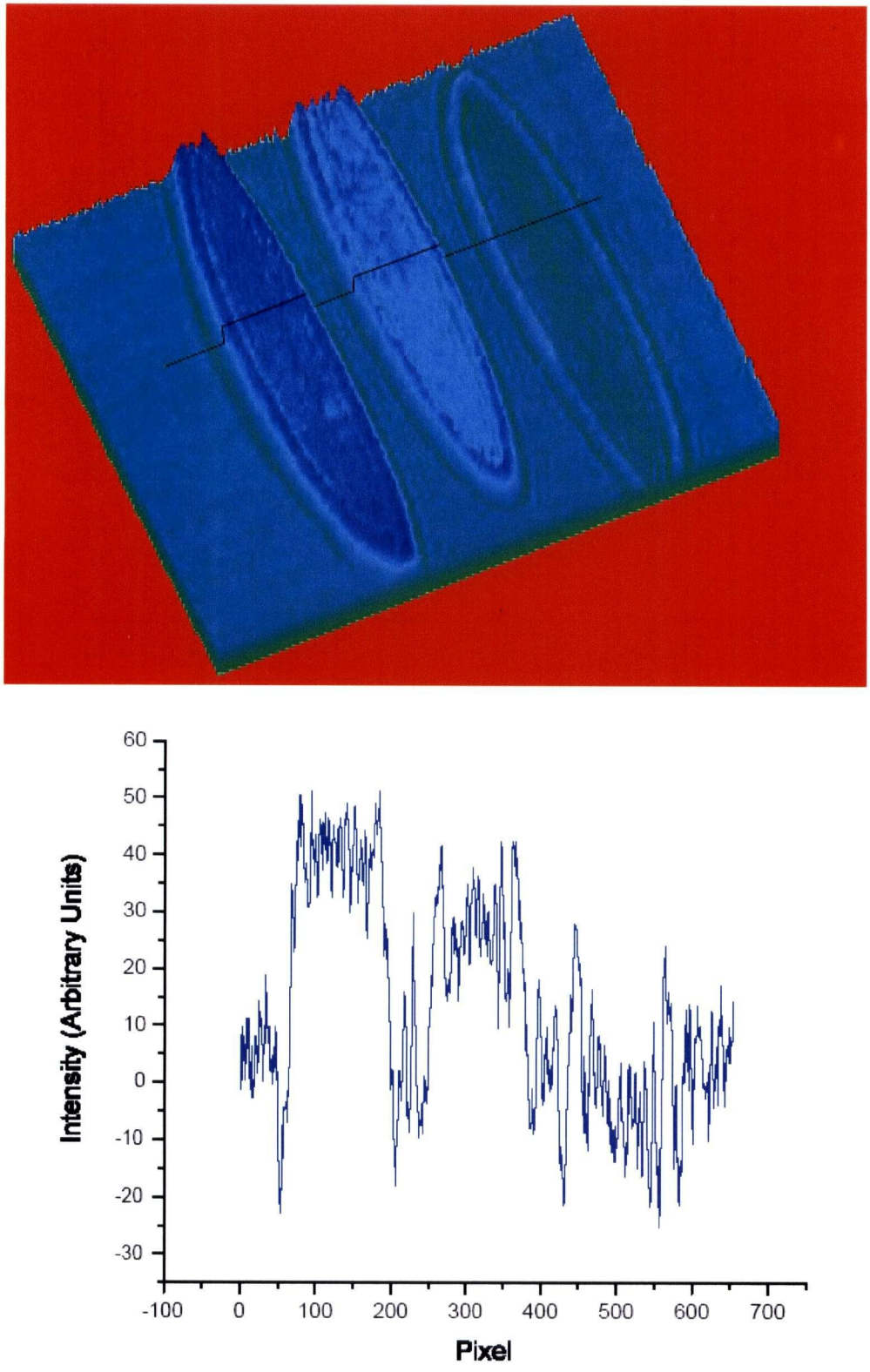

Figure 6.8:(Top) 3 dimensional cross section of the SPR image of the 3 droplets on the surface of the SPR imager. (Bottom) The numerical cross section of the black line drawn shown on the 3 dimensional cross section.

6.4 Evaluation of Raman Microscope Coupled Surface Plasmon Resonance Imaging Apparatus

After evaluating the performance of the SPR imaging device it was tested to see if any signal enhancement could be observed when performing Raman Spectroscopy on a sample.

6.4.1 Experimental

The SPR imaging device was operated as detailed in section 6.2 and was mounted into the removable inset of the Raman Microscope. Since DNA on microarrays was the desired analyte, DNA was chosen as the test substrate for this experiment. A 2 μl spot of Salmon Sperm DNA (Life Technologies Inc. (GIBCO BRL), Rockville, MD) with a concentration of 1mg/ml suspended in 0.1 mol/L phosphate buffer was dropped on the surface of the gold slides and left to dry under a flow of dry nitrogen. The sample was placed in the imaging device with a drop of index matching fluid between the prism and the slide. The angle adjustment on the SPR imager was rotated until the image of the DNA spot was witnessed. This angle was found empirically to be 45°. Since the CCD camera on the SPR imaging device could only handle low incident powers, all images were taken with the diode being driven with 2 mA of current prior to laser irradiation but the diode laser current was turned up to 50 mA for acquisition of Raman spectra in the hopes of achieving the greatest possible enhancement. The intensity of the laser beams were too low to measure with the power meters available in the lab. The Ti:Sapphire laser

was tuned to 785 nm to match the laser diode output and the power at the sample was set to 30 mW. Spectra were each collected for 10 minutes with and without laser irradiation.

6.4.2 Results and Discussion

In Figure 6.8 the SPR imager was tuned to 45° and a film of DNA from an evaporated drop was created on the gold surface.

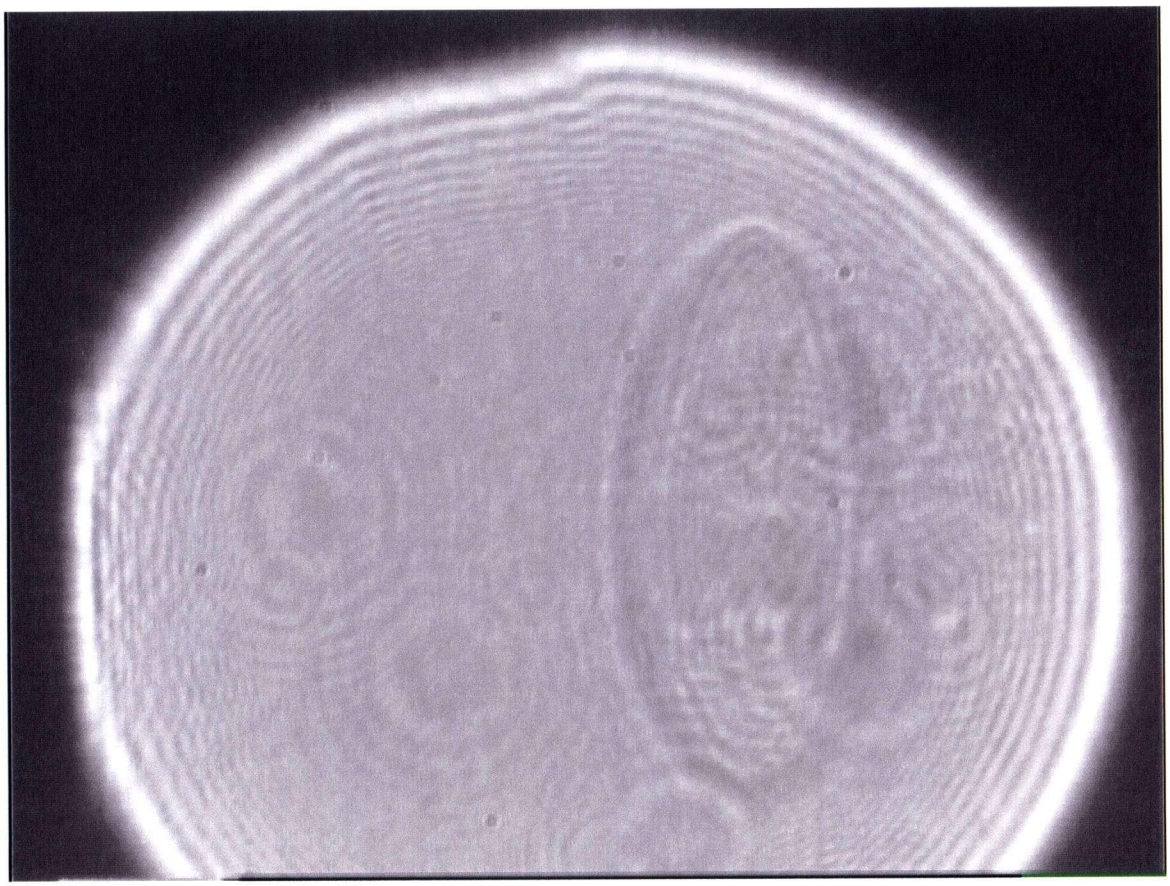

Figure 6.9: The SPR image of evaporated drop of DNA solution on the surface of the gold coated slide.

This is important since the absence of light reflecting from the surface indicates that a surface plasmon resonance is being excited on the surface of the gold slide in the area of the DNA film. After having achieved surface plasmon resonance of the substrate it is possible to further investigate whether any significant Raman enhancement occurs. A spectrum of a bulk sample of DNA was used to collect a higher intensity spectrum to compare with the thinner layers used on the SPR imager's gold surface. The features observed in the spectrum are well known DNA vibrations and they're assignments are listed in Table 6.1 [143-150]

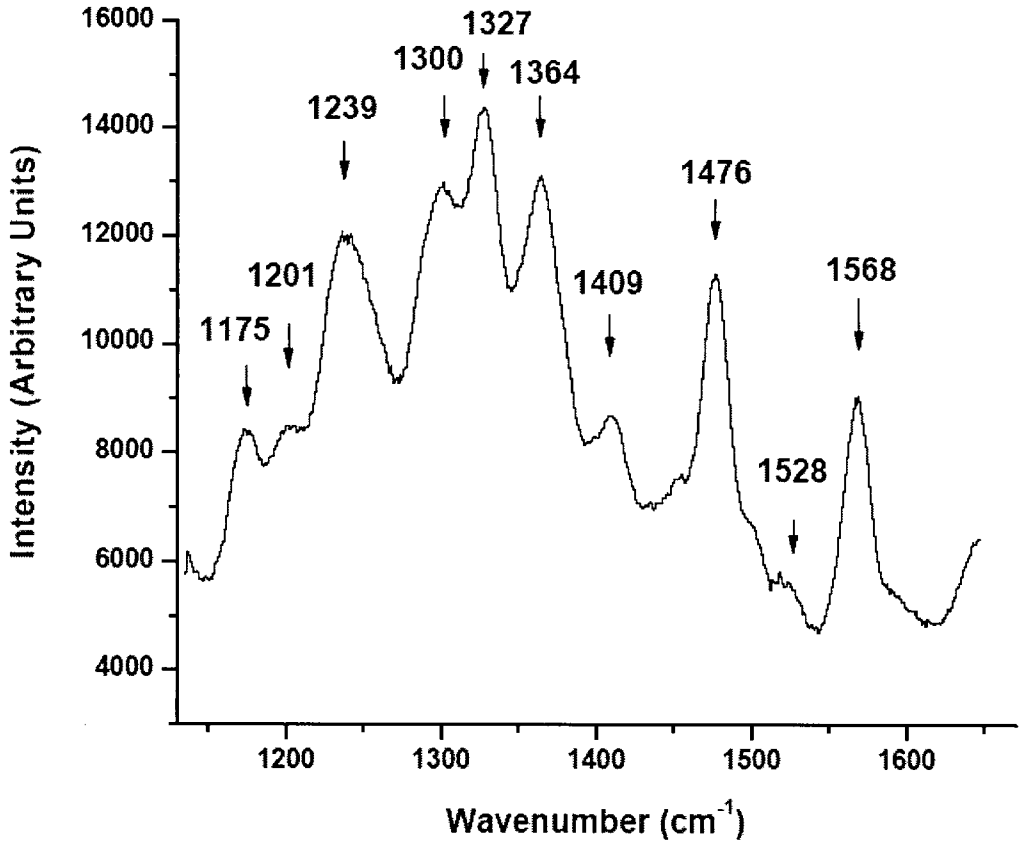

Figure 6.10: The Raman Spectrum of a bulk sample of Salmon Sperm DNA taken at 30 mW for 10 minutes.

Wavenumbers (cm-1)	Assignment
1175	dA, N7C8; C1N2 s; C6NH b
1201	dT, C5-CH3 s + ring
1239	dT, C5-CH3; ring s, dC
1300	dA,dT
1327	dT,dC
1364	dT, ring+C6-H ip bend, dG
1409	dA, dG
1476	deoxyribose
1528	dC, -N3C4, - N1C2
1568	dA, dG

Table 6.1: Vibrational assignments of the observed bands in the spectrum of Salmon Sperm DNA.[143-150]

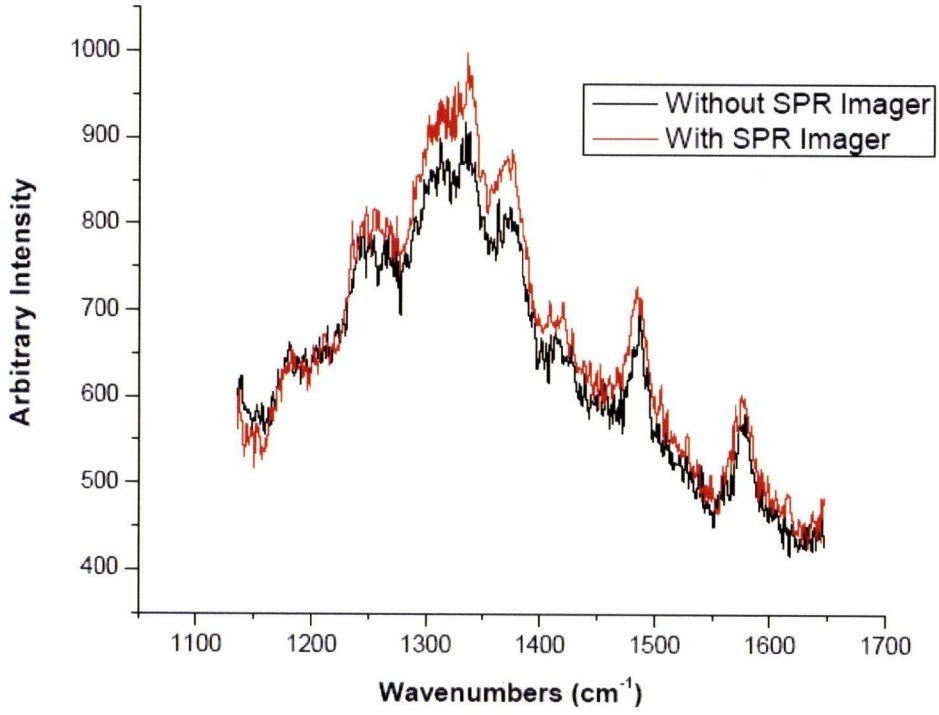

Figure 6.11: (Black) Salmon Sperm DNA spectra taken with 34 mW laser intensity taken for 10 minutes at 785nm without the addition of the SPR imager. (Red) Salmon Sperm DNA spectra taken with 34 mW laser intensity taken for 10 minutes at 785 with the SPR imager in operation.

Figure 6.10 shows the Raman spectra collected from a drop of Salmon Sperm DNA evaporated on the surface of a gold slide with and without additional irradiation from the SPR imager. At first comparison both spectra contain the same features and morphology. Additionally, both spectra also contain all the same features observed in the spectrum of the bulk DNA sample. This confirms that the signal is originating from DNA and not from another anomalous source. The other significant observation made from these spectra is that the additional irradiation of the SPR imager appears to increase the intensity of the collected spectra. Control experiments which measured the signal from just the diode laser found no difference in signal intensity between having the diode on or off. Previous studies have shown that marginal enhancement is possible when SPR and Raman are combined in similar fashions and this evidence supports this observation. Unfortunately, the signal enhancement observed in this experiment are weaker than that seen from the enhancements observed with both SERS and UVRRS. However, the fact that enhancement was observed in this proof-of-concept instrument is very encouraging and definitely merits further experimental follow-up.

6.5 Conclusion and Future Directions

This project merely represents the completion of the proof of concept phase of this research. During the course of this research some immediate concerns with the current device need to be addressed before any significant data collection can proceed. Although effective for these purposes, the current angle tuning apparatus will need to be replaced with an accurate angle adjustment system. A high precision step motor would probably be the best choice for this change. As previously mentioned, the detector used in

the imager was not designed to act as an analytical instrument. Redesigning the device to incorporate a low noise CCD would be crucial to acquire analytical measurements. In an attempt to make the device more practical, the optics could be changed to illuminate a larger area of the gold slide and thereby increasing the imaging area. Another avenue that could be explored while redesigning this instrument involves adapting it to include a flow channel to allow for the Raman analysis of SPR kinetic experiments. Once redesigned, an obvious follow up experiment would involve performing experiments on a spotted microarray. This experiment would be crucial to assess any possible applications that this device could have in the future. If a flow through channel was incorporated, the information from Raman could provide additional information for these studies.

References

1. Raman, C. V. & Krishnan, K. S. A New Type of Secondary Radiation. *Nature (London)* **121**, 501-502 (1928).
2. Ferraro, J. R. & Nakamoto, K. *Introductory Raman Spectroscopy* (Academic Press, Boston, 1994).
3. Skoog, D. A. & Leary, J. J. *Principles of Instrumental Analysis* (Saunders College Publishing, Fort Worth, 1992).
4. Hashimoto, S., Teraoka, J., Inubushi, T., Yonetani, T. & Kitagawa, T. Resonance Raman study on cytochrome c peroxidase and its intermediate. Presence of the Fe(IV) = O bond in compound ES and heme-linked ionization. *JOURNAL OF BIOLOGICAL CHEMISTRY* **261**, 11110-8 (1986).
5. Hildebrandt, P., English, A. M. & Smulevich, G. Cytochrome c and cytochrome c peroxidase complex as studied by resonance Raman spectroscopy. *BIOCHEMISTRY* **31**, 2384-92 (1992).
6. Sievers, G., Osterlund, K. & Ellfolk, N. Resonance Raman study on yeast cytochrome c peroxidase. Effect of coordination and axial ligands. *BIOCHIMICA ET BIOPHYSICA ACTA* **581**, 1-14 (1979).
7. Smulevich, G., Mantini, A. R., English, A. M. & Mauro, J. M. Effects of temperature and glycerol on the resonance Raman spectra of cytochrome c peroxidase and selected mutants. *BIOCHEMISTRY* **28**, 5058-64 (1989).
8. Smulevich, G. et al. Cytochrome c peroxidase mutant active site structures probed by resonance Raman and infrared signatures of the CO adducts. *BIOCHEMISTRY* **27**, 5486-92 (1988).
9. Smulevich, G. et al. Heme pocket interactions in cytochrome c peroxidase studied by site-directed mutagenesis and resonance Raman spectroscopy. *BIOCHEMISTRY* **27**, 5477-85 (1988).
10. Smulevich, G., Evangelista-Kirkup, R., English, A. & Spiro, T. G. Raman and infrared spectra of cytochrome c peroxidase-carbon monoxide adducts in alternative conformational states. *BIOCHEMISTRY* **25**, 4426-30 (1986).
11. Zhang, S. L., Michaelian, K. H. & Loppnow, G. R. Vibrational Spectra and Experimental Assignments of Thymine and Nine of Its Isotopomers. *Journal of Physical Chemistry* **102**, 461-470 (1998).
12. Toyama, A., Takino, Y., Takeuchi, H. & Harada, I. Ultravioloet Resonance Raman spectra of Ribosyl C(1')-Deuterated Purine Nucleosides: Evidence of Vibrational Coupling between Purine and Ribose Rings. *Journal of the American Chemical Society* **115**, 11092-11098 (1993).
13. Thorogood, H., Waters, T. R., Parker, A. W., Wharton, C. W. & Connolly, B. A. Resonance Raman Spectroscopy of 4-Thiothymidine and Oligodeoxynucleotides Containing This Base Both Free in Solution and Bound to the Restriction Endonuclease EcoRV. *Biochemistry* **35**, 8723-8733 (1996).
14. Mukerji, I., Shiber, M. C., Spiro, T. G. & Fresco, J. A UV Resonance Raman Study of $d(A^{+}\text{-}G)_{10}$, a Single-Stranded Helix without Stacked or Paired Bases. *Biochemistry* **34**, 14300-14303 (1995).

15. Perno, J. R., Grygon, C. A. & Spiro, T. G. Ultraviolet Raman Excitation Profiles for the Nucloetides and for the Nucleic Acid Duplexes Poly(rA)-Poly(rU) and Poly(dG-dC). *Journal of Physical Chemistry* **93**, 5672-5678 (1989).
16. Fodor, S. p. A. & Spiro, T. G. Ultraviolet Resonance Raman Spectroscopy of DNA with 200-266 nm Laser Excitation. *Journal of the American Chemical Society* **108**, 3198-3205 (1986).
17. Wen, Z. Q. & Thomas, G. J. J. Uv Resonance Raman Spectroscopy of DNA and Protein Constituents of Viruses: Assignments and Cross Sections for Excitations at 257, 244, 238, and 229 nm. *Biopolymers* **45**, 247-256 (1998).
18. Yazdi, Y. et al. Resonance Raman spectroscopy at 257 nm excitation of normal and malignant cultured breast and cervical cells. *Applied Spectroscopy* **53**, 82-85 (1999).
19. Thomas, G. J. J. Raman spectroscopy of protein and nucleic acid assemblies. *Annual Review of Biophysics & Biomolecular Structure* **28**, 1-27 (1999).
20. Fujimoto, N., Toyama, A. & Takeuchi, H. Effects of Hydrogen Bonding On the Uv Resonance Raman Bands of the Adenine Ring and Its C8-Deuterated Analog. *Journal of Molecular Structure* **447**, 61-69 (1998).
21. Chan, S. S., Austin, R. H., Mukerji, I. & Spiro, T. G. Temperature-Dependent Ultraviolet Resonance Raman Spectroscopy of the Premelting State of Da-Center-Dot-Dt Dna. *Biophysical Journal* **72**, 1512-1520 (1997).
22. Russell, M. P., Vohnik, S. & Thomas, G. J., Jr. Design and Performance of an Ultraviolet Resonance Raman Spectrometer for Proteins and Nucleic Acids. *Biophysical Journal* **68**, 1607-1612 (1995).
23. Suen, W., Spiro, T. G., Sowers, L. C. & Fresco, J. R. Identification by UV resonance Raman spectroscopy of an imino tautomer of 5-hydroxy-2 '-deoxycytidine, a powerful base analog transition mutagen with a much higher unfavored tautomer frequency than that of the natural residue 2 '-deoxycytidine. *Proceedings of the National Academy of Sciences of the United States of America* **96**, 4500-4505 (1999).
24. Cherny, D. Y. et al. DNA unwinding upon strand-displacement binding of a thymine-substituted polyamide to double-stranded DNA. *Proceedings of the National Academy of Sciences of the United States of America* **90**, 1667-1670 (1993).
25. Albrecht, M. G. & Creighton, J. A. Anomalously intense Raman spectra of pyridine at a silver electrode. *Journal of the American Chemical Society* **99**, 5215-17 (1977).
26. Jeanmaire, D. L. & Van Duyne, R. P. Surface Raman spectroelectrochemistry Part I. Heterocyclic, aromatic, and aliphatic amines adsorbed on the anodized silver electrode. *Journal of Electroanalytical Chemistry* **84**, 1-20 (1977).
27. Kneipp, K. Raman spectroscopy of single molecules. *Single Molecules* **2**, 291-292 (2001).
28. Stockman, M. I. Chaos and spatial correlations for dipolar eigenproblems. *Physical Review Letters* **79**, 4562-4565 (1997).
29. Kneipp, K. et al. Single Molecule Detection Using Surface-Enhanced Raman Scattering (SERS). *Physical Review Letters* **78**, 1667-1670 (1997).

30. Kneipp, K. et al. Detection and Identification of a single DNA base molucle using surface-enhanced Raman scattering (SERS). *Physical Review E* **57**, R6281-R6284 (1998).
31. Stockman, M. I. Inhomogeneous eigenmode localization, chaos, and correlations in large disordered clusters. *Physical Review E* **56**, 6494-6507 (1997).
32. Stockman, M. I., Pandey, L. N., Muratov, L. S. & George, T. F. Optical-Absorption and Localization of Eigenmodes in Disordered Clusters. *Physical Review B* **51**, 185-195 (1995).
33. Stockman, M. I., Pandey, L. N. & George, T. F. Inhomogeneous localization of polar eigenmodes in fractals. *Physical Review B* **53**, 2183-2186 (1996).
34. Shalaev, V. M., Poliakov, E. Y. & Markel, V. A. Small-particle composites .2. Nonlinear optical properties. *Physical Review B* **53**, 2437-2449 (1996).
35. Markel, V. A. et al. Near-field optical spectroscopy of individual surface-plasmon modes in colloid clusters. *Physical Review B* **59**, 10903-10909 (1999).
36. Markel, V. A., Shalaev, V. M., Stechel, E. B., Kim, W. & Armstrong, R. L. Small-particle composites .1. Linear optical properties. *Physical Review B* **53**, 2425-2436 (1996).
37. Markel, V. A., Muratov, L. S., Stockman, M. I. & George, T. F. Theory and Numerical-Simulation of Optical-Properties of Fractal Clusters. *Physical Review B* **43**, 8183-8195 (1991).
38. Zang, L. & Rodgers, M. A. Formation of tryptophan radicals in irradiated aqueous solutions of hexachloroplatinate(IV): a flash photolysis study. *PHOTOCHEMISTRY AND PHOTOBIOLOGY FIELD Publication Date:1999 Oct* **70**, 565-7. FIELD Reference Number: FIELD Journal Code:0376425 FIELD Call Number: (1999).
39. Otto, A. What is observed in single molecule SERS, and why? *Journal of Raman Spectroscopy* **33**, 593-598 (2002).
40. Bao, L.-L., Mahurin, S. M., Liang, C.-D. & Dai, S. Study of silver films over silica beads as a surface-enhanced raman scattering (SERS) substrate for detection of benzoic acid. *Journal of Raman Spectroscopy* **34**, 394-398 (2003).
41. Muniz-Miranda, M. Silver clusters onto nanosized colloidal silica as novel surface-enhanced raman scattering active substrates. *Applied Spectroscopy* **57**, 655-660 (2003).
42. Seitz, O. et al. Preparation and characterisation of gold nanoparticle assemblies on silanised glass plates. *Colloids and Surfaces, A: Physicochemical and Engineering Aspects* **218**, 225-239 (2003).
43. Muniz-Miranda, M. Silver-doped silica colloidal nanoparticles. Characterization and optical measurements. *Colloids and Surfaces, A: Physicochemical and Engineering Aspects* **217**, 185-189 (2003).
44. Bjerneld, E. J., Svedberg, F. & Kaell, M. Laser-Induced Growth and Deposition of Noble-Metal Nanoparticles for Surface-Enhanced Raman Scattering. *Nano Letters* **3**, 593-596 (2003).
45. Li, X. et al. Mercaptoacetic Acid-Capped Silver Nanoparticles Colloid: Formation, Morphology, and SERS Activity. *Langmuir* **19**, 4285-4290 (2003).

46. Mulvaney, S. P., He, L., Natan, M. J. & Keating, C. D. Three-layer substrates for surface-enhanced Raman scattering: preparation and preliminary evaluation. *Journal of Raman Spectroscopy* **34**, 163-171 (2003).
47. Nabiev, I. R., Konstantin, V. S. & Voloshin, O. N. Surface-Enhanced Raman Spectroscopy of Biomolecules Part III. Determination of the Local Destabilization Regions in the Double Helix. *Journal of Raman Spectroscopy* **21**, 333-336 (1990).
48. Garrell, R. L., Herne, T. M., Ahern, A. M. & Sullenberger, E. Surface-enhanced Raman spectroscopy of peptides. *Proceedings of SPIE - The International Society for Optical Engineering* **1201**, 451-459 (1990).
49. Isola, N. R., Stokes, D. L. & Vo-Dinh, T. Surface-Enhanced Raman Gene Probe for HIV detection. *Analytical Chemistry* **70**, 1352-1356 (1998).
50. Kneipp, K. et al. Surface-enhanced Raman scattering (SERS)- a new tool for single molecule detection and identification. (1998).
51. Morris, M. D., McGlashen, M. L. & Davis, K. L. Surface-enhanced Raman (SERS) probes of neurotransmitters. *Proceedings of SPIE - The International Society for Optical Engineering* **1201**, 447-450 (1990).
52. Vo-Dinh, T., Hiromoto, M. Y. K., Begun, G. M. & Moody, R. L. Surface-Enhanced Raman Spectrometry for Trace Organic Analysis. *Analytical Chemistry* **56**, 1667-1670 (1984).
53. Wood, R. W. On a remarkable case of uneven distribution of light in a diffraction grating spectrum,. *Phil. Magm.*, 396-402 (1902).
54. Otto, A. Excitation of nonradiative surface plasma waves in silver by the method of frustrated total reflection. *Zeitschrift fuer Physik* **216**, 398-410 (1968).
55. Kretschmann, E. R., H. Radiative decay of non-radiative surface plasmons excited by light. *Zeitschrift fuer Naturforschung* **23A**, 2135-2136 (1968).
56. Nylander, C., Liedberg, B. & Lind, T. Gas detection by means of surface plasmon resonance. *Sensors and Actuators* **3**, 79-88 (1982).
57. Liedberg, B., Nylander, C. & Lundstroem, I. Surface plasmon resonance for gas detection and biosensing. *Sensors and Actuators* **4**, 299-304 (1983).
58. Jonsson, U. et al. Real-time biospecific interaction analysis using surface plasmon resonance and a sensor chip technology. *Biotechniques* **11**, 620-7 (1991).
59. Homola, Jiři. Present and future of surface plasmon resonance biosensors. *Anal Bioanal Chem* (2003) 377 : 528− 539
60. Homola, J., Yee, S. S. & Gauglitz, G. Surface plasmon resonance sensors: review. *Sensors and Actuators, B: Chemical* **B54**, 3-15 (1999).
61. Knoll, W. Interfaces and thin films as seen by bound electromagnetic waves. *Annual Review of Physical Chemistry* **49**, 569-638 (1998).
62. Salamon, Z., Macleod, H. A. & Tollin, G. Surface plasmon resonance spectroscopy as a tool for investigating the biochemical and biophysical properties of membrane protein systems. I: Theoretical principles. *Biochimica et Biophysica Acta (BBA) - Reviews on Biomembranes* **1331**, 117-129 (1997).
63. Szabo, A., Stolz, L. & Granzow, R. Surface plasmon resonance and its use in biomolecular interaction analysis (BIA). *Current Opinion in Structural Biology* **5**, 699-705 (1995).64. Liedberg, B., Nylander, C. & Lundstrom, I. Biosensing

with surface plasmon resonance -- how it all started. *Biosensors and Bioelectronics* **10**, i-ix (1995).

65. Margulies, D. H., Plaksin, D., Khilko, S. & Jelonek, M. T. Studying interactions involving the T-cell antigen receptor by surface plasmon resonance. *Current Opinion in Immunology* **8**, 262-270 (1996).
66. Salamon, Z., Macleod, H. A. & Tollin, G. Surface plasmon resonance spectroscopy as a tool for investigating the biochemical and biophysical properties of membrane protein systems. II: Applications to biological systems. *Biochimica et Biophysica Acta (BBA) - Reviews on Biomembranes* **1331**, 131-152 (1997).
67. van der Merwe, P. A. & Barclay, A. N. Analysis of cell-adhesion molecule interactions using surface plasmon resonance. *Current Opinion in Immunology* **8**, 257-261 (1996).
68. Corn, R. M., Nelson, B. P., Smith, E. & Hurtt, G. Surface plasmon resonance imaging studies of DNA and protein microarrays. *Polymeric Materials Science and Engineering* **84**, 19 (2001).
69. Yu, X. et al. Micro-array detection system for gene expression products based on surface plasmon resonance imaging. *Sensors and Actuators, B: Chemical* **B91**, 133-137 (2003).
70. Smith, E. A., Thomas, W. D., Kiessling, L. L. & Corn, R. M. Surface Plasmon Resonance Imaging Studies of Protein-Carbohydrate Interactions. *Journal of the American Chemical Society* **125**, 6140-6148 (2003).
70. Palumbo, M., Pearson, C., Nagel, J. & Petty, M. C. A single chip multi-channel surface plasmon resonance imaging system. *Sensors and Actuators, B: Chemical* **B90**, 264-270 (2003).
71. Vetter, D. Chemical microarrays, fragment diversity, label-free imaging by plasmon resonance-a chemical genomics approach. *Journal of Cellular Biochemistry*, 79-84 (2002).
72. Smith, E. A., Erickson, M. G., Ulijasz, A. T., Weisblum, B. & Corn, R. M. Surface Plasmon Resonance Imaging of Transcription Factor Proteins: Interactions of Bacterial Response Regulators with DNA Arrays on Gold Films. *Langmuir* **19**, 1486-1492 (2003).
73. Lee, H. J., Goodrich, T. T. & Corn, R. M. SPR imaging measurements of 1-D and 2-D DNA microarrays created from microfluidic channels on gold thin films. *Analytical Chemistry* **73**, 5525-5531 (2001).
74. Pirrung, M. C. How to make a DNA chip. *Angewandte Chemie, International Edition* **41**, 1276-1289 (2002).
75. Cheung, V. G. et al. Making and reading microarrays. *Nature Genetics* **21**, 15-19 (1999).
76. Southern, E.M. *Methods in Molecular Biology, vol 170: DNA Arrays: Methods and Protocols*. Edited by Rampal J. B. 1-15 (2001).
77. Grunstein, M., Hogness, D. S. Colony Hybridization: a method for the isolation of cloned DNAs that contain a specific gene. *Proceedings of the National Academy of Science* **72**. 3961-3965 (1975).
78. Hoheisel, J. D. et al. Relational genome analysis using reference libraries and hybridisation fingerprinting. *Journal of Biotechnology* **35**. 121-134 (1994).

79. Letsinger et al. Phosphite coupling procedure for generating internucleotide links. *Journal of the American Chemical Society* **97**. 3278-3279 (1975)
80. Kafatos et al. Determination of nucleic acid sequence homologies and relative concentrations by a dot hybridization procedure. *Nucleic Acids Research* **7**. 1541-1552 (1979).
81. Beaucage, S. L., Caruthers, M. H. Deoxynucleoside phosphoramidites – a new class of key intermediates for deoxyploynucleiotide links. *Journal of the American Chemical Society* **97**. 3278-3279 (1981).
82. Lipshutz, R. J., Fodor, S. P. A., Gingeras, T. R. & Lockhart, D. J. High density synthetic oligonucleotide arrays. *Nature Genetics* **21**, 20-24 (1999).
83. Caviani Pease, A. et al. Light-Generated Arrays for Rapid DNA Sequence Analysis. *Proceedings of the National Academy of Science* **91**. 5022-5026 (1994).
84. Li, X.,et al. DNA Microarrays:Their Use and Misuse. *Microcirculation* **9**. 13-22 (2002)
85. Heller, M. J. DNA Microarray Technology:Devices, Systems and Applications. *Annual Review of Biomedical Engineering* **4**. 129-153 (2002)
86. Zhang, S., Gant, T. W. A statistical framework for the design of microarray experiments and effective detection of differential gene expression. *Bioinformatics* (2004) [Epub ahead of print]
87. Tseng, G. C. et al. Issues in cDNA microarray analysis:quality filtering, channel normalization, models of variations, and assessment of gene effects. *Nucleic Acids Research* **29**. 12, 2549-2557 (2001).
88. Yang, Y. H. et al. Normalization for cDNA Microarray Data:A Robust Composite Method Addressing Single and Multiple Slide Systematic Variations. *Nucleic Acids Research* **30**, e15 (2002).
89. Yu, J. et al. Evaluation and optimization of procedures for target labeling and hybridization of cDNA microarrays. *Molecular Vision [online computer file]* **8**, 130-137 (2002).
90. Xiang, C. C. et al. Amine-modified random primers to label probes for DNA microarrays. *Nature Biotechnology* **20**, 738-742 (2002).
91. Hoen, P. A. C., de Kort, F., van Ommen, G. J. B. & den Dunnen, J. T. Fluorescent labelling of cRNA for microarray applications. *Nucleic Acids Research* **31**, e20/1-e20/8 (2003).
92. Bassil, N. et al. One hundred spots parallel monitoring of DNA interactions by SPR imaging of polymer-functionalized surfaces applied to the detection of cystic fibrosis mutations. *Sensors and Actuators B* **94**, 313–323 (2003).
93. Corn, R. M., Nelson, B. P., Smith, E. & Hurtt, G. Surface plasmon resonance imaging studies of DNA and protein microarrays. *Polymeric Materials Science and Engineering* **84**, 19 (2001).
94. Mariotti, E., Minunni, M. & Mascini, M. Surface plasmon resonance biosensor for genetically modified organisms detection. *Analytica Chimica Acta* **453**, 165–172 (2002).
95. Smith, E. A., Erickson, M. G., Ulijasz, A. T., Weisblum, B. & Corn, R. M. Surface Plasmon Resonance Imaging of Transcription Factor Proteins: Interactions of Bacterial Response Regulators with DNA Arrays on Gold Films. *Langmuir* **19**, 1486-1492 (2003).

96. Smith, E. A., Thomas, W. D., Kiessling, L. L. & Corn, R. M. Surface Plasmon Resonance Imaging Studies of Protein-Carbohydrate Interactions. *Journal of the American Chemical Society* **125**, 6140-6148 (2003).
97. Cole, K. A., Krizman, D. B. & Emmert-Buck, M. R. The genetics of cancer--a 3D model. *Nature Genetics* **21**, 38-41 (1999).
98. Debouck, C. & Goodfellow, P. N. DNA microarrays in drug discovery and development. *Nature Genetics* **21**, 48-50 (1999).
99. Duggan, D. J., Bittner, M., Chen, Y., Meltzer, P. & Trent, J. M. Expression profiling using cDNA microarrays. *Nature Genetics* **21**, 10-14 (1999).
100. Hacia, J. G. Resequencing and mutational analysis using oligonucleotide microarrays. *Nature Genetics* **21**, 42-47 (1999).
101. Bailey, S. N., Wu, R. Z. & Sabatini, D. M. Applications of transfected cell microarrays in high-throughput drug discovery. *Drug Discovery Today* **7**, S113-S118 (2002).
102. Becker, Y. Herpes simplex virus evolved to use the human defense mechanisms to establish a lifelong infection in neurons - A review and hypothesis. *Virus Genes* **24**, 187-196 (2002).
103. Ellis, J. S. & Zambon, M. C. Molecular diagnosis of influenza. *Reviews in Medical Virology* **12**, 375-389 (2002).
104. Reinke, V. Functional exploration of the C. elegans genome using DNA microarrays. *Nature Genetics* **32**, 541-546 (2002).
105. Greek, L. S. in *Electrical Engineering* (University of British Columbia, Vancouver, 1996).
106. Wen, Z. Q., Overman, S. A. & Thomas, G. J. Structure and Interactions of the Single-Stranded Dna Genome of Filamentous Virus Fd - Investigation By Ultraviolet Resonance Raman Spectroscopy. *Biochemistry* **36**, 7810-7820 (1997).
107. Dunford, B. H. in *Heme Peroxidases* 23-29 (John Wiley & Sons, 1999).
108. Everse, J. E., K.E. in *Peroxidases in Chemistry and Biology* 51-84 (CRC Press LLC, 1990).
109. Erman, J. E. & Vitello, L. B. Yeast cytochrome c peroxidase: mechanistic studies via protein engineering. *Biochimica et Biophysica Acta (BBA) - Protein Structure and Molecular Enzymology* **1597**, 193-220 (2002).
110. Hildebrandt, P., English, A. M. & Smulevich, G. Cytochrome c and cytochrome c peroxidase complex as studied by resonance Raman spectroscopy. *BIOCHEMISTRY* **31**, 2384-92 (1992).
111. Hashimoto, S., Teraoka, J., Inubushi, T., Yonetani, T. & Kitagawa, T. Resonance Raman study on cytochrome c peroxidase and its intermediate. Presence of the Fe(IV) = O bond in compound ES and heme-linked ionization. *JOURNAL OF BIOLOGICAL CHEMISTRY* **261**, 11110-8 (1986).
112. Ivancich, A., Dorlet, P., Goodin, D. B. & Un, S. Multifrequency High-Field EPR Study of the Tryptophanyl and Tyrosyl Radical Intermediates in Wild-Type and the W191G Mutant of Cytochrome c Peroxidase. *Journal of the American Chemical Society* **123**, 5050-5058 (2001).
113. Sievers, G., Osterlund, K. & Ellfolk, N. Resonance Raman study on yeast cytochrome c peroxidase. Effect of coordination and axial ligands. *BIOCHIMICA ET BIOPHYSICA ACTA* **581**, 1-14 (1979).

114. Smulevich, G., Evangelista-Kirkup, R., English, A. & Spiro, T. G. Raman and infrared spectra of cytochrome c peroxidase-carbon monoxide adducts in alternative conformational states. *BIOCHEMISTRY* **25**, 4426-30 (1986).
115. Smulevich, G. et al. Cytochrome c peroxidase mutant active site structures probed by resonance Raman and infrared signatures of the CO adducts. *BIOCHEMISTRY* **27**, 5486-92 (1988).
116. Smulevich, G. et al. Heme pocket interactions in cytochrome c peroxidase studied by site-directed mutagenesis and resonance Raman spectroscopy. *BIOCHEMISTRY* **27**, 5477-85 (1988).
117. Smulevich, G., Mantini, A. R., English, A. M. & Mauro, J. M. Effects of temperature and glycerol on the resonance Raman spectra of cytochrome c peroxidase and selected mutants. *BIOCHEMISTRY* **28**, 5058-64 (1989).
118. Spiro, T. G., Smulevich, G. & Su, C. Probing protein structure and dynamics with resonance Raman spectroscopy: cytochrome c peroxidase and hemoglobin. *Biochemistry* **29**, 4497-508. FIELD Reference Number:121 FIELD Journal Code:0370623 FIELD Call Number: (1990).
119. Bunte, S. W. et al. Theoretical determination of the vibrational absorption and Raman spectra of 3-methylindole and 3-methylindole radicals. *Chemical Physics* **265**, 13-25 (2001).
120. Greek, L. S. in *Electrical Engineering* (University of British Columbia, Vancouver, 1996).
121. Wittenberg, B. A., Kampa, L., Wittenberg, J. B., Blumberg, W. E. & Peisach, J. Electronic structure of protoheme proteins. II. Electron paramagnetic resonance and optical study of cyctochrome c peroxidase and its derivatives. *Journal of Biological Chemistry* **243**, 1863-70 (1968).
122. Ho, P. S., Hoffman, B. M., Kang, C. H. & Margoliash, E. Control of the transfer of oxidizing equivalents between heme iron and free radical site in yeast cytochrome c peroxidase. *Journal of Biological Chemistry* **258**, 4356-63 (1983).
123. Sigma. (1996).
124. Zang, L. & Rodgers, M. A. Formation of tryptophan radicals in irradiated aqueous solutions of hexachloroplatinate(IV): a flash photolysis study. *PHOTOCHEMISTRY AND PHOTOBIOLOGY FIELD Publication Date:1999 Oct* **70**, 565-7. FIELD Reference Number: FIELD Journal Code:0376425 FIELD Call Number: (1999).
125. Austin, J. C., Jordan, T. & Spiro, T. G. in *Advances in Spectroscopy* (eds. Clark, R. J. H. & Hester, R. E.) 55-126 (John Wiley & Sons, Chichester, England, 1993).
126. Asher, S. A., Ludwig, M. & Johnson, C. R. UV Resonance Raman Excitation Profiles of the Aromatic Amino Acids. *Journal of the American Chemical Society* **108**, 3186-3197 (1986).
127. Chi, Z. H. & Asher, S. A. UV Raman determination of the environment and solvent exposure of Tyr and Trp residues. *Journal of Physical Chemistry* **102B**, 9595-9602 (1998).
128. Fodor, S. P. A., Copeland, R. A., Grygon, C. A. & Spiro, T. G. Deep-Ultraviolet Raman Excitation Profiles and Vibronic Scattering Mechanisms of Phenylalanine, Tyrosine, and Tryptophan. *Journal of the American Chemical Society* **111**, 5509-5518 (1989).

129. Johnson, C. R., Ludwig, M. & Asher, S. A. Ultraviolet Resonance Raman Characterization of Photochemical Transients of Phenol, Tyrosine, and Tryptophan. *Journal of the American Chemical Society* **108**, 905-912 (1986).
130. Rava, R. P. & Spiro, T. G. Resonance Enhancement in the Ultraviolet Raman Spectra of Aromatic Amino Acids. *Journal of Physical Chemistry* **89**, 1856-1861 (1985).
131. Qin, Y. & Wheeler, R. A. Similarities and Differences between Phenoxyl and Tyrosine Phenoxyl Radical Structures, Vibrational Frequencies, and Spin Densities. *Journal of the American Chemical Society* **117**, 6083-92 (1995).
132. Knobloch, H. & Knoll, W. Raman spectroscopy and imaging with surface-plasmon polaritons. *Makromolekulare Chemie, Macromolecular Symposia* **46**, 389-93 (1991).
133. Knobloch, H., Brunner, H., Leitner, A., Aussenegg, F. & Knoll, W. Probing the evanescent field of propagating plasmon surface polaritons by fluorescence and Raman spectroscopies. *Journal of Chemical Physics* **98**, 10093-5 (1993).
134. Ushioda, S. & Sasaki, Y. Raman scattering mediated by surface-plasmon polariton resonance. *Physical Review B: Condensed Matter and Materials Physics* **27**, 1401-4 (1983).
135. Corn, R. M., Nelson, B. P., Smith, E. & Hurtt, G. Surface plasmon resonance imaging studies of DNA and protein microarrays. *Polymeric Materials Science and Engineering* **84**, 19 (2001).
136. Yu, X. et al. Micro-array detection system for gene expression products based on surface plasmon resonance imaging. *Sensors and Actuators, B: Chemical* **B91**, 133-137 (2003).
137. Smith, E. A., Thomas, W. D., Kiessling, L. L. & Corn, R. M. Surface Plasmon Resonance Imaging Studies of Protein-Carbohydrate Interactions. *Journal of the American Chemical Society* **125**, 6140-6148 (2003).
138. Palumbo, M., Pearson, C., Nagel, J. & Petty, M. C. A single chip multi-channel surface plasmon resonance imaging system. *Sensors and Actuators, B: Chemical* **B90**, 264-270 (2003).
139. Smith, E. A., Erickson, M. G., Ulijasz, A. T., Weisblum, B. & Corn, R. M. Surface Plasmon Resonance Imaging of Transcription Factor Proteins: Interactions of Bacterial Response Regulators with DNA Arrays on Gold Films. *Langmuir* **19**, 1486-1492 (2003).
140. Lee, H. J., Goodrich, T. T. & Corn, R. M. SPR imaging measurements of 1-D and 2-D DNA microarrays created from microfluidic channels on gold thin films. *Analytical Chemistry* **73**, 5525-5531 (2001).
141. Nelson, B. P., Frutos, A. G., Brockman, J. M. & Corn, R. M. Near-Infrared Surface Plasmon Resonance Measurements of Ultrathin Films. 1. Angle Shift and SPR Imaging Experiments. *Analytical Chemistry* **71**, 3928-3934 (1999).
142. Corn, R. M.
143. Movileanu, L., Benevides, J. M. & Thomas, J., George J. Temperature Dependence of the Raman Spectrum of DNA. Part I—Raman Signatures of Premelting and Melting Transitions of Poly(dA–dT)·Poly(dA–dT). *J. Raman Spectrosc.* **30**, 637-649 (1999).

144. Movileanu, L., Benevides, J. M. & Thomas Jr., G. J. Temperature Dependence of the Raman Spectrumof DNA. II. Raman Signatures of Premelting and Melting Transitions of Poly(dA)_Poly(dT) and Comparison with Poly(dA-dT)_Poly(dA-dT). *Biopolymers* **63**, 181–194 (2002).
145. Carrier, V. & Savoie, R. Raman Spectroscopic Study of the Conformation and Melting of Poly(dG) - Poly(dC) and Poly(dG-dC) - Poly(dG-dC) in Aqueous Solution. *Journal of Solution Chemistry* **29** (2000).
146. Dong, L. Q., Zhou, J. Z., Wu, L. L., Dong, P. & Lind, Z. H. SERS studies of self-assembled DNA monolayer – characterization of adsorption orientation of oligonucleotide probes and their hybridized helices on gold substrate. *Chemical Physics Letters* **354**, 458–465 (2002).
147. Deng, H., Bloomfield, V. A., Benevides, J. M. & Thomas, J., George J. Dependence of the Raman Signature of Genomic B-DNA on Nucleotide Base Sequence. *Biopolymers* **50**, 656–666 (1999).
148. Perno, J. R., Grygon, C. A. & Spiro, T. G., Thomas G. Ultraviolet Raman Excitation Profiles for the Nucleotides and for the Nucleic Acid Duplexes Poly(rA)-Poly(rU) and Poly(dG-dC). *J. Phys. Chem.* **93**, 5612-5678 (1989).
149. Zhang, R.-Y. et al. Investigation of Ordered ds-DNA Monolayers on Gold Electrodes. *J. Phys. Chem. B* **106**, 11233-11239 (2002).
150. Li, J. et al. Temperature-dependent Raman and infrared spectra of nucleosides. III—deoxycytidine. *J. Raman Spectrosc.* **34**, 183–191 (2003).

Appendix

Isolation of Recombinant Cytochrome c Peroxidase from E. Coli

1. From a plate of freshly transformed BL21(DE3) cells with the desired mutant plasmid (pT7 CcP), inoculate a 3 mL culture of superbroth/amp (see media preparation) and grow at 37°C with shaking (250 rpm) for 4-5 hours, until some turbidity is evident.
2. Use 500 μL of this culture to inoculate 50 mL of superbroth/amp in 250 mL Erlenmeyer flast and incubate with shaking at 37°C for 2-3 hours until some turbidity is evident (Do not let these cultures overgrow. The final yield of CcP seems to be quite sensitive to the age of the inocula used).
3. Inoculate each 10 L superbroth/amp in 2L Erlenmeyer flasks with 1 mL of the previous culture and grow for 10-11 hours at 37°C with shaking (250 rpm). The OD_{600} at this point should be around 2, and some CcP will already be present. At this point, add 1 mL of a filter sterilized solution of 125 mg IPTG/mL to each flask, and continue the incubation for another 3 hours. At this point, there should be a large amount of CcP present in the cells, and an SDS gel of the cell lysate should give a clearly distinctive band of CcP.
4. Centrifuge cell (GS 3) for 6 minutes at 8000 rpm. Weigh the wet cells. All steps from this point should be performed at 4°C.
5. Resuspend cells in buffer B plus 1 mM PMSF (see lysis buffer preparation) to a final volume of ~100 mL. (It is important to resuspend the cell paste as well as possible and get a homogeneous suspension without any large clumps of cell. Use a spatula, and press the cells against the sides of the container. The centrifuge bottles with yellow caps are good containers in which to perform this operation).
6. Add 100 mg of lysozyme (Sigma) dissolved in 10 mL of water, and incubate on ice with gentle shaking for 1 hour. Freeze the cells in liquid nitrogen and store them in the –70°C freezer until ready to process them. (The final quality of the enzyme does not seem to be affected by the time the cells spend in "hibernation")
7. Take the container out of the freezer and let the cell suspension thaw overnight at 4°C. Add 5 mL of a 2 M solution of $MgCl_2$, 5 mg of DNase (Sigma) and 2 mg of RNase (Sigma) dissolved in a few mL of water, and mix well with a spatula (the suspension should be extremely viscous and sticky at this point). Shake gently at 4°C for ~1 hour an check the viscosity of the mixture. If it is still very viscous, add another 5 mg of Dnase and shake until the suspension can be easily sucked into a Pasteur pipette.
8. Centrifuge the suspension for 30 minutes at 8500 rpm in a precooled GS-3 rotor, and store the supernatant on ice. Wash the pellet twice with 50 mL of cold buffer B, and collect all the washes together with the first supernatant.
9. From the lysis procedure, ~ 200 mL of solution containing CcP/apo-CcP should be obtained. Place this solution in two 150 mL dialysis bags (see preparation of dialysis bads). Leave some room in the bag for expansion. Dialyze overnight at 4oC against 4 L of 50 mM potassium phosphate buffer/1 mM EDTA, pH 6.3.

(Make this buffer by diluting twentyfold with distilled water a stock of 1 M potassium phosphate buffer/20mM EDTA pH 6.0 @ 25°C).

10. Variable amounts of solid material (commonly known as "white stuff") will precipitate during dialysis. Centrifuge for 1 hour at 8500 rpm in a precooled GS-3 rotor.
11. Load the supernatant onto a 2.5 x 4 cm DEAE sepharose CL-6B column equilibrated with buffer A. Wash the column with 100 mL of buffer A, and elute with a linear gradient using 300 mL of buffer A and 300 mL of buffer C (use large linear gradient maker).
12. Run a 13% SDS PAGE gel on the fractions and pool those containing apo-CcP. (Note: A small amount of reconstituted protein that is sometimes produced by E.Coli, and that runs slower than apo-protein in the DEAE column, is not good enzyme. Since this represents a small fraction of the total discard these fractions).
13. Concentrate the pooled fractions, and exchange them into buffer B. The final volume should be ~10 mL. Load this material into a 2.5 x 100 cm G-75 fine column equilibrated in buffer B. (Note: While concentrating and exchanging the DEAE fractions does not bring the solution to a volume smaller than 10 mL, handling solutions that are too concentrated may damage the apo-protein. On the other hand loading a smaller volume onto the gel filtration column does not improve the resolution due to the great viscosity of the solution at this point).
14. Run a 13% SDS PAGE gel on the fractions and combine the fractions that contain a reasonable amount of CcP peptide (Note: Usually, the first fractions eluting from the column in the void volume contain variable amounts of the "white stuff". The apo-protein normally elutes after this fraction, or in some cases it may overlap with the final fractions of the "white stuff").
15. Concentrate the fraction to a volume of 30-40 mL and estimate the amount of apo-protein (MW (WT) = 33484): $\varepsilon_{280nm} = 55\ mM^{-1}cm^{-1}$ (Note: This extinction coefficient for the apo-protein is very likely an underestimate of the real value. Using this value leads to an overestimation of he amount of protein present. The yield of crystallized protein at the end of isolation procedure is approximately half of the yield estimated at this point).
16. Load this solution in a dialysis bag and dialyze overnight against 4 L of 0.1 M potassium phosphate buffer, pH 7.5 (Make this buffer by diluting the 1 M stock of potassium phosphate buffer, pH 7.2 @ 25°C tenfold with distilled water).
17. Prepare a solution of hemin as follows:
    a. Weigh 1.1 equivalents of hemin into a 15 mL Falcon tube covered with aluminum foil.
    b. Add 1 mL of 0.1 M NaOH and vortex vigorously for 5 min.
    c. Adjust the pH to >7 (but <7.5) by filling the tube with 0.1 M potassium phosphate buffer taken from last night's dialysis beaker. Vortex again for another 3 min.
18. Add the hemin solution to the dialysis bag containing the apo-protein. Mix and let stand for 1 hour in the same beaker shielded from light with aluminum foil.
19. Place bag into 4 L of 0.1 M phosphate buffer, pH 6.2 (Make this buffer by diluting 1 M stock of potassium phosphate buffer, pH 6.0 @ 25°C tenfold with distilled water) and dialyze for 6 to 10 hours.

20. Dialyze exhaustively against distilled water, changing the water twice a day. It will take several changes for the protein to start crystallizing.
21. After three to four days the crystallization is complete. Collect the crystals by centrifugation (20 min at 8000 rpm in an SS-34 rotor). Discard the supernatant which should have a green-brown colour due to excess heme. Wash the crystals twice with distilled cold water and redissolve them in approximately 20 mL of 0.1 M potassium phosphate buffer pH 6.2. Do not stir the solution too vigorously or pipette too fast. The solution of holo-CcP is very concentrated at this point, and it has to be treated with lots of care. Centrifuge this solution, keep the supernatant and wash the precipitate with 5 mL of the same buffer (Note: there can be a substantial amount of material that does not redissolve at this point. Do not worry, this seems to be normal. Just discard this material and concentrate in the fraction that does redissolve)
22. Fill a dialysis bad with the previous supernatant, and dialyze extensively against distilled water. The crystallization of the enzyme should be faster this time IT should take about two days.
23. Repeat the procedure described in #20 and 21. (The supernatant from the second crystallization should have much less colour than the one from the first crystallization since a large fraction of the excess heme has already been removed and there should be little enzyme that does not crystallize).
24. The material that has been crystallized three times is ready to be stored, used or sent away. Collect the crystals by centrifugation, discard the supernatant, and using a P1000 resuspend the crystals in ~2 mL of cold distilled water. Transfer the slurry to cryovials, check the quality of the enzyme, and determine the concentration of the suspension of crystals. Store the cryovials in liquid nitrogen.
25. Even after three crystallizations, there is still some free heme present in the reconstituted protein. When a certain amount of protein is needed for an experiment, the best way to proceed is to dissolve the crystals is to take the required amount of suspension, centrifuge to pellet the crystals and discard the supernatant that should be colourless or have a very faint color. Dissolve the pellet in the desired buffer and centrifuge again. A dark solution of the protein and a very dark pellet, that is essentially heme, should be obtained. Keep the supernatant and resuspend and wash the pellet once with the same buffer. Discard the pellet.

Media and Buffers

Superbroth
10g bactrotryptone
8g yeast extract
5g NaCl
1 mL glycerin

Make up to 1 L with distilled water and autoclave for 20 min. Before inoculating add 1 mL of a filter sterilized solution of 100 mg/mL of ampicillin.

Buffers for chromatography

Potassium phosphate, pH 6.0 @ 4°C. Buffer D is 1 mM EDTA.

		KH_2PO_4	K_2HPO_4	EDTA	pH
Buffer A: 50 mM	1L	5.87g	1.20g	---	6.11
	4L	23.47g	4.80g	---	
Buffer B: 100 mM	1L	11.21g	3.07g	0.38g	6.11
	4L	44.84g	12.28g	1.50g	
Buffer C: 500 mM	1L	50.44g	22.54g	---	6.08
	2L	100.88g	45.08g	---	
	4L	201.76g	90.16g	---	

Lysis Buffer

Dissolve17.5 mg of PMSF in 3 mL of ethanol and add this solution dropwise to 100 mL of cold buffer B, while stirring vigorously.

Dialysis stock buffers

Prepare a 1 M solution of K_2HPO_4 and a 1 M solution of KH_2PO_4. To make the stock buffers titrate one solution with the other to the desired pH (measure at 25°C). The stock buffer containing EDTA is prepared in the same way and EDTA is added at the end.

Cleaning Spectrapor Dialysis Tubing

1. To remove glycerol rinse with water for 3-4 hours at room temperature and then rinse with 1% acetic acid. Wash residual acetic acid off with distill water.
2. To remove sulfides, treat in the following manner.
   Solution A: 0.05% sodium sulfate
   Solution D: 0.016% sulfuric acid
   Soak the tubing in solution A for 1 minute.
   Soak the tubing in water at 60oC for 2 minutes.
   Soak the tubing in solution B for 1 minute.
   Wash with distilled water,
3. To remove metal contaminants, soak in EDTA (10 mM)/bicarbonate(10mM) solution for 5 minutes at room temperature. Wash with water. In washing and soaking be careful to treat both the outside and the inside of the tubing.